Analytical, Experimental, Computed Tomography Inspection, and Finite Element Modeling of the Material Extrusion Wave Infill in Additive Manufacturing

by

Robert S. Chisena

A dissertation submitted in partial fulfillment
of the requirements for the degree of
Doctor of Philosophy
(Mechanical Engineering)
in the University of Michigan
2019

Doctoral Committee:

Professor Albert J. Shih, Chair
Professor Thomas Armstrong
Professor Kira Barton
Research Investigator Jeffrey Plott
Assistant Professor Elliott Rouse

Robert S. Chisena

rchisena@umich.edu

ORCID iD: 0000-0002-0807-3947

Dedication

I would like to thank my parents, grandparents, brother, sister-in-law, and niece for their continued and on-going support of my work. They have always pushed me to excel in all aspects of my life, and I am incredibly blessed to call them my family.

I would like to thank Francesco Bianchini, Andrea Lupini, Damiete Horsfall, Rachel Schwind, and Giuseppe Battiato – a handful of the friends that I have made and that have helped me through this adventure.

I would like to thank my lab mates, Dian-Ru Li, Yang Liu, Lei Chen, Matthew Hildner, Jingxuan Lyu, Ketut Priambada, Ryan Posh, Yihao Zhen, Jeffrey Plott, and Miguel Angel Funes Lora, for the help and support that they have provided to me throughout my time in the Shih Lab. I would like to thank my undergraduate student, Sophia Marina Engstrom, for her help in my research topic. She demonstrated an incredible amount of dedication and maturity in her work.

I would like to thank my committee members, Professor Thomas Armstrong, Professor Kira Barton, Dr. Jeffrey Plott, and Professor Elliott Rouse. Each member worked with me to improve and refine my research topic, and I am grateful for the insights they have provided to me.

I would like to thank all of the Mechanical Engineering faculty and staff that I have interacted with and that have made my education at the University of Michigan a wonderful experience.

Finally, I would like to thank my advisor Professor Albert Shih. Over the course of my time in the Shih lab, I have learned many lessons from Professor Shih. However, one of the most important lessons I learned from him is his dedication to his students. During midnight phone calls

from Professor Shih to discuss research results or corrections to a research paper, I quickly learned that he was not just looking in from the outside, but he was in the trenches with us. This is something that I have always appreciated and something that motivated me to work harder. I strive to be this type of influence to the students that work with me and whose careers and lives that I impact.

"The noblest pleasure is the joy of understanding" – Leonardo da Vinci

Acknowledgements

This work was supported by the National Science Foundation PFI:BIC (Grant 1534003), the National Center for Defense Manufacturing and Machining and America Makes (NCDMM FA8650-12-2-7230), and the Blue Cross Blue Shield of Michigan Foundation.

I would like to thank Stratasys, Ltd. including Gary Larson and Andrew Hanson for their assistance in producing specimens for Chapters 2, 3, and 5 of this thesis. I would like to thank John Slotwinski, Edward Garboczi, Keith Hebenstreit, Felix Kim, and Shawn Moylan for sharing their CT data for Chapter 4 of this thesis. I would like to thank the Orthopedic Research Laboratory (ORL), including Basma Khoury, Lauran Smith, Andrea Clark, and Rob Goulet, for their assistance in describing the CT process and for scanning the specimens for Chapters 4 and 5 of this thesis.

Preface

This dissertation summarizes research that I have conducted over the past four years in the lab of Professor Albert J Shih. This dissertation is the part of the NSF PFI:BIC, which has three PhD students. My research area focuses on the material extrusion (MEX) manufacturing of the thin-walled structure (TWS) such as the ankle-foot orthosis (AFO). The NSF PFI:BIC is a project in collaboration with Prof. Barton's Ph.D. student, Deema Totah, investigating the effect of AFO stiffness on patient gait and Prof. Armstrong's Ph.D. student, Qianyi Fu, investigating a model of knee and ankle biomechanics of people with varying pathologies.

Chapters 2, 4, and 5 of this thesis have been submitted for publication and are presented with slight modifications and reformatting.

Chapter 1 Section 1.2 contains work, with modifications and reformatting that has been previously submitted as a conference paper as follows: "Chisena R, Totah D, Menon M, et al. Mechanical Stiffness and Healthy Subject Evaluation of Traditional and 3D-Printed Ankle-Foot Orthoses. World Congr. Biomech. Dublin, Ireland; 2018."

Chapter 2 contains work, with modifications and reformatting, that has been previously submitted for publication as follows: Chisena, R. S., and Shih, A. J., 2018, "Analytical Characterization and Experimental Validation of the Material Extrusion Wave Infill for Thin-Walled Structures," Manuscript Submitted for Publication to The American Society of Mechanical Engineers Journal of Manufacturing Science and Engineering.

Chapter 4 contains work, with modifications and reformatting, that will be submitted for publication as follows: Chisena, R. S., Engstrom, S. M., and Shih, A. J., 2019, "Thresholding

Method for the Computed Tomography Inspection of the Internal Composition of Parts Fabricated using Additive Manufacturing," to the Journal of Additive Manufacturing.

Chapter 5 contains work, with modifications and reformatting, that will be submitted for publication as follows: Chisena, R. S., Engstrom, S. M., and Shih, A. J., 2019, "Computed Tomography Evaluation of the Porosity and Fiber Orientation in Short Carbon Fiber Material Extrusion Filaments and Parts," to the Journal of Additive Manufacturing.

For Chapter 2, contributors include Robert S Chisena (RSC) and Albert J Shih (AJS). RSC manufactured specimens, collected data, and developed analytical models; RSC and AJS wrote the journal article. For Chapter 3, contributors include RSC, Lei Chen (LC), and AJS. RSC conceived the model and performed finite element modeling (FEM); LC and AJS consulted on model development, application, and FEM; RSC and AJS are writing the journal article. For Chapter 4 and 5, contributors include RSC, Sophia Marina Engstrom (SME), and AJS. RSC and AJS conceived the study. RSC performed data collection and developed and coded the model. SME assisted with data collection, code writing, and code troubleshooting. RSC, SME, and AJS wrote both journal articles.

Table of Contents

List of Tables

List of Figures

List of Appendices

Abstract

Material extrusion (MEX), also known as fused deposition modeling (FDM), is an additive manufacturing (AM) process that deposits a molten thermoplastic material layer-by-layer from a heated nozzle. This thesis investigates the use of MEX in the fabrication of a thin-walled structure (TWS), such as the ankle-foot orthosis (AFO). Three requirements for the AFO and other TWSs fabricated by MEX are that they are lightweight and durable and have tunable structural stiffness.

To fabricate a lightweight TWS with a tunable structural stiffness, the layer-by-layer nature of the MEX process may be adapted to fabricate complex internal geometries within a part. The wave infill, which uses a sine wave pattern to fill the TWS, is one method for designing such an interior within a TWS. The key advantage of the wave infill is that its truss-like structure can minimize TWS mass and homogenize the TWS for characterization of its structural stiffness. The effect of the wave infill geometry on four metrics – stiffness, load capacity, fabrication time, and mass – was studied. Analytical models were developed that predicted these metrics to within 10% of experimental measurements. The analytical models were used to develop a composite simplification model (CSM) of the wave infill in TWSs with generalized geometries. In CSM, the wave infill and TWS faces are modelled as a homogenous stacked composite, which reduces computation and setup time. CSM for the wave infill was found to predict the stiffness of experimental measurements within 15%. An analysis performed on several geometries and loading conditions shows CSM to be a powerful finite element tool that can optimize the wave infill for TWSs.

To fabricate a durable TWS, interfacial weaknesses between layers due to voids from the MEX fabrication process must be inspected to allow for the improvement of MEX process parameters. Computed tomography (CT) is a non-destructive method for quantifying void density at MEX layer interfaces. An advanced segmentation technique called the Mixed Skew Gaussian Distribution (MSGD) method was developed to improve processing of CT AM part analysis. The MSGD method predicted the porosity of an AM specimen from the National Institute of Standards and Technology (NIST) to within 1% of its experimentally measured value. MSGD was applied to quantify the internal structure of a MEX filament and part. For the MEX part, average void area was found to be highest (>250 μm^2) at the bottom of the layer and smallest (<100 μm^2) at the top of the layer, which could be explained by a large temperature gradient between layers and contractile thermal stresses inside the layer that causes the thermoplastic to have increased shrinkage resulting in larger voids.

Overall, this thesis shows: (1) the wave infill can be used to generate a lightweight TWS with tunable structural stiffness, (2) CSM is a powerful finite element technique that may be used to design MEX wave infill TWSs, (3) CT and MSGD may be used to quantify the internal structure of MEX filaments and parts, and (4) voids from the MEX process occur at interfaces between layers, possibly due to large thermal gradients and plastic shrinkage. This research will inform and improve the MEX fabrication process to fabricate TWSs with tunable structural stiffnesses that are lightweight and durable.

Chapter 1
Introduction

1.1 Material Extrusion: Fabricating a Durable, Lightweight Thin-Walled Structure with Tunable Structural Stiffness

The ankle-foot orthosis (AFO) is a device that is used to support and correct the foot and leg orientation of patients with drop-foot syndrome and other pathologies during walking. The conventional fabrication process for the AFO is shown in Figure 1.1. The process for fabricating an AFO is to capture the shape of the patient's limb using a plaster cast, fill the cast with plaster to generate a positive mold, vacuum form a thin thermoplastic sheet around the plaster mold, and cut the device trimline to create the final product. The trimline, material, and the thickness of the thermoplastic sheet determines the bending stiffness of the final AFO. Bending stiffness, the resistance to angular deformation of the AFO due to ankle joint bending moment M_X (Figure 1.2), is a key metric for patient outcomes [1]. Limitations with this conventional fabrication process include that the process is time consuming, labor and material intensive and geometry and shape limited.

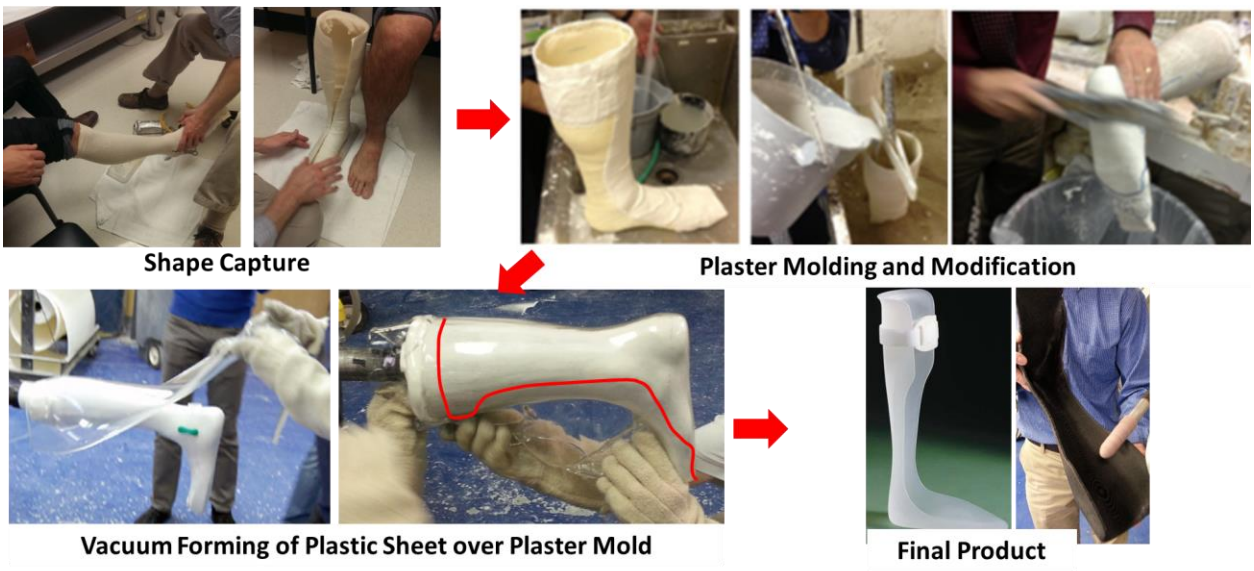

Figure 1.1. Conventional manufacturing practice for the AFO.

Figure 1.2. Bending moment, M_X, about the ankle joint of the AFO

Material extrusion (MEX), also known as fused deposition modeling (FDM), is an additive manufacturing (AM) process that offers a potential solution to the fabrication of the AFO because it can quickly and cost-effectively manufacture complex parts. In MEX, a molten thermoplastic material is deposited layer-by-layer from a heated nozzle [2]. A schematic of the MEX process is provided in Figure 1.3. MEX is increasingly being used in the fabrication of thin-walled structure (TWS) parts for high-performance, end-use applications in fields such as medicine and aerospace

[3–6]. An example application of a TWS fabricated by MEX is the AFO (Figure 1.5(a)). Three requirements for the AFO and other TWSs fabricated by MEX are that they are lightweight and durable and have a tunable structural stiffness. This thesis investigates the use of the layer-by-layer MEX process to fabricate TWSs with these requirements. Section 1.2 demonstrates the applicability of MEX to fabricate an AFO with similar stiffness and patient outcomes as the conventional manufacturing process.

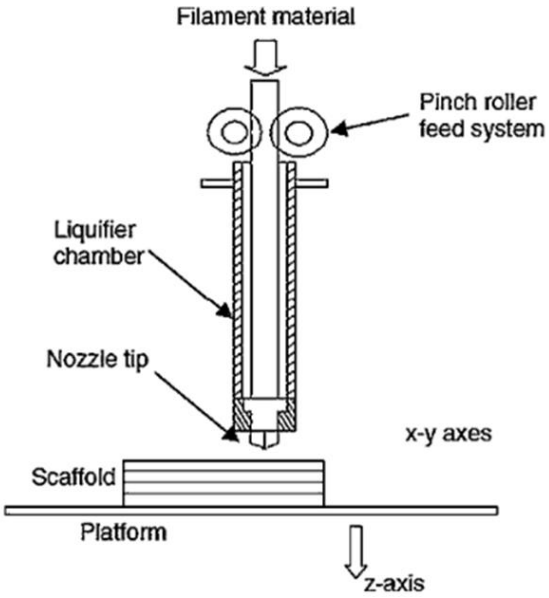

Figure 1.3. MEX process for depositing molten thermoplastic material layer-by-layer [2]

To fabricate a lightweight TWS with a tunable structural stiffness, the layer-by-layer nature of the MEX process may be adapted to fabricate complex internal geometries within a part. For a TWS such as the AFO that is primarily subjected to bending deformations during use (Figure 1.5(a)), internal geometries within the TWS allow for lightweighting and tuning of the structural stiffness of the part. During four IRB-approved subject trials performed at the University of Michigan Orthotics and Prosthetics Center, AFO weight was one of the main concerns provided by the users. Additionally, AFO stiffness has an impact on users' gait [1]. The wave infill is one method for designing an interior that allows for lightweighting and structural stiffness tuning of a

TWS. The wave infill uses a sine wave pattern to fill the TWS between its two outer facings. The key advantage of the wave infill is that its truss-like structure can minimize TWS mass and homogenize the TWS for characterization of its structural stiffness. Chapters 2 and 3 of this thesis investigate the use, design, and modelling of the wave infill for a MEX TWS. Sec. 1.3 provides further detail on the background and review of the MEX wave infill. Specifically, the research aim of Chapter 2 will be to study the effect of the uniform wave infill geometry on the stiffness and mass of the TWS. Chapter 3 aims to model the stiffness of wave infill TWSs with generalized geometries and loading conditions.

To fabricate a durable TWS, interfacial weaknesses between layers due to voids from the MEX fabrication process must be inspected to allow for the improvement of MEX process parameters. During the layer stacking process, molten thermoplastic material from the nozzle is deposited onto a previously cooled layer. During deposition and cooling of the molten material, voids form or are entrapped between layers. These voids contribute to the structural anisotropies that are inherent in MEX structures. To minimize the voids that contribute to these anisotropies, non-destructive inspection techniques may be used to visualize internal MEX structures, which can be used to improve MEX processes and mechanical strength. Chapter 4 and 5 of this thesis investigate the use of non-destructive computed tomography and a segmentation algorithm to visualize and quantify the internal structure of MEX materials. Sec. 1.4 provides further detail on the background and review of the inspection of voids using CT. Specifically, Chapter 4 aims to quantify CT data for physical insight into the internal structure of AM parts. Finally, Chapter 5 aims to apply methods developed in Chapter 4 to investigate the internal structure of MEX filaments and parts.

1.2 Comparison of MEX and Conventional AFO

To ensure that the MEX and conventional AFO were similar, two devices were tested and compared according to the following protocol. The right foot and leg of a healthy subject was scanned (Omega, WillowWood, OH), and the scan was modified (Standard Cyborg, CA) to create both the adjusted positive model and the 3D model of the AFO. From the adjusted positive model, a foam model was created using a CNC carver. A standard 4.75mm polypropylene sheet was thermoformed around this model, and trimlines were cut to create the conventional AFO device. From the 3D model, a MEX machine (Fortus, Stratasys, MN) was used to fabricate a 4mm thick, fully dense Nylon AFO. Both AFOs were subjected to a stiffness test (Figure 1.4(a)) using a custom mechanical testing device. This device measures angular deflection and torque about the AFO ankle axis. Average stiffness of the AFO is obtained by applying a linear fit to the torque-deflection curve (Figure 1.4(b)). Under an IRB approved protocol, a healthy subject walked with regular shoes and with the two AFOs while gait parameters were recorded using inertial measurement units (IMUs) (Legsys, BioSensics, MA). A Fisher Pairwise Method for one-way ANOVA was used to determine statistical difference ($P<0.05$) between the three conditions. Average stiffness of both AFOs were similar – 3.8 N-m/deg – compared to cited stiffness ranges [7]. Gait analysis demonstrated that stride length, right-side knee angle at contact, and left and right-side knee flexion during swing were statistically similar between AFOs but different from the regular shoe condition. However, the AFOs performed statistically differently in step length and left and right-side stride duration. In a survey, the subject revealed the printed AFO better limited the foot's motion during gait. MEX of AFO has been shown to produce statistically similar gait results in a healthy subject compared with traditionally manufactured AFO.

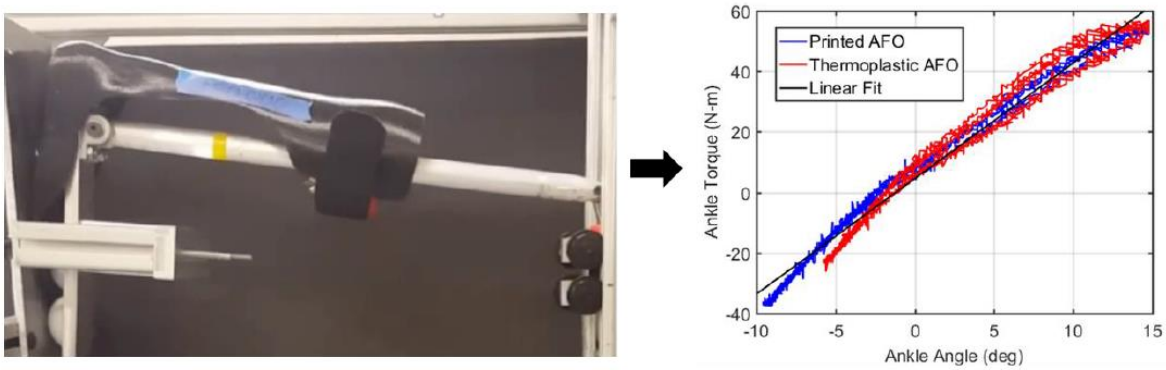

(a) (b)

Figure 1.4. (a) AFO mechanical tester measuring stiffness of printed AFO, (b) resulting stiffness curves for both AFOs and average linear fit

1.3 Material Infill for the Layer-by-Layer MEX TWS

To fabricate a lightweight TWS with a tunable structural stiffness, the layer-by-layer MEX process is described. In MEX, a TWS is divided into layers. These layers typically consist of a long, thin contour region. An example of the contour region in an AFO is shown in Figure 1.5(b). To provide stiffness to the structure, this thin region needs to be filled using an infill strategy or toolpath, which may significantly influence the fabrication time, weight, structural stiffness, and strength of a TWS. Three common MEX toolpaths for an AFO are illustrated in Figure 1.5(c)-(e). The most common infill toolpath is the direction-parallel infill (Figure 1.5(c)-(d)), which deposits line-segments, or rasters, parallel to a pre-defined vector [8]. The line width, known as beadwidth, W, and the distance between line segments, P, are two important MEX process parameters in direction-parallel infill. The direction-parallel infill can be used either for the dense infill (with $P = W$ in Figure 1.5(c)) or porous infill (with $P > W$ in Figure 1.5(d)). For the TWS, the direction-parallel infill requires lines that are short in nature, leading to many sharp corners. With the MEX machine's heavy extruder head, which comprises the nozzle, heater, and drive motor, the acceleration of the extruder head is limited, and fabrication time for the TWS with many sharp corners is increased [8]. Another infill toolpath, as shown in Figure 1.5(e), is the contour infill,

which is the successive offsetting of the boundary by the beadwidth towards the mid-plane [8]. However, this toolpath is not suitable for creating a porous core optimized for TWS bending.

The direction-parallel and contour infill toolpaths have been studied for MEX fabrication time, mass, and structural properties such as stiffness and strength in the areas of toolpath planning [9,10] and structural optimization [11–17]. In toolpath planning, Jin et al. [9] developed an algorithm to maximize the length of the direction-parallel line segments to reduce the number of sharp corners. By searching possible direction-parallel angles, the average extruder head speed could be increased. Han et al. [10] identified grouping strategies for the direction-parallel infill to reduce fabrication time. However, these studies did not discuss an efficient toolpath method for filling a TWS.

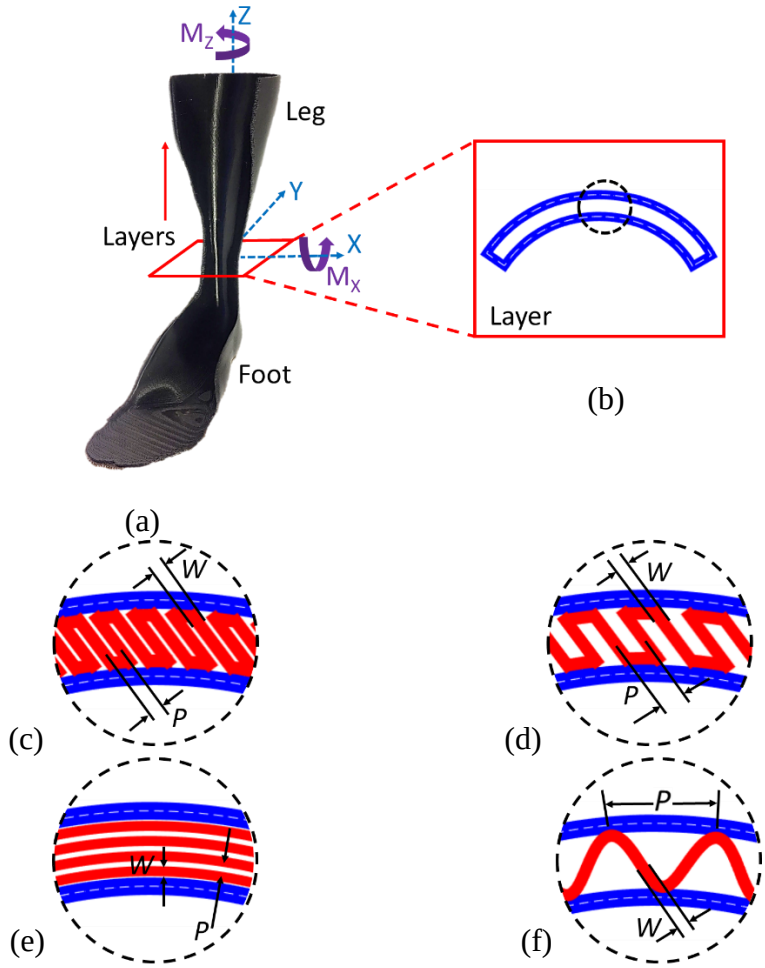

Figure 1.5. The AFO (an example of a TWS) fabricated with MEX: (a) the AFO in the fabrication orientation during MEX with layers stacked in the Z-direction and a cross-section of the layer, (b) the long, thin contour region of the TWS, (c) dense direction-parallel infill, (d) porous direction-parallel infill, (e) contour infill, and (f) wave infill.

Within structural optimization, Mohamed et al. [11] reviewed studies relating structural properties such as strength and stiffness of MEX parts to process parameters such as direction-parallel angle, beadwidth, and porosity. Ang et al. [12] developed an empirical relationship between the internal porosity of direction-parallel infill and compression stiffness and strength of a MEX part. Additionally, topology optimization, a tool that identifies an optimized porous structure, has been used for structural optimization of MEX parts [13–17]. Smith et al. [13] investigated truss beams with minimum mass for large civil structures. Wu et al. [14] optimized truss-like structures within a MEX part to mimic trabecular bone. Wu et al. [15] developed self-supporting rhombic infill structures for application-specific loading conditions. Roger et al. [16]

quantified the infill porosity of a direction-parallel MEX part subjected to pre-specified loads. These studies, however, did not investigate a porous core optimized for the MEX of a TWS under bending.

The wave infill is an ideal porous structure for the TWS under bending. Topology optimization of a beam under bending generates an optimized truss structure that has a wavy (similar to Figure 1.5(f)) and not square-like core [17]. This finding inspired the sine wave infill as shown in Figure 1.5(f) to minimize weight and compliance of a TWS beam. Additionally, the wave infill, which fills the interior of a layer with a sine wave, can reduce the MEX fabrication time of a TWS compared to the direction-parallel infill (to be presented later in Appendix E). In the past, a wave core has been used in the MEX of concrete structures in civil engineering [18], in creating efficient support structures [19], in lightweight corrugated mediums for packaging [20,21], and in tuning the structural properties of parts [22]. Further, contour generation techniques for the MEX wave infill have been described [23]. However, the research on flexural stiffness and load capacity of wave infill for MEX of the TWS is still lacking. This thesis investigates the wave infill for a TWS fabricated by MEX.

One of the key advantages of the MEX of the wave infill is that the thickness and frequency of wave infill shape may be continuously varied throughout the TWS depending on the loading, deflection, and geometry requirements. To properly design the wave infill core for generalized geometries and loadings, computational analyses should be investigated. This thesis studies the finite element composite simplification model (CSM) for TWSs with MEX wave infill and the application of CSM for design.

Analytical methods have been developed to model the flexural stiffness and strength, manufacturing time, and mass of MEX wave infill TWS specimens [3]. Computational analyses

of wave infill-like corrugations within the TWS have been studied in the packaging industry. Paper corrugations are used for stiffening the TWS while maintaining a low weight. A high stiffness-to-weight ratio is required to protect components within paper packaging while minimizing shipping costs. Previous computational analysis methods for corrugated paper board are in two categories [24]: (1) the full-scale finite element model (FEM) of the corrugated geometry including internal core geometry and (2) the homogenization of the wave geometry using CSM. The full-scale FEM of the corrugated geometry provides an accurate local analysis of the stresses within the entire TWS geometry and can predict the failure and buckling of the internal structure [25–27]. Along with increased accuracy, however, comes extensive model setup and computational time and cost. The CSM, in which the bulk properties of the corrugations and faces are modelled as a stacked composite, has a significantly lower computational and setup time compared to full-scale FEM [24]. Furthermore, the complex geometry of the corrugations does not need to be modelled, allowing for optimization without iterations of geometry remodeling and remeshing. CSM provides a generalized overview of the stresses and strains of the corrugated TWS under loading [28–30]. The improved computational time comes at the expense of the precise representation of the internal and localized corrugation of the TWS, which is acceptable for TWS studies that require infill design optimization for only the bulk deflection properties (as opposed to detailed failure mechanisms). It is the goal of this thesis to develop the CSM to characterize the bending of generalized MEX TWS with wave infill.

The mass of the TWS is an important objective in design. Minimizing the mass of the TWS, which is influenced by the geometry of the MEX wave infill, while achieving a desired structural stiffness is investigated in this study. Optimization of AM structure sizing and topology has been studied in the past [15,16,31]. In sizing and topology optimization, the optimal thickness

and connectivity, respectively, of a structure is determined by a minimum mass or compliance optimization [17]. There is a lack of research on the non-uniform wave infill in the TWS to minimize its mass. It is the goal of this thesis to apply the CSM to a TWS to demonstrate the design of a minimum mass structure with a non-uniform wave infill. Findings from this thesis can be applied to design and optimize the wave infill TWSs subjected to generalized loads.

1.4 Inspection of Interfacial Voids using Computed Tomography for the Layer-to-Layer MEX Process

To fabricate a durable TWS, inspection of voids that cause interfacial weaknesses between layers is discussed. Several studies have investigated voids during the MEX layer stacking process [32,33]. These voids are expected to contribute to the anisotropic material properties found in MEX thermoplastics. For example, for a nylon thermoplastic with embedded short carbon fibers, a commonly used high-performance MEX material, a high degree of anisotropy is demonstrated by the large differences between the in-plane (63.4 MPa) and layer-to-layer (28.9) strengths of the material [34]. In studies [32,33], only macroscopic structural voids, as shown in Figure 1.6, that occur in the gaps between MEX filaments were identified. In addition to these macroscopic structural voids, this thesis hypothesizes that smaller voids occur in the necking region between layers, which may contribute to weaknesses at the interfaces of MEX parts.

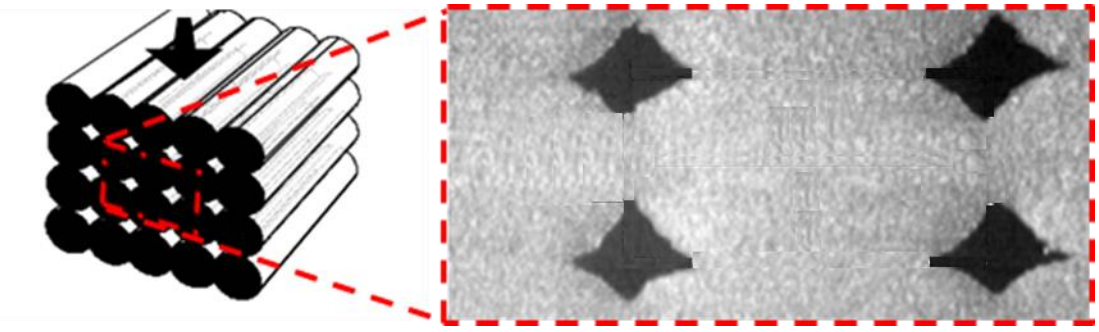

Figure 1.6. Macroscopic structural voids that occur due to the layer-by-layer MEX stacking process [32]

Because of the voids that are expected to form during the layer-to-layer MEX process, inspection of MEX materials is important to improving MEX process parameters. Inspection techniques including destructive [11,35–38] and non-destructive testing (NDT) methods [39–43] have been utilized to inspect the structure of MEX parts. Destructive testing methods such as tensile, bending, compression, and impact tests provide macroscopic characterization of MEX parts and fabrication processes but provide little information about the internal structure. Scanning electron microscopy (SEM) creates high-resolution images of an external surface but can only examine external surfaces. Microtome cutting is used to expose the internal surfaces of a part for SEM (Demuth, Benjamin. Stratasys, Eden Prairie. (May 24, 2017). Personal Interview), but the process is complex and the slicing cut may melt and/or deform the plastic and cover the pore.

NDT techniques, such as ultrasound and X-ray tomography, exist for measuring porosity and quantifying the internal structures of MEX parts. Ultrasound can identify internal voids [39], but voids less than 0.5 mm in size are difficult to identify due to limitations of sound penetration depth and resolution associated with the sound wavelengths [40]. With the use of X-rays and reconstruction techniques, computed tomography (CT) can visualize the internal structure of a specimen with sub-μm scale resolution [44].

In CT, X-rays are condensed onto a rotating specimen. Upon passing through the specimen, the concentrated X-ray is attenuated linearly according to the regional density at the exposed location. For example, a higher regional density corresponds to higher X-ray attenuation, and a lower regional density corresponds to lower X-ray attenuation. The attenuated X-ray is projected onto a 2D detector plate for each rotational angle, and the resulting X-ray intensity is recorded. A reconstruction procedure is then used to assign a grayscale value, which is linearly mapped from the measured X-ray intensity [44], to each incremental volume, or voxel, throughout the part [44].

From the 3D volume, 2D image slices are generated. A schematic of the CT process is shown in Figure 1.7.

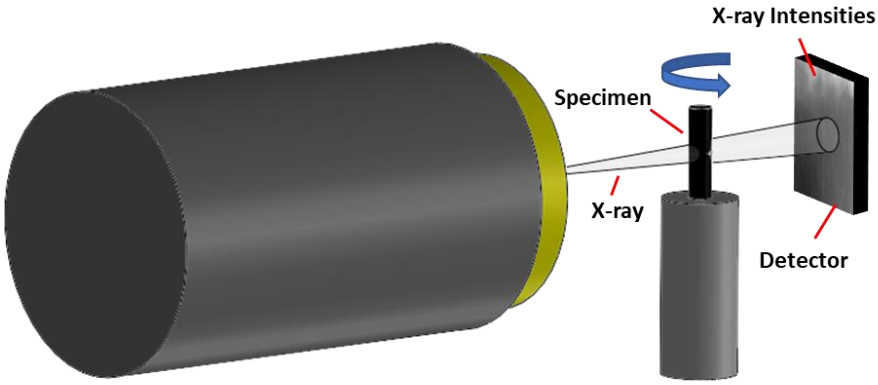

Figure 1.7. Computed tomography schematic. X-rays are condensed onto a rotating specimen, and, after passing through the specimen, the resultant X-ray intensities are recorded on the detector plate and reconstructed into a 3D volume.

CT provides visual data that may be utilized to identify boundaries between phases, or components, within the inspected part. To identify these phase boundaries, CT resolutions from 0.87 µm to 12.6 µm have been applied for inspection [39,41,42,44–50]. Furthermore, techniques, such as Bernsen [51], Otsu [52], and Kittler [47] methods, have been developed to segment the CT data into the respective internal phases. Because of various randomly distributed artifacts such as noise, blurring, shadowing, edge effects, and imperfect material and beam size that occur during the CT process [46], the choice of the CT resolution and segmentation technique is a critical aspect of the post-processing and analysis of the CT images.

The National Institute of Standards and Technology (NIST) in the United States is actively evaluating techniques and standards for measuring the porosity of materials fabricated by AM [39,42]. Experimental measurements of porosity such as with Archimedes method give a macroscopic measurement of part porosity. CT analyses provide local data of the entire part and, thus, require large amounts of data. To process this large data set, a thresholding algorithm that is easy-to-use and models the inherent randomness of CT data is required. This thesis advances a

class of statistical global image analysis techniques, called mixed Gaussian Distribution (MGD) clustering, to analyze data from CT inspections of AM parts. This method is able to determine phase volume percentages and provide insights into the internal structure and composition of the scanned parts.

CT has been applied for inspecting the internal structure of AM parts. Van Bael et al. [48] used CT with a voxel size of 12.6 μm to study the porous structures of selective laser sintered Ti-6Al-4V scaffolds. Kerckhofs et al. [49] applied CT to measure the internal surface roughness of selective laser melted Ti-6Al-4V parts using a voxel size as small as 1.5 μm and found that CT could resolve high-roughness measurements, but not sub-μm roughness. Slotwinski et al. [39] and Kim et al. [42] measured the porosity of CoCr laser powder bed fusion parts using CT with a minimum voxel size of 0.87 μm. Bernsen's segmentation method [50] was utilized to distinguish pores from the surrounding metal and determine the distribution of pores inside the part. Chen et al. [41] analyzed the internal structure of a MEX acrylonitrile butadiene styrene (ABS) part using CT with 4 μm voxel size and demonstrated that internal porosity within MEX parts may occur at different size scales. For example, porosity within a MEX part may be due to either porosity within the deposited filament (internal bubble) or the filament stacking process (necking bubble). No study, however, has characterized the internal structures of MEX filaments and parts at the μm scale. It is the goal of this thesis to use CT to quantify the pore size, distribution, and volume percentage of a MEX filament and part.

1.5 Thesis Structure

This thesis aims to investigate the layer-by-layer nature of the MEX process to improve the fabrication of the MEX TWS. Key gaps in the literature include:

Chapter 2:

1. No previous study of lightweight MEX TWS with tunable stiffness
2. No study of efficient toolpath method for filling TWS
3. No research on the flexural stiffness and load capacity of the wave infill for MEX of the TWS

Chapter 3:

4. No efficient stiffness modeling of MEX wave infill TWSs with generalized geometries and loading conditions
5. No method that can be subjected to optimization to generate an optimized MEX TWS toolpath toolpath with wave infill

Chapter 4:

6. No application of the mixture of skewed Gaussian distributions to quantify skewed CT data due to intra-component variations

Chapter 5:

7. No investigation of layer-to-layer voids that occur within MEX parts

Chapters 2 and 3 of this thesis relate to the investigation of the MEX wave infill. Chapter 2 describes an analytical and experimental approach to characterizing four metrics of flexural beams with uniform wave infill – stiffness, load capacity, fabrication time, and mass. Chapter 3 describes the composite simplification model for finite element analysis of a generalized TWS with the MEX wave infill. Chapters 2 and 3 serve as the foundation for the optimization of the wave infill for a MEX TWS. Chapters 4 and 5 of this thesis relate to the investigation and quantification using CT of the internal structural of MEX parts. Chapter 4 describes the use of a probability-based segmentation algorithm for CT to quantify the internal structure of CT-analyzed

parts. Chapter 5 describes the application of this algorithm to a MEX filament and part. Chapter 6 provides conclusions of the thesis and future work.

Chapter 2
Analytical Characterization and Experimental Validation of the Material Extrusion Wave Infill for Thin-Walled Structures

2.1 Abstract

The wave infill for material extrusion (MEX) of the thin-walled structure (TWS) is presented. The wave infill, a lightweight truss-like porous core structure sandwiched between two outer walls, is an efficient toolpath pattern for the MEX of TWS. Analytical models for predicting the stiffness, load capacity, fabrication time, and mass were established for two orthogonal in-plane and layer-to-layer variations inherent in MEX wave infill parts. Rectangular prism, four-point flexural bending specimens representing the in-plane and layer-to-layer orientations with wave infill were fabricated by MEX of Polyamide-12 (Nylon-12) material. From these specimens, fabrication time and mass were measured, and four-point flexural tests were conducted to measure the stiffness and load capacity of the beam. Analytical models were compared with the experimental measurements to identify their predictive capabilities. Stiffness for in-plane and layer-to-layer orientations was predicted well with the relative root-mean-square error (RRMSE) of 7% and 6%, respectively. Load capacity in in-plane and layer-to-layer orientations had an RRMSE of 23% and 22%, respectively. Fabrication time and mass were predicted well with a RRMSE of 7% and 6%, respectively. The methods established in this study are the foundation for optimal design and MEX of wave infill TWSs with generalized loads.

2.2 Introduction

In MEX, a heated extruder nozzle deposits molten thermoplastic material to build a component layer-by-layer resulting in a three-dimensional part. One of the applications for MEX

is the fabrication of the thin-walled structure (TWS), which is used extensively in medical orthotics, such as the ankle foot orthosis (AFO) illustrated in Figure 1.5(a). The AFO is an assistive device commonly used to correct drop-foot syndrome in stroke patients to support their foot during walking. Customization, light-weighting, compliance, and durability are all important requirements for an ideal AFO. Therefore, a porous TWS core using MEX to fabricate the AFO with lightweight while maintaining strength is ideal [53]. This study investigates the MEX wave infill for fabricating a truss-like TWS with a porous core.

Successful fabrication and implementation of the wave infill TWS requires characterization of four metrics – stiffness, load capacity, fabrication time, and mass. Because the TWS is dominated by bending deformation, analytical models for flexural stiffness and load capacity of MEX wave infill TWS will be established. In addition, the fabrication time and mass, which relate specifically to the MEX machine's capability on acceleration and velocity, are also evaluated for wave infill MEX structures. For validation, the accuracy of four analytical models for stiffness, load capacity, fabrication time, and mass are compared with experimental measurements during fabrication and four-point bending tests of wave infill MEX beams.

In this study, an analytical model of the flexural stiffness and load capacity of a wave infill MEX beam is introduced in Sec. 2.3. The geometrical input parameters for the wave infill and directional flexural testing procedures are described in Sec. 2.4. Analytical models to predict the four metrics – stiffness, load capacity, fabrication time, and mass – of the wave infill beam are presented in Sec. 2.5 and Appendices A-D. Experimental results, analytical model validation, and a discussion of model effectiveness are elaborated in Sec. 2.6. Finally, an analysis of the analytical model for the four wave infill metrics is discussed in Sec. 2.7.

2.3 Generalized 3D Wave Infill TWS and its Flexural Bending and Directional Properties

A generalized 3D wave infill TWS and representative flexural beam are presented to describe the flexural stiffness and load capacity of a wave infill MEX part.

2.3.1 Bending of a Generalized 3D Wave Infill TWS

A MEX TWS with wave infill can be generalized as the structure shown in Figure 2.1(a). This TWS has outer contours and wave infill and is subjected to bending moments, M_X and M_Z, about its principle axes. Practically, during use, a MEX TWS (such as the AFO in Figure 1.5) experiences two primary bending moments about the TWS' principle axes, as shown in Figure 1.5(a). The flexural stiffness and load capacity of the 3D TWS with wave infill can be measured by applying moments, M_X and M_Z, about the principal axes of the TWS, as shown in Figure 2.1(b) and (c), while measuring the resulting deformation. The flexural stiffness and load capacity of the TWS will vary in orthogonal X- and Z- bending modes because the area moments of inertia are different. Two simplified sections, as shown in Figure 2.1(b) and (c), with area moments of inertia, I_Z and I_X, respectively, are used to study these differences.

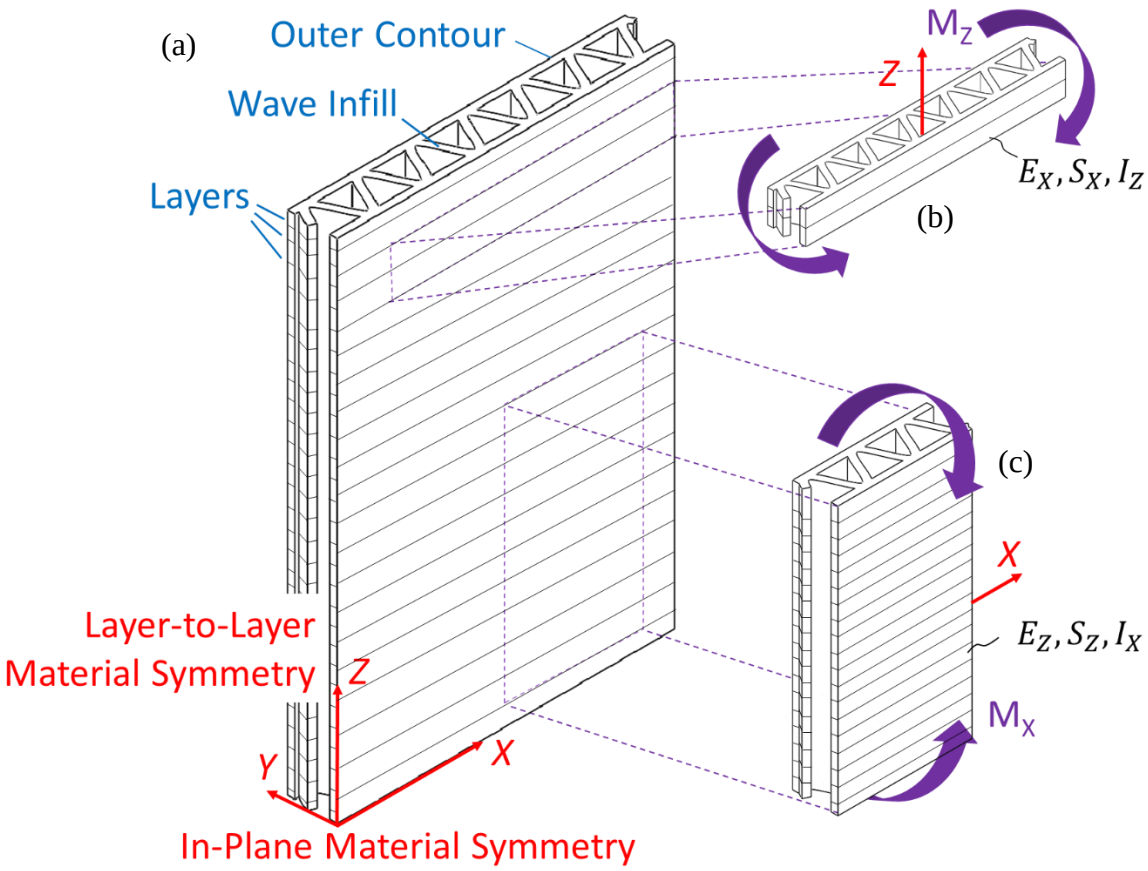

Figure 2.1. A generalized 3D MEX TWS exhibiting transversely orthotropic material properties with material symmetries within the layer (in-plane symmetry) and normal to the layers (layer-to-layer symmetry): (a) layers stacked along the Z-direction, a wave infill, and the outer contours, (b) an in-plane section of the TWS with applied moment, M_Z, about the Z-axis and beam properties of E_X, S_X, and I_Z, and (c) a layer-to-layer section of the TWS with applied moment, M_X, about the X-axis and beam properties E_Z, S_Z, and I_X.

2.3.2 Directional Properties of MEX Parts

Whereas the flexural stiffness and load capacity will differ in the two primary bending modes due to the area moment of inertia differences, the layer-to-layer MEX process itself affects the directional material properties. During MEX, the inter-layer temperature differences limit polymer cross-linking [54], reduce the layer-to-layer strength and stiffness, and yield transversely orthotropic parts [55–57]. Transverse orthotropy refers to the existence of equivalent mechanical properties within a plane of a part.

As shown in Figure 2.1(a), the XY-plane is referred to as the *in-plane* material symmetry with flexural modulus, E_X, and strength, S_X. Normal to this plane (Z-direction) is the *layer-to-*

layer material symmetry with modulus, E_Z, and strength, S_Z. Analytical models to predict the stiffness and load capacity of the wave infill geometry in the layer-to-layer and in-plane symmetry directions will be derived. Flexure specimens shown in Figure 2.1(b) and (c) will be fabricated by MEX to represent both symmetry directions. Bending experiments will be performed to validate analytical models for stiffness, load capacity, fabrication time, and mass.

2.4 MEX Fabrication, Experimental Procedure, and Design of Four-Point Bending Flexure Specimen with Wave Infill

The MEX process for fabrication of flexure beam specimens, infill constraint, and measurement results for the load capacity and stiffness of flexural beams with the wave infill are presented in this section.

2.4.1 MEX process for ASTM flexure specimen for four-point bending

To represent the symmetry directions in MEX wave infill parts, two types of flexure specimens of rectangular cross-section (120 mm in length and 10 mm in height for the in-plane specimens and 40 mm in height for the layer-to-layer specimens) were designed according to ASTM Standard D790-10 for flexural experiments [58]. Specimens were manufactured using a MEX machine (Fortus 400mc by Stratasys, Eden Prairie, Minnesota). Specimens were made by MEX from 1.75 mm diameter Nylon-12 filament, a 0.5 mm diameter nozzle, 0.33 mm layer height, 295°C nozzle temperature, and 110°C oven temperature enclosing the whole part. A 2 mm base of acrylic copolymer support material [59] was printed before the Nylon MEX. To dissolve this support material, specimens were placed in a sodium hydroxide solution (24 g/L) ultrasonic bath at 60°C.

As shown in Figure 2.2, four variables that define the toolpath centerline of the wave infill flexure specimen are:

- Beadwidth, W, is the width of the deposited thermoplastic bead and is controlled by the nozzle speed, filament extrusion rate, and nozzle diameter. In this study, W is constrained between 0.45 to 0.95 mm.
- Thickness, T, is the thickness of the rectangular specimen. In this study, T is held between 3.0 to 15.0 mm.
- Period, P, is the period of one wave of the wave infill pattern within the rectangular prism. The range of P is from 1 to 10 mm.
- Overlap, O, is the overlap of the wave infill peaks and the outer contour. O is the minimum distance between centerlines of the outer layer and the extremes of the wave. A lower value of O reduces the distance between the wave and contour centerlines, corresponding to a greater overlap of the contour and wave. The range of O is from 0.05 to 0.4 mm. Above 0.4 mm, the motion of the nozzle causes dislocation of the wave infill from the straight wall. Below 0.05 mm, the high overlap causes the material to pushout yielding dimensional errors.

These input variables are defined as a vector, $\boldsymbol{x} = [x_1, x_2, x_3, x_4] = [W, T, P, O]$. The fifth constraint, presented in the next section, limits the amount of material deposited within the TWS.

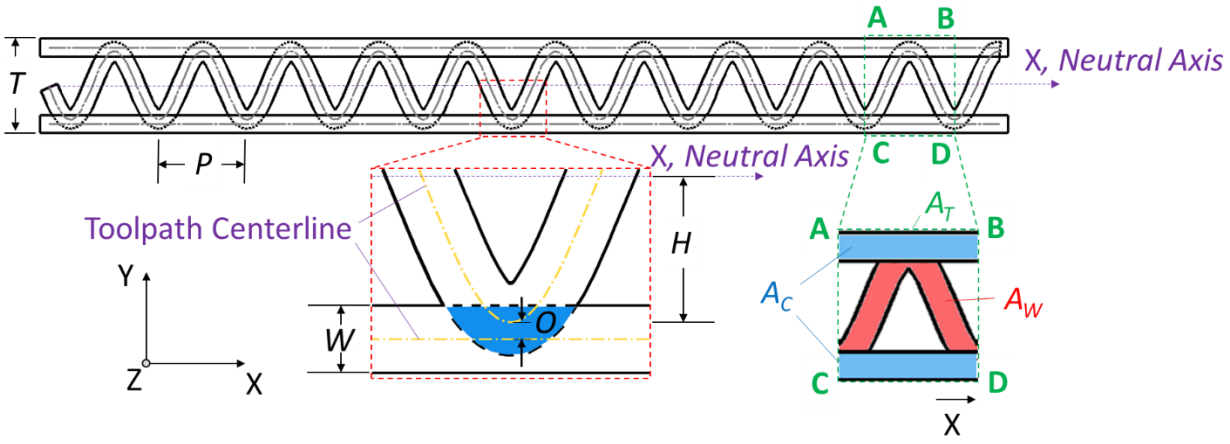

Figure 2.2. Top- or layer-schematic view of the wave infill specimen with the four input variables, W, T, P, and O that define the wave infill toolpath centerline for a TWS. The toolpath centerline is the line followed by the center of the MEX toolhead nozzle when depositing material. The area ABCD shows the contour-filled area, A_C, and total area, A_T.

2.4.2 Infill Constraint

The ratio of filled area over total area, defined as the infill ratio, F, is constrained. F can be obtained from:

$$F = \frac{A_F}{A_T} \tag{2.1}$$

where A_T is the total area and A_F is the filled area of the specimen cross-section. Within a period of the sine wave infill shown by the shaded dashed-box area in area ABCD of Figure 2.2, the total area, A_T, is:

$$A_T = P\ T \tag{2.2}$$

A_F in area ABCD of Figure 2.2 consists of the areas of outer contours, A_C, and the wave, A_W:

$$A_F = A_C + A_W \tag{2.3}$$

The area of the outer contours, A_C, shown in area ABCD of Figure 2.2, is:

$$A_C = 2\ P\ W \tag{2.4}$$

To find the area of the wave in area ABCD, the toolpath mid-line of the wave, as shown in Figure 2.2, is defined as a sine wave, $y(x)$:

$$y(x) = H \sin\left(\frac{2\pi}{P}\ x\right) \tag{2.5}$$

where x is the parameterized distance along the wave (Figure 2.2) and, the wave amplitude, H, is:

$$H = \frac{T}{2} - \left(\frac{W}{2} + O\right) \tag{2.6}$$

The area of the wave, A_W, is:

$$A_W \approx L_{wave} W \tag{2.7}$$

where L_{wave} is the length of the wave within the area of interest calculated from the arc length [60]:

$$L_{wave} = \int_0^P \sqrt{1 + \left(\frac{2\pi}{P} H \cos\left(\frac{2\pi}{P} x\right)\right)^2}\, dx \tag{2.8}$$

which can be approximated numerically. In this analysis, the density and cross-sectional area of the deposited bead were assumed constant throughout the area of interest.

The infill ratio, F, constraint limits the wave infill design from overfilling or under-filling the interior of the flexure specimen. By observing the wave infill of specimens, the range of allowable F was found to be between 50 to 90%. For F below 50% (under-filling), the outer contours were prone to buckling during testing. For F above 90% (overfilling), the part is a solid or is close to a solid, and its dimensional accuracy was affected. Figure 2.3(a) and (b) show a wave infill specimen with low infill ratio, 54%, and a high infill ratio, 88%, respectively.

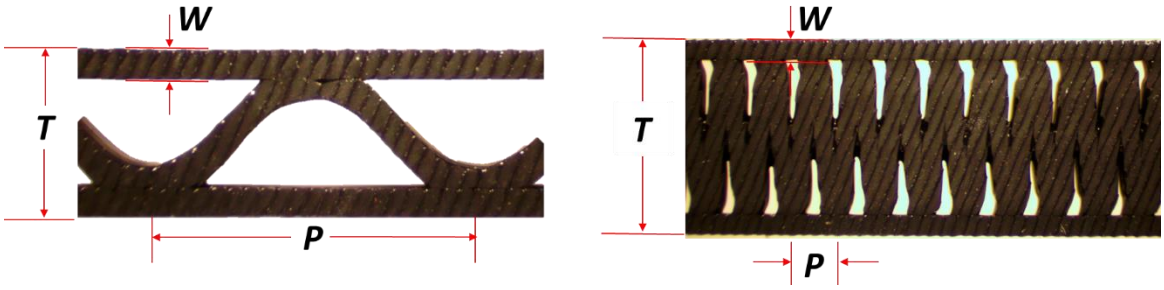

(a) (b)

Figure 2.3. Example wave infill specimens with (a) 54% and (b) 88% infill ratio. Note that the diagonal lines on the printed surface are from the imprint of an adjacent layer of support material.

2.4.3 Measurements of Bending Stiffness and Load Capacity

The ASTM Standard D790-10 four-point flexural tests [58], as shown in Figure 2.4, were performed. Four-point tests, as opposed to three-point, are used to increase the length of the constant moment distribution through the mid-length, a, between the two top, inner loading pins on the porous flexural specimens with wave infill. The length, l, of each specimen was 120 mm. Two types of specimens, one representing the in-plane symmetry direction (10 mm x T x 120 mm in Figure 2.4(a)) and the other representing the layer-to-layer symmetry direction (40 mm x T x

120 mm in Figure 2.4(b)) were subjected to bending moments M_Z and M_X, respectively, in four-point bending tests. The spacing between two outer (bottom) loading pins is L_S. In this study, L_S = 80 mm and a = 30 mm. Bending tests were performed on a 10 kN material testing machine (MTS Insight 10 Mechanical Tester, MTS, Eden Prairie, MN).

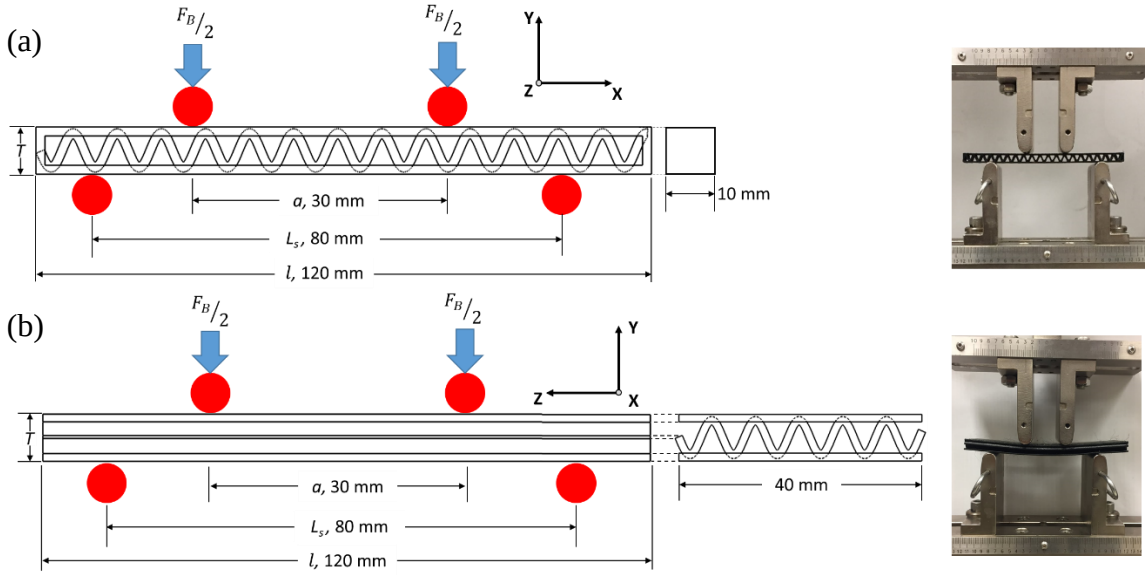

Figure 2.4. Four-point flexure test setup in (a) in-plane and (b) layer-to-layer specimen orientation.

The load on the top two inner pins, F_B, vs. cross-head displacement, δ, in the four-point bending tests were recorded. A sample measurement is shown in Figure 2.5. The stiffness K is the slope, and the load capacity L is the peak load of F_B vs. δ curve. A tangent line was fit to the user-defined linear region, using the MATLAB *fit* function, to find the slope and stiffness, K.

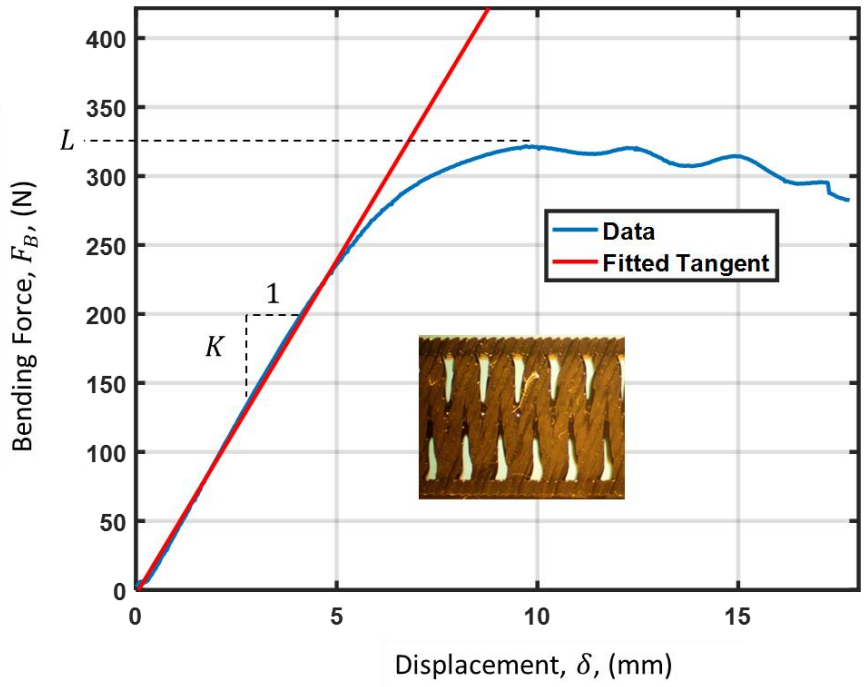

Figure 2.5. Four-point bending load vs. displacement curve for in-plane Experiment 1 (Table 2.1) with fitted tangent in linear region corresponding to the flexural stiffness, K, and horizontal dotted line corresponding to peak load, L, of the specimen.

2.4.4 Outputs from Flexural Experiments and Comparison with Analytical Models

The four-point bending experiments have four measurement outputs: K_X^E and K_Z^E (measured stiffness for in-plane and layer-to-layer specimens, respectively) and L_X^E and L_Z^E (measured load capacity for in-plane and layer-to-layer specimens, respectively).

Analytical models, K_X^A, K_Z^A, L_X^A, and L_Z^A, are derived to predict the K and L of the directional MEX wave infill specimens. K_X^A and K_Z^A represent the analytically predicted stiffness for in-plane and layer-to-layer specimens, respectively. L_X^A and L_Z^A represent the analytically predicted load capacity for in-plane and layer-to-layer specimens, respectively.

Analytical models K_X^A, K_Z^A, L_X^A, and L_Z^A are validated by comparing with experimentally measured K_X^E, K_Z^E, L_X^E, and L_Z^E of four-point bending flexural specimens with wave infill. To ensure analytical models for K and L are accurate across the whole space of four input variables $[W, T, P, O]$, a systematic experimental approach based on the Latin Hypercube Sampling (LHS)

[61] is applied. Each of four inputs was divided into equidistant levels within their respective bounds. For each equidistant level, combinations of each level from each input variable are sampled once, never repeating levels. With these combinations, the LHS approach allows a uniform sampling of the entire design region. Every set of inputs $[W, T, P, O]$ was also checked to ensure it was within the infill ratio of 50% < F < 90%. The Matlab function *lhsdesign* was used.

- In-plane specimens: The four inputs were segmented into 75 equidistant segments in LHS to create 75 combinations. After checking the F of this set of 75 LHS-sampled design variables, 19 experiments, listed in Table 2.1, met the constraint (50% < F < 90%). From these 19 design variable sets, 19 in-plane MEX flexural specimens with wave infill were fabricated and experimentally tested by four-point bending to validate analytical models for X-direction stiffness and load capacity.
- Layer-to-layer specimens: the set of 19 experimental variables were reduced to a set of 7 variables (listed in Table 2.2) for four-point bending testing of layer-to-layer flexural specimens. These 7 layer-to-layer MEX specimens were fabricated and experimentally tested to validate the analytical predictions for Z-direction stiffness and load capacity.

Top-view microscope images of each of the fabricated specimens are shown in Figure 2.6.

2.4.5 LHS Experimental Variable Distribution

Using the LHS method, the design region was sampled uniformly for efficient experimental validation of the analytical models for wave infill. Table 2.1 and Table 2.2 show each of the LHS generated experimental variables and the corresponding F for in-plane and layer-to-layer specimens, respectively. Table 2.1 shows the constrained design region, according to Secs. 2.4.1 and 2.4.2, along with the maximum, minimum, and average in-plane and layer-to-layer variable distribution from LHS. Table 2.3 shows that the center and boundaries of the design space were

sampled uniformly to test deviations of the model from experimental measurements throughout the design region. Each variable, except for P, had an average sample near the center of the design region. Because of the minimum restriction on infill ratio determined predominately by a specimen's period, LHS specimens were biased toward a lower wave infill period.

2.4.6 Fabrication Time and Mass Outputs

During printing, the fabrication time, or cycle time per layer, τ^E of the 19 in-plane wave infill specimens were measured. Upon completion of the part and removal of the support material, the mass M^E of each wave infill specimen was measured. Analytical models to predict wave infill fabrication time τ^A and mass M^A are presented in Sec. 2.5.3 and 2.5.4, respectively.

Table 2.1. Experimental variables, infill ratio, and experimental and analytical flexural stiffness, flexural load capacity, fabrication time, and mass of in-plane wave infill specimens. (for Nylon-12 E_X = 1276 MPa [62] to calculate stiffness K_X^A and S_X = 67 MPa [62] to calculate load capacity L_X^A)

Experimental Variables (mm)					Infill Ratio	Stiffness, K (N/mm)			Load Capacity, L (N)			Fabrication Time, τ (s/layer)			Mass, M (g)		
No.	W	T	P	O	F	Experiment K_X^E	Analytical K_X^A	$\epsilon_R(\%)$	Experiment L_X^E	Analytical L_X^A	$\epsilon_R(\%)$	Experiment τ^E	Analytical τ^A	$\epsilon_R(\%)$	Experiment M^E	Analytical M^A	$\epsilon_R(\%)$
1	0.80	8.79	2.00	0.22	0.88	47.3	44.8	5.1	319.5	312.5	2.2	15.3	15.1	1.7	9.0	9.1	-1.0
2	0.47	5.07	1.46	0.13	0.75	8.9	8.7	1.9	82.6	105.5	-27.7	13.9	15.5	-11.9	4.4	4.1	6.4
3	0.53	10.39	1.34	0.18	0.84	48.9	45.1	7.8	297.1	266.1	10.5	23.0	24.0	-4.1	10.2	9.3	8.9
4	0.81	7.84	2.66	0.10	0.75	37.9	35.2	7.1	256.7	274.9	-7.1	11.7	11.3	3.6	6.9	6.9	-0.5
5	0.89	5.86	2.78	0.28	0.82	20.3	19.4	4.4	173.2	203.2	-17.4	9.0	9.1	-1.2	5.5	5.8	-6.4
6	0.73	3.35	3.17	0.12	0.84	4.7	4.5	4.7	55.3	82.3	-48.8	6.7	6.5	3.2	3.2	3.3	-2.4
7	0.87	5.30	10.00	0.32	0.54	15.3	15.1	1.1	132.0	174.9	-32.5	3.9	3.2	17.9	3.3	3.6	-9.1
8	0.51	6.35	2.41	0.10	0.55	16.4	15.3	6.9	133.3	129.6	2.8	10.8	11.3	-5.0	4.1	3.8	8.0
9	0.60	9.18	2.22	0.08	0.63	37.1	38.7	-4.2	185.7	227.5	-22.5	14.5	14.4	0.7	6.6	6.4	3.6
10	0.52	3.49	2.26	0.11	0.71	4.3	4.1	6.7	50.6	62.7	-23.8	8.3	8.9	-6.2	2.8	2.7	4.2
11	0.77	4.13	3.08	0.12	0.80	8.5	7.7	8.7	89.4	101.1	-13.0	7.0	7.3	-4.9	3.8	4.0	-3.1
12	0.55	10.02	1.96	0.10	0.63	41.2	43.2	-4.8	232.7	232.6	0.0	17.9	16.8	6.2	6.3	6.9	-9.6
13	0.54	4.08	2.81	0.10	0.61	5.4	6.0	-10.5	54.2	78.9	-45.5	8.0	8.1	-1.4	2.9	2.8	4.1
14	0.64	12.14	1.89	0.22	0.72	66.2	74.1	-11.9	313.4	329.4	-5.1	19.8	18.8	5.1	10.2	9.7	4.3
15	0.46	10.77	1.39	0.05	0.72	40.5	42.8	-5.6	187.5	214.4	-14.4	23.5	23.9	-1.9	7.3	8.0	-8.5
16	0.48	14.34	2.08	0.09	0.51	88.9	80.7	9.2	467.3	303.6	35.0	20.7	19.0	8.4	7.2	7.6	-6.1
17	0.48	9.79	2.16	0.10	0.51	33.9	36.4	-7.5	186.3	200.8	-7.8	16.1	15.3	5.0	5.8	5.3	8.4
18	0.78	3.82	4.84	0.19	0.73	6.8	6.4	4.7	68.9	91.0	-32.2	5.3	5.1	3.7	3.2	3.2	-0.6
19	0.92	5.23	4.10	0.10	0.76	16.1	15.2	5.8	154.5	156.6	-1.4	7.1	6.6	7.1	4.6	4.8	-3.8
							R^2	0.982		R^2	0.866		R^2	0.984		R^2	0.973
							RRMSE	6.8%		RRMSE	23.6%		RRMSE	6.6%		RRMSE	6.0%

Table 2.2. Experimental variables, infill ratio, and experimental and analytical stiffness and load capacity for flexure of layer-to-layer wave infill specimens. (for Nylon-12 E_Z = 1180 MPa [62] to calculate K_Z^A and S_Z = 61 MPa [62] to calculate L_Z^A)

Experimental Variables (mm)					Infill Ratio	Stiffness, K (N/mm)			Load Capacity, L (N)		
No.	W	T	P	O	F	Experiment K_Z^E	Analytical K_Z^A	$\epsilon_R(\%)$	Experiment L_Z^E	Analytical L_Z^A	$\epsilon_R(\%)$
1	0.80	8.79	2.00	0.22	0.88	274.5	251.2	8.5	2383.0	1723.9	27.7
2	0.47	5.07	1.46	0.13	0.75	50.4	51.5	-2.2	531.3	612.6	-15.3
3	0.53	10.39	1.34	0.18	0.84	380.0	396.9	-4.5	2587.0	2303.7	11.0
4	0.81	7.84	2.66	0.10	0.75	176.0	170.4	3.2	1654.0	1311.0	20.7
5	0.89	5.86	2.78	0.28	0.82	82.3	84.6	-2.8	858.5	870.4	-1.4
6	0.73	3.35	3.17	0.12	0.84	20.3	18.4	9.3	243.1	331.5	-36.4
7	0.87	5.30	10.00	0.32	0.54	54.4	57.2	-5.2	525.0	650.9	-22.6
							R^2	0.992		R^2	0.963
							RRMSE	5.7%		RRMSE	22.0%

Table 2.3. LHS uniform experimental distribution for in-plane and layer-to-layer specimens

Experimental Variables	W (mm)		T (mm)		P (mm)		O (mm)		F	
Design Region (min, max)	0.45	0.95	3.00	15.00	1.00	10.00	0.05	0.40	0.50	0.90
In-plane LHS (min, max)	0.46	0.92	3.35	14.34	1.34	10.00	0.05	0.32	0.51	0.88
In-Plane LHS Average	0.65		7.37		2.87		0.14		0.70	
Layer-to-Layer LHS (min, max)	0.47	0.89	3.35	10.39	1.34	10.00	0.10	0.32	0.54	0.88
Layer-to-Layer LHS Average	0.73		6.66		3.34		0.19		0.77	

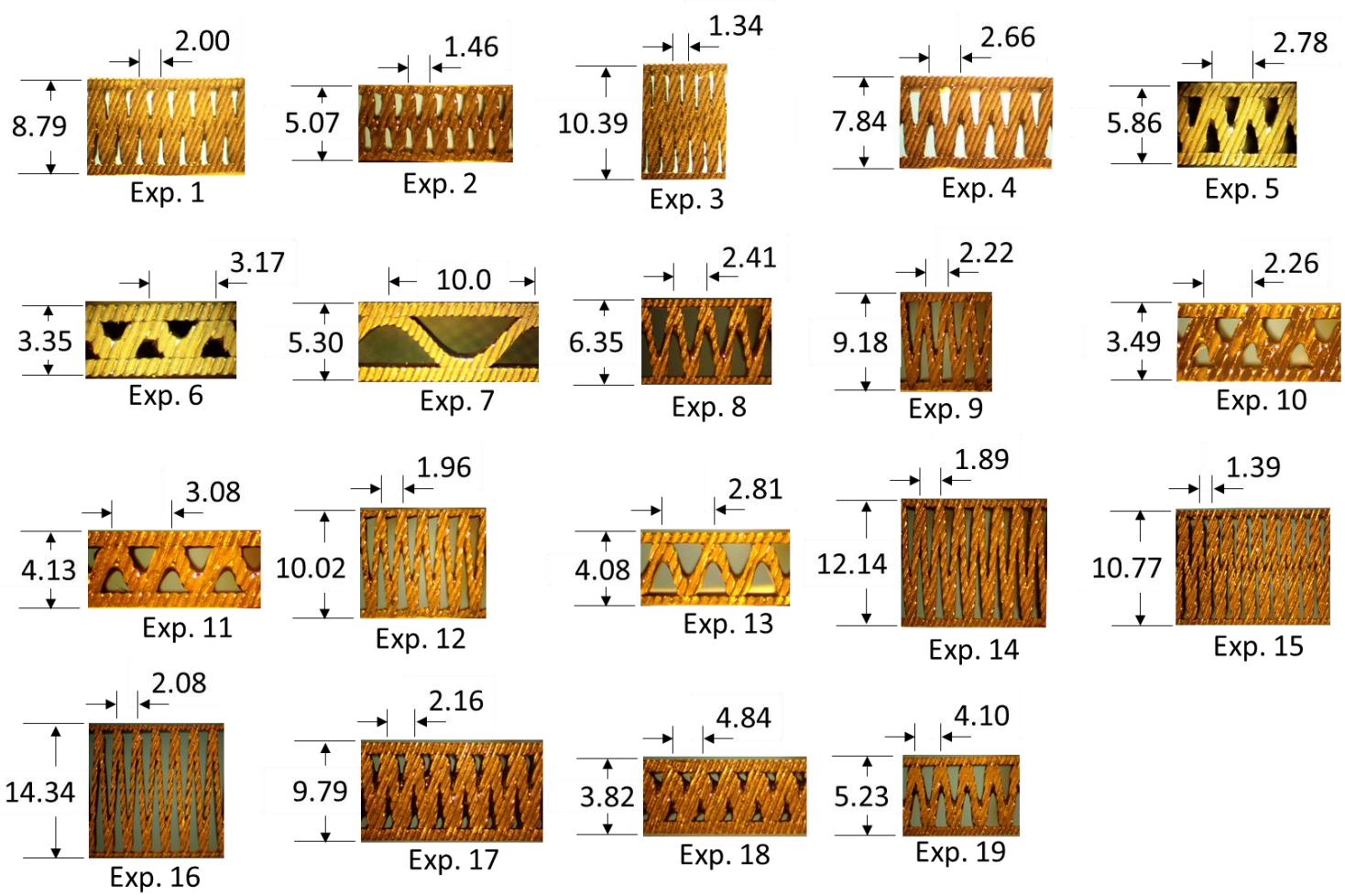

Figure 2.6. Top-view microscope images of the 19 experiment samples of MEX wave infill for validation of in-plane analytical models of stiffness, load capacity, time, and mass. The first seven samples represent the top-view of layer-to-layer models, as well. Note that the diagonal lines on the printed surface are from the imprint of an adjacent layer of support material. All measurements in mm.

2.5 Analytical Modelling of Four Wave Infill Output Parameters

Analytical models to predict the stiffness, load capacity, fabrication time, and mass of the directional wave infill flexural specimens are presented.

2.5.1 Stiffness Model

Appendix A presents details of the derivation of stiffness $K_{\bullet}^{A}$ of the four-point flexural in-plane and layer-to-layer bending specimens.

$$K_{\bullet}^{A}(\boldsymbol{x}) = \frac{48\, E_{\bullet}\, I_{\bullet}(\boldsymbol{x})}{{L_s}^3 - 3\, a^2\, L_s + 2\, a^3} \tag{2.9}$$

where ● represents the X or Z directions; $E_{\bullet}$ is either E_X or E_Z, the flexural modulus in X- or Z-direction, respectively; $I_{\bullet}(\boldsymbol{x})$ is either $I_Z(\boldsymbol{x})$ or $I_X(\boldsymbol{x})$, the area moment of inertia of the in-plane and layer-to-layer cross-sections, respectively; L_S is the support span; and a is the distance between two loading pins (Figure 2.4). The mathematic formulas for $I_Z(\boldsymbol{x})$ or $I_X(\boldsymbol{x})$ of the wave infill flexural specimens are derived in Appendices A.2 and A.3.

2.5.2 Load Capacity Model

Appendix B presents the derivation of load capacity $L_{\bullet}^{A}$ of the four-point flexural in-plane and layer-to-layer bending specimens.

$$L_{\bullet}^{A}(\boldsymbol{x}) = \frac{8\, S_{\bullet}\, I_{\bullet}(\boldsymbol{x})}{T\, (L_s - \mathrm{a})} \tag{2.10}$$

where ● represents the X or Z and $S_{\bullet}$ is either S_X or S_Z, the flexural strength in the X- and Z-directions, respectively.

2.5.3 Fabrication Time Model

The fabrication time per layer for flexural specimens with wave infill was estimated using the analytical model for fabrication time, τ^{A}, which is derived in Appendix C.

2.5.4 Mass Model

The mass of in-plane specimens was estimated using the analytical model for specimen mass, M^A, which is derived in Appendix D.

2.6 Experimental Results, Validation of Models, and Discussions

This section discusses the experimental results for each measured output for the wave infill experiments and compares the results with predicted analytical models.

2.6.1 Stiffness

The flexural stiffness $K_{\bullet}^{E}$ of each specimen was measured according to Sec. 2.4.3 and reported in Table 2.1 and Table 2.2. The model-estimated stiffness $K_{\bullet}^{A}$ was calculated according to Sec. 2.5.1 using the flexural moduli of elasticity, 1276 and 1180 MPa for E_X and E_Z, respectively, reported by the material supplier (Stratasys, Eden Prairie, MN) [62] for the conditioned Nylon-12 MEX material used in this study. Using these reported flexural moduli of elasticity values, specimen stiffness $K_{\bullet}^{A}$ was estimated. The relative error ϵ_R between the experimental and model-based estimates of specimen stiffness:

$$\epsilon_R = \frac{K_{\bullet}^{E} - K_{\bullet}^{A}}{K_{\bullet}^{E}} \tag{2.11}$$

was calculated for each experiment. Additionally, the relative root-mean-square error (RRMSE) of the n experiments is:

$$RRMSE = \sqrt{\frac{1}{n}\sum_{i=1}^{n} {\epsilon_R}^2} \tag{2.12}$$

where ϵ_R is the relative error between model-based estimates and experimental measurements. The ϵ_R was calculated for the in-plane and layer-to-layer stiffness.

As shown in Table 2.1 within the *Stiffness* column, experimental and analytical stiffness for in-plane specimens correlated well with an R^2 value of 0.982. Based on Eq. (2.12), the RRMSE was 6.8% indicating a well-fit model. Experiment 16 had the highest positive relative error between the analytical model and experimental values. In this case, the model under-predicted the average experimental stiffness by 9.2% or 8.2 N/mm. As shown in Figure 2.6, the specimen in Experiment 16 was the thickest amongst each of the experiments and was the most sparsely filled (i.e. had the lowest infill ratio). The lowest negative relative error between the analytical model and experimental values occurred in Experiment 14. The model over-predicted the stiffness by 11.9% or 7.9 N/mm. A top view of Experiment 14 in Figure 2.6 shows that it was the second thickest specimen of the specimen set, yet unlike Experiment 16, had a higher infill ratio. Both Experiments 14 and 16 also accounted for the largest magnitude absolute error between the model and experiment.

No identifiable trends between beadwidth, period, overlap and relative error for these specimens were seen. In general, as thickness increased, the model tended to over-predict the experimental stiffness. The model performed with less than 6% relative error in 10 out of the 19 cases. Notably, the model performed well at the boundaries of the design region with relative errors below 6% except for the thickest specimen (Experiment 16) and the shortest period experiment (Experiment 3). Finally, the model performed with a relative error of 6.7% or 0.3 N/mm and 9.2% or 8.2 N/mm for the most compliant (Experiment 10) and stiffest (Experiment 16) specimen, respectively.

As shown in Table 2 within the *Stiffness* column, experimental and analytical stiffness for layer-to-layer specimens correlated well with an R^2 value of 0.992. The RRMSE between the model and experiments was 5.7% indicating a well-fit model. Despite having one of the lowest

magnitude of absolute errors of 1.9 N/mm, Experiment 6 had the largest positive relative error, 9.3%, between the analytical model and experimental values. Experiment 6, as shown in Figure 2.6, is the thinnest specimen of the set with a low stiffness value. The large relative error for this experiment can be attributed to its low thickness and stiffness value and high sensitivity to comparatively small magnitude absolute errors. The lowest negative relative error occurred with Experiment 7, which, as shown in Figure 2.6, is also a sparse specimen with a comparatively low infill ratio (0.54). More importantly, Experiments 1 and 3 had the highest absolute errors of the set at 23.3 N/mm and 16.9 N/mm. As shown in Figure 2.6, these two experiments constituted the thickest specimens with the highest infill ratios, which may indicate a limitation or deviation of the model from the experimental data.

No identifiable trends between beadwidth, thickness, period, overlap and relative error were seen. However, as infill ratio increased, there was a general trend to under-predict the stiffness. The model performed with less than 6% error in 5 out of the 7 cases. The model predicted experimental stiffness for all boundary variables except maximum thickness with an absolute error less than 5.6 N/mm. Finally, the model performed with an error of 4.5% or 16.9 N/mm and 9.3% or 1.9 N/mm for the stiffest and most compliant specimens, respectively, in the set.

2.6.2 Load Capacity

The flexural load capacity $L_{\bullet}^{E}$ of each specimen was measured according to Sec. 2.4.3 and reported in Table 2.1 and Table 2.2. The model-estimated load capacity $L_{\bullet}^{A}$ was calculated according to Sec. 2.5.2 using the flexural strength, 67 and 61 MPa, for S_X and S_Z, respectively, reported by the material supplier (Stratasys, Eden Prairie, MN) [62] for the conditioned Nylon-12 MEX material used in this study. Using these reported strength values, specimen load capacity

$L_{\bullet}^{A}$ was estimated. The relative error ϵ_R between the experimental and model-based estimates of specimen load capacity:

$$\epsilon_R = \frac{L_{\bullet}^{E} - L_{\bullet}^{A}}{L_{\bullet}^{E}} \tag{2.13}$$

was calculated for each experiment. Likewise, RRMSE was also calculated for this set.

As seen in Table 2.1 and Table 2.2 within the *Load Capacity* column, prediction of specimen load capacity performed worse than the prediction of stiffness. Prediction of load capacity and failure of a specimen is a difficult task, especially with the highly variable MEX process. Various factors that affect the accurate prediction of load capacity include inconsistent bonding between the wave and outer contour, internal voids between layers [41], variations in print times, a "self-healing" phenomena of the wave infill (Figure 2.7), and high surface roughness due to temperature accumulations during the print (Figure 2.8).

As shown in Table 2.1, the analytical model and experimental load capacity values for in-plane specimens correlated with an R^2 value of 0.866 and an RRMSE of 23.6%. The load capacities of experiments 2, 6, 8, 13, and 18 were over-predicted with largest negative relative errors all greater than 25%. However, these experiments were amongst the thinnest, as seen in Figure 2.6, and the weakest of the set. Comparing these specimens with the entirety of the set, the absolute errors are within the same range as all other samples except for Experiment 16. Because of the low load capacity values associated with these thin specimens, the relative error can be sensitive to comparatively small absolute errors.

The largest positive error of 35.0% or 163.7 N was associated with the under-prediction of Experiment 16, which, as shown in Figure 2.6, is the thickest specimen, has the lowest infill ratio, and is the strongest of the set. One possible cause of the large under-prediction of Experiment 16 is that at yield stress the sharp troughs and peaks began to interact with each other increasing the

effective area moment of inertia of the bending region acting to regain its stiffness (or "self-heal" itself). This phenomenon is evident in the load-displacement plot of Experiment 16 shown in Figure 2.7. After the load reaches the specimen's initial yield point, the structure regains stiffness.

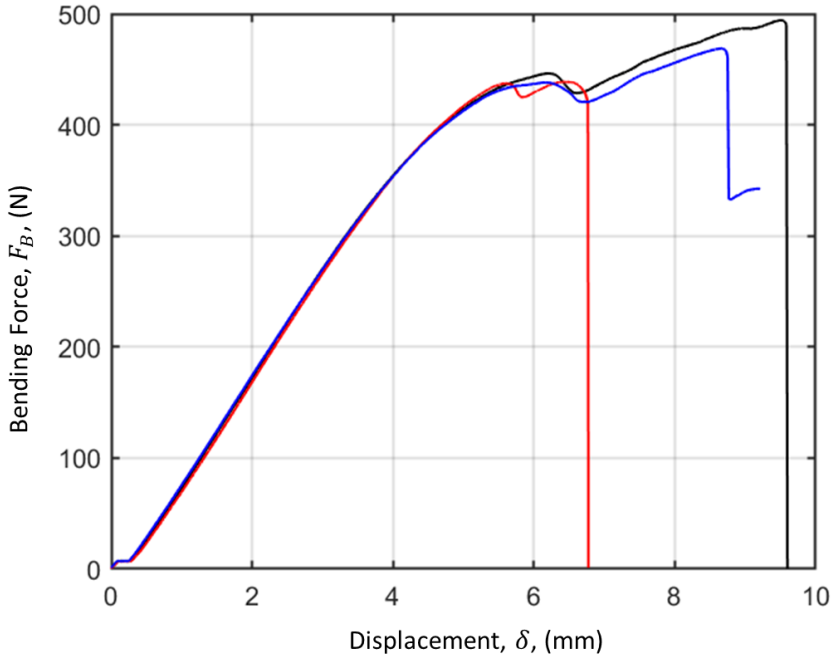

Figure 2.7. Load-displacement plot of the three experiments corresponding to Experiment 16. In two of the three experiments, the structure regains its stiffness to allow increased loading after initial yielding is reached.

No identifiable trends between beadwidth, period, overlap and relative error were seen. In general, as thickness increased, the model tended to under-predict the experimental load capacity. At the boundaries of the design region, the model predicted experimental load capacity with less than 45 N absolute error except for maximum thickness and minimum infill ratio, which both occurred in Experiment 16.

As shown in Table 2.2, model and experimental stiffness for layer-to-layer specimens correlated with an R^2 value of 0.963, and the RRMSE for the group of specimens was 22.0%. Experiment 6 was over-predicted with the largest negative relative error of 36.4%, yet it had one of the smallest magnitude absolute errors 88.4 N of the set. Again, this difference can be attributed to the thin specimen, as can be seen in Figure 2.6, with comparatively low load capacity value and

high sensitivity to absolute errors. The largest positive error of 27.7% or 659.1 N occurred in Experiment 1. Comparing Experiments 1, 3, and 4 shows that the model under-predicted the thickest specimens with the highest infill ratios, which is a limitation of the model.

Explanations for the unpredictability of the layer-to-layer load capacity may be the surface roughness that occurred during fabrication of the specimens. Because the layer-to-layer specimens are tall and thin (in both width and thickness), heat builds up rapidly, and subsequent layers are printed before previous layers can cool to the glass transition temperature resulting in surface beading and pitting as shown in a side-view of the specimen in Figure 2.8. Whereas these surface imperfections do not affect the stiffness of the parts, the load capacity prediction is significantly affected because the surface imperfections serve as stress concentrations. Among three tested samples, there were large variations, with the standard deviation of the tested samples being up to 13% of the mean value.

Figure 2.8. Side-view of layer-to-layer specimen (Experiment 7) with surface beading and pitting imperfections due to temperature accumulation during print. These surface imperfections lead to stress concentrations that affect prediction of load capacity. Layers are stacked from right to left.

2.6.3 Fabrication Time

The cycle time for the MEX nozzle to complete one layer was recorded for the 19 in-plane specimens according to Sec. 2.4.5. The model-estimated layer fabrication time τ^A for each specimen was estimated according to Sec. 2.5.3 and Appendix C using a maximum machine

velocity and acceleration of $v_m = 150$ (mm/s) and $a_m = 3000$(mm/s^2), respectively. The fabrication time measurements and estimate results are shown in Table 2.1 in the *Fabrication Time* column. The measured and estimated specimen layer fabrication times correlated well with an R^2 value of 0.984 and had a RRMSE of 6.6%. As seen in Table 2.1, the largest positive relative error of 17.9% occurred with Experiment 7, which also was the specimen with the shortest fabrication time. However, more importantly, as infill ratio increased, there was a shift from under-prediction to over-prediction, which can be seen by comparing Experiments 3 and 16. Experiment 16, the specimen with the lowest infill ratio, had the largest positive magnitude absolute error of 1.7 s. Experiment 2 had one of the highest infill ratios and was over-predicted by 0.9 s. These variations between experimentally measured and predicted fabrication times were, therefore, most likely due to variances in the expected machine dynamics that limit velocity and acceleration to ensure accurate toolpath deposition.

2.6.4 Mass

The mass of the 19 in-plane specimens was measured after fabrication according to Sec. 2.4.5. The model-estimated mass M^A for each specimen was estimated according to Sec. 2.5.4 and Appendix D using a material density for the Nylon-12 MEX material of ρ = 1.01 g/cm^2 [62]. The specimen mass measurements and model-based estimate results are shown in Table 2.1 in the *Mass* column. The measured and estimated specimen mass correlated well with an R^2 value of 0.973 and had a RMSE of 6.0%. The largest positive error of 8.9% or 0.9 g occurred with Experiment 3, and the largest negative error of 9.6% or 0.6 g occurred with Experiment 12. All mass measurements were predicted with less than 10% error or within 1 g of the experimentally

measured value. These small variations in mass could be a result of the inconsistent nature of MEX parts or small voids that are inherent in the layer-by-layer extrusion process.

2.7 Analysis of Analytical Models

This section provides an analysis of trends observed based on stiffness, fabrication time, and mass analytical models described in Sec. 2.5 and Appendices A-D for the wave infill four-point bending loading conditions and specimens described in Secs. 2.4.1-2.4.3. The trends for load capacity were similar to stiffness and are not expressly presented.

2.7.1 Stiffness

Because of the assumptions for area moment of inertia for the in-plane wave infill specimens (Appendices A.1 and A.2), the in-plane stiffness, K_X^A, (Eq. (2.9)) is affected only by T and W in the area moment of inertia term, $I_Z(\boldsymbol{x})$ (Eq. (A.6)). Figure 2.9 demonstrates the effect of T and W (i.e. Eqs. (2.9) and (A.6)) on K_X^A of the in-plane beam for $3 < T < 15$ mm and $0.45 < W < 0.95$ mm with w = 10 mm, E_X = 1276 MPa, L_S = 80 mm, and a = 30 mm. Increasing T and W both monotonically increase K_X^A. W contributes to K_X^A significantly at higher T (T > 10 mm) and negligibly at lower T values. Therefore, when designing the beam for a desired K_X^A, small stiffness magnitudes (K_X^A < 50 N/mm) can only be achieved by adjusting T. At higher stiffness magnitudes, both W and T can be altered to achieve the desired stiffness.

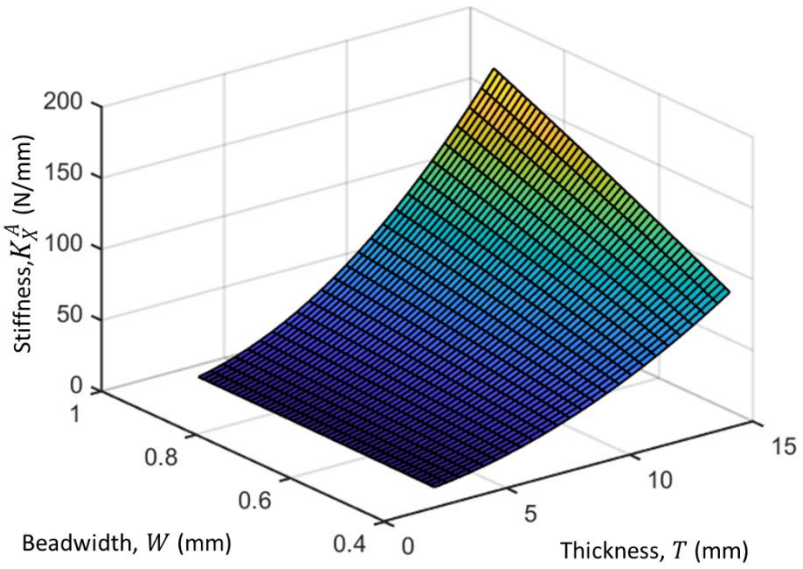

Figure 2.9. Plot of model-predicted K_X^A vs. T and W (for any P or O) with variable ranges $3 < T < 15$ mm and of $0.45 < W < 0.95$ mm and four-point beam parameters w = 10 mm, E_X = 1276 MPa, L_S = 80 mm, and a = 30 mm.

For layer-to-layer specimens, an analysis of the analytical model (Eq. (2.9) and Appendices A.1 and A.3), suggests that T and P have the most significant effect on layer-to-layer stiffness, K_Z^A. Figure 2.10 shows the model-predicted K_Z^A vs. T and P for $3 < T < 15$ mm and $1 < P < 10$ mm, W = 0.45 mm and 0.95 mm, O = 0.15 mm, and w = 40 mm, E_Z = 1180 MPa, L_S = 80 mm, and a = 30 mm. Increasing T and P yields a monotonic increase and decrease, respectively, in K_Z^A. Furthermore, P has a more pronounced effect on K_Z^A at higher T (T > 10 mm) and a negligible effect at lower T (T < 5 mm).

As shown by the two surfaces representing K_Z^A curves with W = 0.45 mm and W = 0.95 mm, W affects K_Z^A. W monotonically increases K_Z^A but has negligible effect at low T (T < 5 mm). W has a weak effect at low T because of the short distance between the neutral axis and the printed material. To take advantage of this phenomenon, W should be variably assigned within the cross-section of a TWS (i.e. increased from a minimum value at the center of the beam to a maximum value at the extremities of the beam), which will maintain K_Z^A while minimizing mass.

Although O is held constant in this analysis, it does contribute to K_Z^A. Although insignificant, a smaller value of O (i.e. higher interference between the wave peak and outer contour) increases K_Z^A of the part. K_Z^A increases due to a change in O are negligible compared to T, P, and W and are not shown graphically.

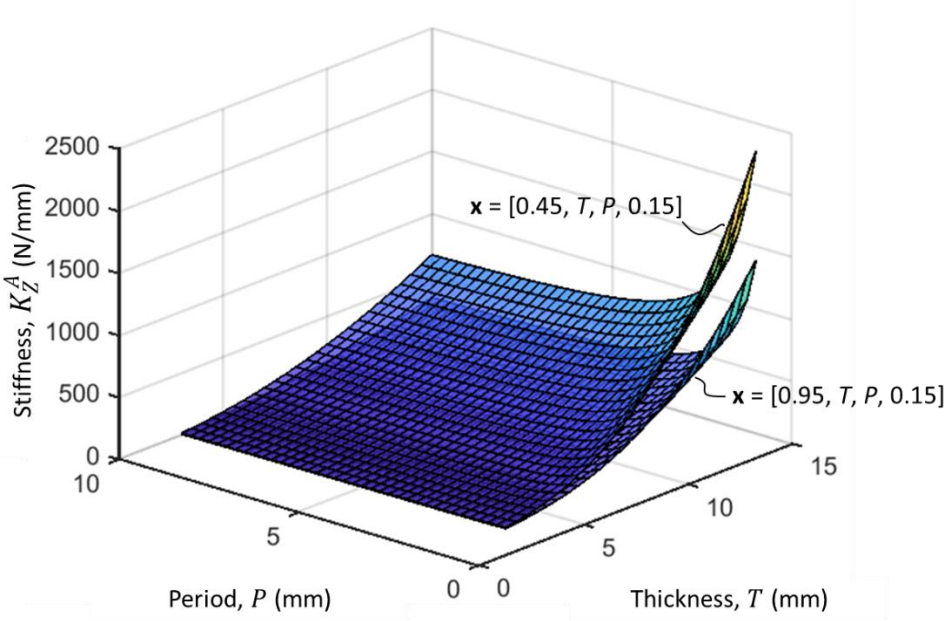

Figure 2.10. Plot of model-predicted K_Z^A vs. T, P, and W = 0.45 mm and 0.95 mm and a fixed overlap, O = 0.15 mm with variable ranges of 3 < T < 15 mm and 1 < P < 10 mm and four-point beam parameters w = 40 mm, E_Z = 1180 MPa, L_S = 80 mm, and a = 30 mm.

2.7.2 Fabrication Time

An analysis of the fabrication time, τ^A, analytical model (Appendix C) suggests that specimen T and P both significantly affect the fabrication time of the specimen. Figure 2.11 shows the model-predicted τ^A vs. T and P for in-plane wave infill specimens described in Secs. 2.4.1-2.4.3 with fixed O = 0.15 mm. Increasing the T and P yields a monotonic increase and decrease, respectively, in τ^A. However, at high period values (P > 7 mm), the fabrication time remains unaffected by changes in thickness.

Because of the small changes in length of the wave infill due to varying O, the model suggests that a decrease in O slightly increases τ^A. Because the change in τ^A with varying overlap is negligible compared to those due to P and T, these changes are not presented graphically in Figure 2.11. Finally, W has no effect on fabrication time because the amount of material delivered by the nozzle is assumed not to influence the machine dynamics.

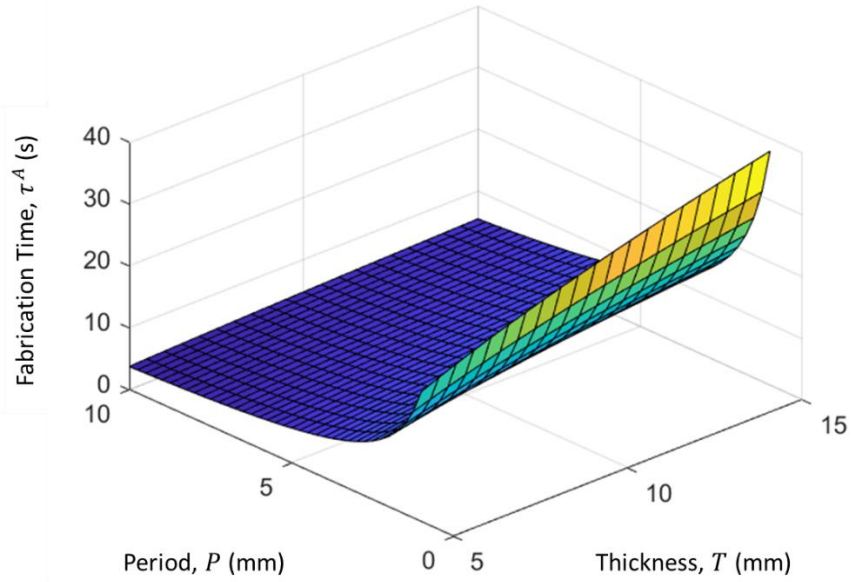

Figure 2.11. Plot of τ^A vs. T and P with O = 0.15 mm with variable ranges of 3 < T < 15 mm and 1 < P < 10 mm for in-plane wave infill specimen fabricated with a maximum machine velocity and acceleration of v_m = 150 mm/s and a_m = 3000 mm/s^2.

2.7.3 Mass

An analysis of specimen mass, M^A, analytical model (Appendix D) suggests that T, P, and W contribute most significantly to M^A. Figure 2.12 shows the model-predicted M^A vs. specimen T and P for W = 0.45 mm and W = 0.95 mm and O = 0.15 mm for in-plane wave infill specimens described in Secs. 2.4.1-2.4.3. As expected, increasing the T and P yields a monotonic increase and decrease, respectively, in M^A. Furthermore, T has a more pronounced effect on M^A at lower wave P (P < 5 mm) and a negligible effect at higher P (P > 5 mm).

As shown by the two surfaces representing specimen mass with W = 0.45 mm and 0.95 mm, W affects M^A. Because of the added material, a larger W increases M^A at all T and P values but has the largest affect at high T (T > 10 mm) and low P (P < 5 mm).

Although wave O is held constant in this analysis, a reduction in O slightly increases specimen mass. This increase is negligible compared with increase in M^A due to T, P, and W and, thus, is not shown graphically.

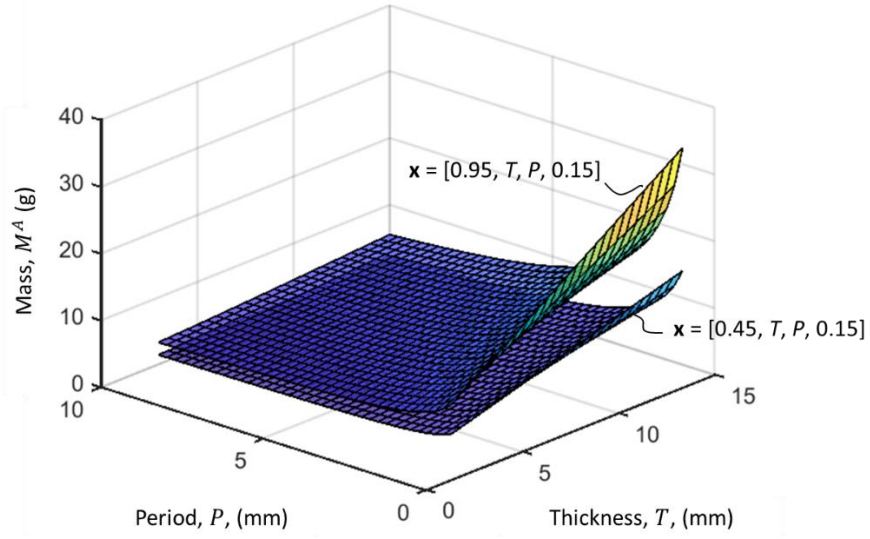

Figure 2.12. Plot of model-predicted specimen M^A vs. thickness, T, P, W = 0.45 mm and 0.95 mm, and a fixed O = 0.15 mm with variable ranges of 3 < T < 15 mm and 1 < P < 10 mm for in-plane wave infill specimens using a material density for the Nylon-12 MEX material of ρ = 1.01 g/cm^2.

2.7.4 Design Guidelines for the Uniform Wave Infill Ankle-Foot Orthosis

The sensitivity analysis of Sec. 2.7 provides design guidelines for the design of uniform geometry AFOs. When designing an AFO with wave infill stacked along the height of the device, the thickness of the beam contributes the most to beam stiffness and strength. However, this increase in thickness yields an increase in fabrication time and mass. Therefore, the thickness of the wave infill beam is used to achieve the desired range of the stiffness or strength of the beam, and the wave infill period is used for fine tuning of that stiffness and strength. Additionally, because the beadwidth does not contribute to the fabrication time, it can be used to increase

stiffness and mass of the device without the added fabrication time cost. Limitations with this model is that it is limited to only considering uniform wave infill geometries. Chapter 3 will develop a technique for applying this sensitivity analysis to small elements that can be assembled to determine the structural properties of the AFO.

2.8 Conclusions

Four analytical models to predict the stiffness, load capacity, fabrication time, and mass of the wave infill four-point bending beam specimen with in-plane and layer-to-layer orientations in MEX were developed and validated with experimental measurements. Stiffness analytical models showed high correlations, R^2 > 98%, and high predictive capabilities, RRMSE < 7%, to estimate the experimental results. Load capacity was more difficult to predict and demonstrates the inconsistency inherent in the layer-by-layer manufacturing processes such as MEX. Load capacity analytical models demonstrated correlations of R^2 > 86% and predictive capabilities of RRMSE < 24% to estimate the experimental results. The analytical model estimations for both fabrication time and mass showed high correlations, R^2 > 97%, and high predictive capabilities, RRMSE < 7%, to estimate the experimental results.

Upon analysis of the analytical model trends, it is evident and expected that the thickness of the wave infill beam contributes most significantly to four metrics: stiffness, load capacity, fabrication time, and mass. Period and beadwidth also contribute to the four metrics. When fabricating MEX TWS, an optimization of the wave infill geometry may design the geometry to a minimum mass or fabrication time.

The future work will focus on developing the optimization algorithms that will minimize the mass or the fabrication time of MEX TWSs subjected to generalized loads while maintaining a desired structural stiffness. Two other areas of future research include improved accuracy of

prediction and understanding of the failure of the wave infilled TWS under bending loads and the wave infill TWS shear stiffness.

Chapter 3
Finite Element Composite Simplification Modeling and Design of the Material Extrusion Wave Infill for Thin-Walled Structure

3.1 Abstract

The finite element composite simplification model (CSM) for modelling the material extrusion (MEX) wave infill of a thin-walled structure (TWS) with generalized geometries and loading conditions is presented. The MEX wave infill is a sine wave infill pattern used to generate a lightweight thin-walled structure (TWS) with desired bending properties. In CSM, the wave infill and TWS faces are modelled as a homogenous stacked composite, which reduces computation and setup time. Analytical models are presented to determine the effective material properties of the homogeneous core of the CSM. Previously reported four-point flexural experiments were used to validate the CSM. CSM was shown to predict the measured experimental stiffness within 15%. Using CSM, fixed flat- and curved-plate cantilevers with uniform and varying wave infill were analyzed. These analyses show CSM to be a powerful finite element tool that can be used in the future to optimize the wave infill for TWSs.

3.2 Introduction

The wave infill for material extrusion (MEX), a layer-by-layer additive manufacturing (AM) process, is a sine wave infill pattern used to generate a lightweight thin-walled structure (TWS) with desired bending properties [3]. A TWS is composed of outer facings and a corrugated core filled by a wave infill. Such TWS parts with wave infill have been widely utilized for lightweight structure [18,19,22,23]. This study investigates the composite simplification model

(CSM) for modelling the bulk material properties of the MEX wave infill in TWSs with generalized geometries and loading conditions.

In this paper, the wave infill geometry, directional material properties, and composite CSM are described in Sec. 3.3. The CSM is validated in Sec. 3.4 by comparing four-point bending experiments to results from a representative finite element CSM. In Secs. 3.5 and 3.6, the process for modelling a fixed flat-cantilever and an AFO, respectively, with CSM for a MEX TWS is described.

3.3 MEX Wave Infill and Composite Simplification Modeling

The MEX wave infill and the CSM for the TWS is presented.

3.3.1 Wave Infill Geometry and Directional Material Properties

A MEX TWS with wave infill is shown in Figure 3.1. This TWS is fabricated using MEX by stacking layers of thermoplastic material in the Z-direction. Each layer is composed of outer facings, which define the outer boundary of the TWS, and the wave infill core. The MEX wave infill can be characterized by the geometry of the inner wave and the interference between the wave and the outer facing. For a straight bar specimen, as shown in Figure 3.2, four variables define the geometry of the wave infill along the toolpath centerline within the outer boundaries of the specimen [3]:

- Beadwidth W: The width of the deposited thermoplastic bead
- Thickness T: The localized thickness of the TWS measured normal to the TWS mid-plane
- Period P: The localized period of one wave of the wave infill pattern
- Overlap, O: The overlap of the wave infill peaks and the outer contour.

As shown in Figure 3.2, *O* is the minimum distance between centerlines of the outer layer and the extremes of the wave. A lower value of *O* reduces the distance between the wave and contour centerlines, corresponding to a greater overlap of the contour and wave.

The amplitude of the wave infill, H, as shown in Figure 3.2, is defined as:

$$H = \frac{T}{2} - \left(\frac{W}{2} + O\right) \tag{3.1}$$

The primary deformation mode of a TWS is bending. In bending, the flexural stiffness of the MEX wave infill TWS varies in the X- and Z- directions because of the wave geometry. The layer-to-layer MEX process itself also generates the transverse orthotropy in the part and affects the directional material properties. Transverse orthotropy refers to the in-plane and layer-to-layer material symmetry directions, as shown in Figure 3.1.

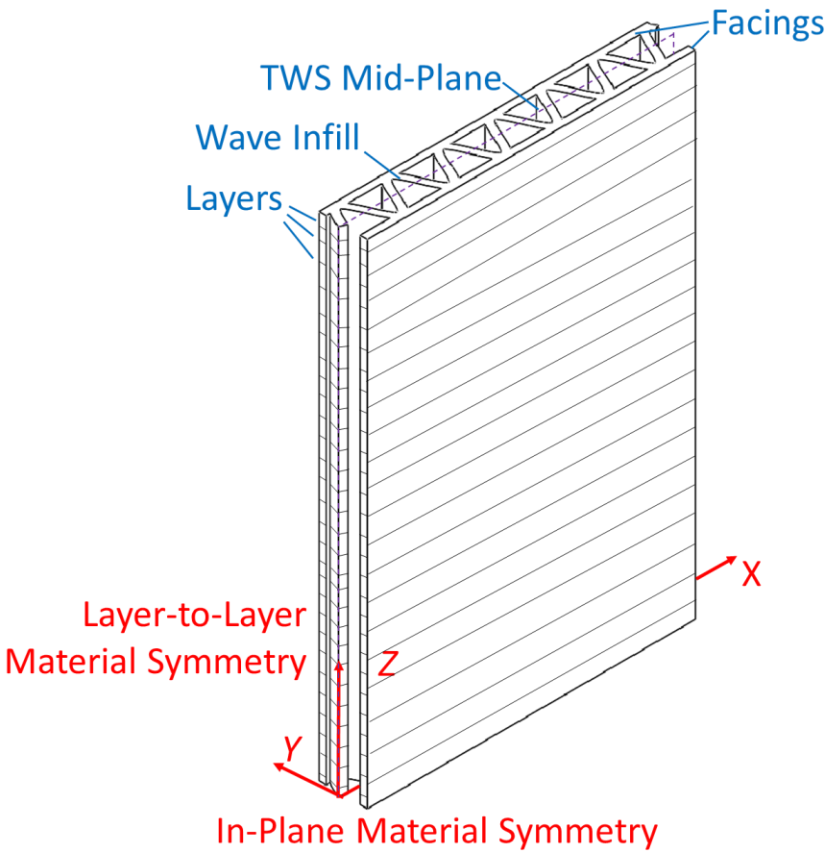

Figure 3.1. MEX wave infill TWS defined along the TWS mid-plane and composed of stacked layers of facings and wave infill core. The part exhibits transverse orthotropy in the in-plane and layer-to-layer material symmetry directions due to the cross-sectional area moment of inertias and directional material properties from the MEX process.

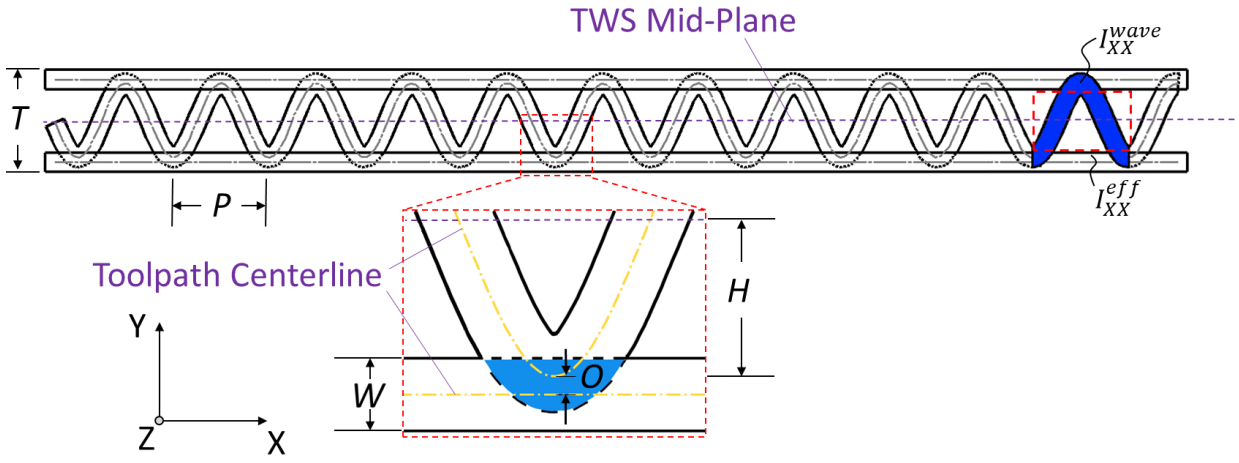

Figure 3.2. Top-view of the MEX wave infill for a straight beam TWS. The geometry of the MEX wave infill is defined along the TWS mid-plane and by the outer thickness of the TWS, the period of the wave, the beadwidth of the toolpath, and the overlap between the wave infill and the facings.

For the structural analysis of the MEX wave infill TWS, the material properties of the base MEX material are required. These material properties include: (1) the in-plane elastic modulus, E_X, which is the slope of the linear portion of the tensile stress-strain curve of the material along the direction of the toolpath centerline, (2) the layer-to-layer elastic modulus, E_Z, which is the slope of the linear portion of the tensile stress-strain curve of the material along the layer direction, and (3) the in-plane Poisson's ratio, ν_{XZ}. These three properties will be used in the CSM of the MEX wave infill.

3.3.2 CSM of a MEX Wave Infill TWS

The CSM is developed to calculate the deformation of a generalized MEX wave infill TWS under loading. The wave infill TWS is modelled as a composite stack composed of homogeneous laminae with properties equivalent to the TWS in CSM. The MEX wave infill TWS (Figure 3.3(a)) with outer thickness, T, wave infill period, P, beadwidth, W, core thickness, T_C ($T_C = T - 2W$), and length, b, is modeled with the composite stack shown in Figure 3.3(b). As shown in the cross-sectional view in Figure 3.3(c), the composite stack has inner and outer facing laminae, which represent the inner and outer facings of the MEX wave infill TWS, and a core lamina with properties equivalent to the wave infill of the TWS.

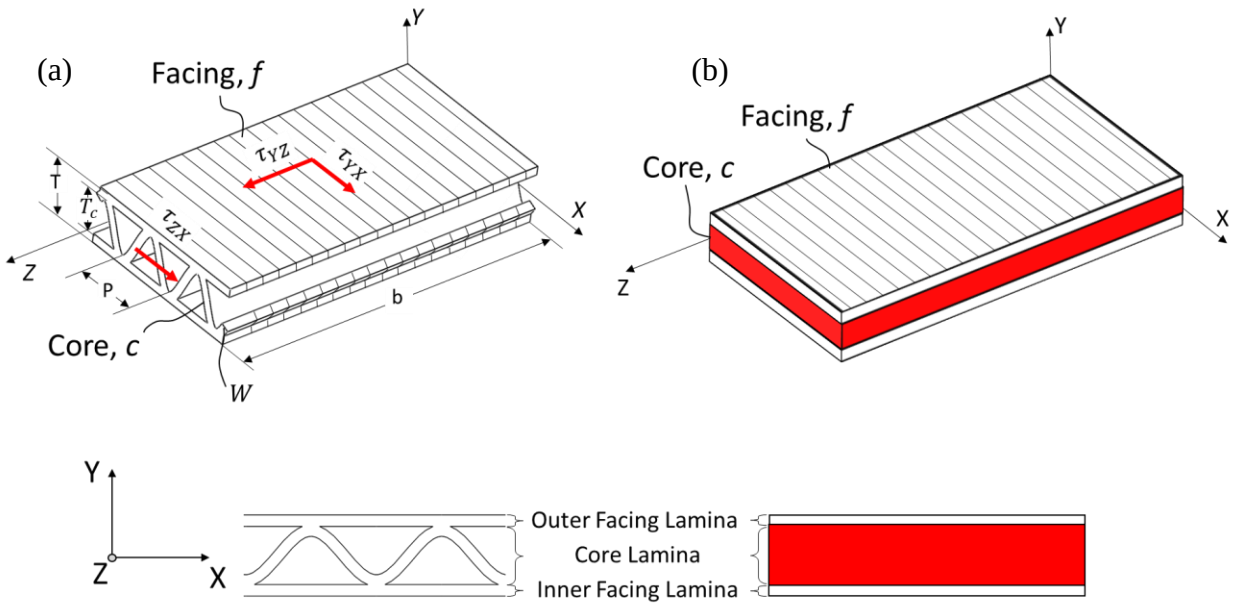

(c)

Figure 3.3. An example MEX wave infill TWS with (a) outer thickness, T, wave infill period, P, beadwidth, W, core thickness, T_C, and length, b. This TWS can be modeled as (b) a composite stack with bending properties equivalent to the MEX wave infill TWS and with inner and outer facing laminae and the inner core lamina, which represents the wave infill. In (c), the lamina representing each structure of the MEX wave infill is shown.

To equate the MEX wave infill TWS to the CSM, each lamina of the composite must be assigned the appropriate material properties. Assuming a transversely orthotropic lamina (with equivalent X- and Y-directional properties), the constitutive equation for a lamina with respect to the primary axes (i.e. X, Y, Z) is:

$$\begin{bmatrix} \varepsilon_{XX} \\ \varepsilon_{YY} \\ \varepsilon_{ZZ} \\ \varepsilon_{YZ} \\ \varepsilon_{ZX} \\ \varepsilon_{XY} \end{bmatrix} = \begin{bmatrix} \frac{1}{E_X} & -\frac{\nu_{YX}}{E_Y} & -\frac{\nu_{ZX}}{E_Z} & 0 & 0 & 0 \\ -\frac{\nu_{XY}}{E_X} & \frac{1}{E_Y} & -\frac{\nu_{ZY}}{E_Z} & 0 & 0 & 0 \\ -\frac{\nu_{XZ}}{E_X} & -\frac{\nu_{YZ}}{E_Y} & \frac{1}{E_Z} & 0 & 0 & 0 \\ 0 & 0 & 0 & \frac{1}{2G_{YZ}} & 0 & 0 \\ 0 & 0 & 0 & 0 & \frac{1}{2G_{ZX}} & 0 \\ 0 & 0 & 0 & 0 & 0 & \frac{1}{2G_{YX}} \end{bmatrix} \begin{bmatrix} \sigma_{XX} \\ \sigma_{YY} \\ \sigma_{ZZ} \\ \sigma_{YZ} \\ \sigma_{ZX} \\ \sigma_{XY} \end{bmatrix} \tag{3.2}$$

or

$$[\varepsilon_i] = [S_{ij}][\sigma_i] \tag{3.3}$$

where ε_i is the directional lamina strain, σ_i is the directional lamina stress, and S_{ij} is the compliance tensor of the material with E_i, the lamina's i^{th}-direction modulus of elasticity, ν_{ij}, the ij^{th}-direction Poisson's ratio, and G_{ij}, the ij^{th}-direction shear modulus. Because of the transverse isotropy (i.e. equivalent X- and Y- directional properties) and the symmetry of S_{ij} (e.g. $\frac{\nu_{XZ}}{E_X} = \frac{\nu_{ZX}}{E_Z}$), 8 material properties are needed to fully characterize S_{ij}: $E_X,\ E_Z,\ G_{YX},\ G_{YZ},\ G_{ZX},\ \nu_{XY}, \nu_{YZ}, \nu_{XZ}$. However, because the primary deformation of a TWS is a bending mode, the TWS experiences negligible loading in the Y-direction and properties ν_{XY} and ν_{YZ} are unimportant to TWS analyses. Therefore, only 6 material properties, $E_X, E_Z, G_{YX}, G_{YZ}, G_{ZX}$, and ν_{XZ}, are required.

For the CSM of the MEX wave infill TWS, each lamina has a unique material compliance tensor. For the CSM of the inner and outer MEX wave infill facings, the compliance tensor and its components are referred to with the superscript 'f' (e.g. S_{ij}^f and E_X^f). The material properties of the core lamina in the CSM are referred to with the superscript 'c' (e.g. S_{ij}^c and E_X^c). In this study, the inner and outer facings of the MEX wave infill TWS and the CSM are assumed to have properties equivalent to the base material. Analytical models are used to describe the effective core lamina properties for the CSM in terms of base material properties and the wave infill geometry.

3.3.3 Analytical Models for the Effective Core Lamina Properties

Analytical models for defining some of the effective core lamina properties ($E_X^c,\ G_{YX}^c$, and G_{YZ}^c) have been described for the study of paper corrugations [30,63]. These analytical models have been adapted and derived here to express equivalent lamina material properties of the MEX wave infill core.

3.3.4 Effective Core Elastic Moduli, $\mathbf{E_Z^c}$ and $\mathbf{E_X^c}$

Analytical expressions for the effective core elastic moduli, E_Z^c and E_X^c, relate the elastic stresses and strains of the core. The effective core in-plane elastic modulus, E_X^c of the wave infill is determined by considering the YZ cross-section of the wave infill. Because the distance from the neutral axis to the wave infill varies in the TWS, the in-plane effective elastic modulus of the core lamina, E_X^c, is assumed to be negligible:

$$E_X^c \approx 0 \tag{3.4}$$

The effective core layer-to-layer effective elastic modulus, E_Z^c, is determined by considering the XY- cross-section of the wave infill. Other works [63] have defined E_Z^c as a ratio between the area of the infill and the effective area of the core. However, because the primary deformation of the TWS is a bending mode, a more appropriate calculation of E_Z^c is:

$$E_Z^c = \alpha \frac{I_{XX}^w}{I_{XX}^{eff}} E_Z \tag{3.5}$$

where α is a correction factor, I_{XX}^w is the area moment of inertia of the wave infill given in [3], and I_{XX}^{eff} is the effective area moment of inertia of the core (both regions shown in Figure 3.2) given by:

$$I_{XX}^{eff} = \frac{1}{12} T_C^3 \, P \tag{3.6}$$

The ratio of Eq. (3.5) considers the material distribution of the wave infill about the neutral axis of the TWS in the bending mode. However, as seen in Figure 3.2, the wave infill overlaps into the inner and outer facings (i.e. beyond the core thickness, T_C), which will provide an overprediction of E_Z^c. To account for this overprediction, a correction factor, α, is applied. In this study, a 20% correction factor of α = 0.8 was used.

3.3.5 Effective Core Shear Moduli G^C_{ZX}, G^C_{YX}, and G^C_{YZ}

The effective shear moduli of the core, G^C_{ZX}, G^C_{YX}, and G^C_{YZ}, relate the shear deformation of the MEX wave infill TWS subjected to applied shear stresses τ_{ZX}, τ_{YX}, and τ_{YZ}, as shown in Figure 3.3. Assuming the analyzed wave infill geometries are symmetrical and uniform throughout the TWS and the deformation is in pure bending (i.e. no twisting), the in-plane effective core shear modulus, G^C_{ZX}, can be assumed to be negligible [63]:

$$G^C_{ZX} \approx 0 \tag{3.7}$$

If these conditions are not true, such as when the wave infill is not symmetrical throughout the part or the loading conditions transmit a shear along the ZX-surface, this assumption needs to be revisited.

Appendix A presents details of the derivation of the analytical model expression for calculating an effective core shear modulus, G^C_{YZ}:

$$G^C_{YZ} = \frac{4\,T_C\,W}{P\,L_w} G_{XZ} \tag{3.8}$$

where G_{XZ} is the base material in-plane shear modulus according to Eq. (F.5) and L_w is the arclength of the sine wave from Eq. (F.3).

Appendix B presents details of the derivation of the analytical model expression for calculating an effective core shear modulus, G^C_{YX}:

$$G^C_{XY} = E_X\,A_X \left(\frac{T_c}{\frac{P}{2}\,b}\right) \frac{\det\begin{bmatrix} C_{11} & C_{12} \\ C_{12} & C_{22} \end{bmatrix}}{\det\begin{bmatrix} C_{11} & C_{12} & C_{13} \\ C_{12} & C_{22} & C_{23} \\ C_{13} & C_{23} & C_{33} \end{bmatrix}} \tag{3.9}$$

where E_X is the base material in-plane elastic modulus, $A_X \approx b\,W$, and C_{ij} are coefficient of the wave infill core compliance matrix given by Eqs. (B.20)-(B.25).

3.4 Validation of CSM for MEX Wave Infill with Four-Point Bending Experiments Discussion

In this section, a CSM is generated for MEX wave infill bending experiments previously reported in [3]. FEM is applied to simulate the bending experiments using the CSM to validate the technique.

3.4.1 Bending Experiments of MEX Wave Infill Specimens [3]

The ASTM Standard D790-10 four-point flexural bending tests were performed on both in-plane and layer-to-layer rectangular prism Nylon-12 MEX specimens with varying wave infills [3]. As shown in Figure 3.4, specimen length, l, was 120 mm and thickness, T, was variable. Width, b, of the in-plane and layer-to-layer specimens were 10 mm and 40 mm, respectively. Loading pins were spaced with a distance, a, of 30 mm, and support pins were spaced with a distance, L_s, of 80 mm. Each pin had a radius of 5 mm. During the four-point flexural tests, load, F_b, on the pin and their displacement, δ, were measured. The resulting in-plane stiffness, K_X^E, and layer-to-layer stiffness, K_Z^E, specimens were determined using a linear fit of the F_b vs δ data.

Table 3.1 shows the experimental variables and the measured flexural stiffnesses, K_X^E and K_Z^E, for both the in-plane and layer-to-layer geometries, respectively. Because specimens undergoing four-point flexure tests experience both shear and elastic deformation and stresses, these experiments will be used to validate the CSM for use in generalized structures.

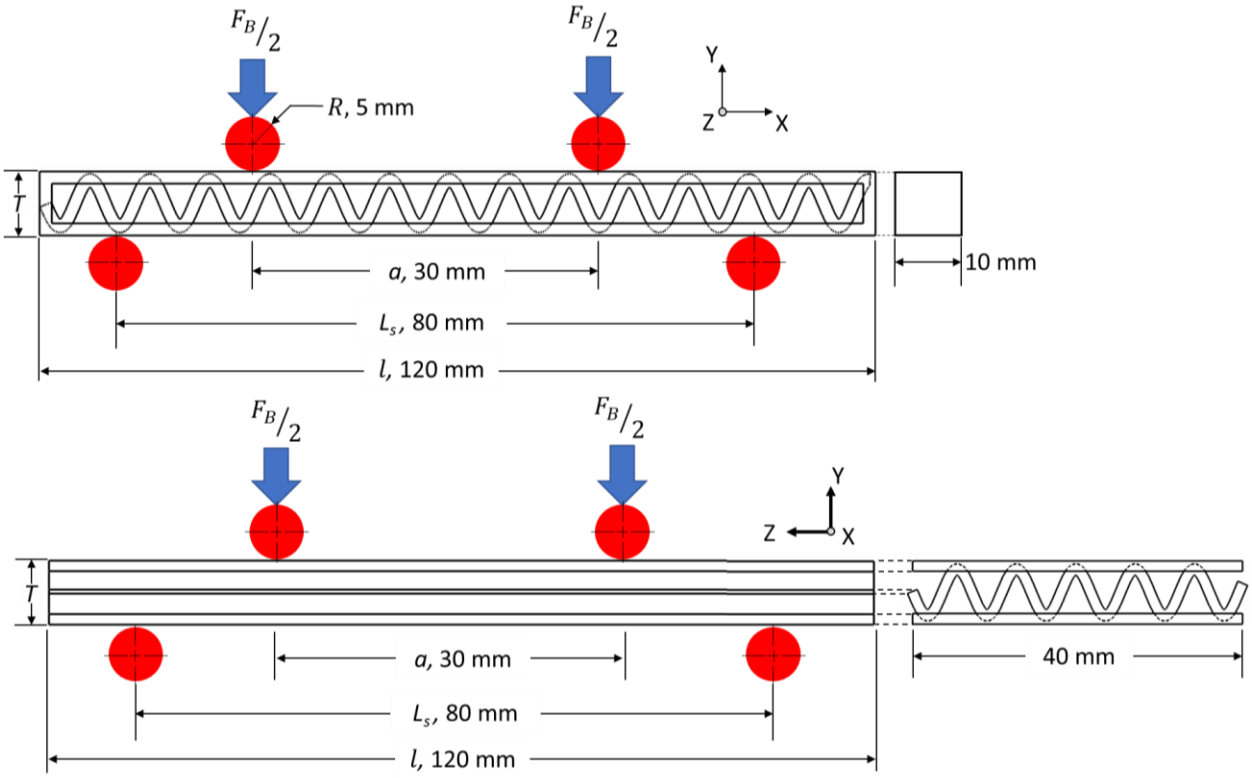

Figure 3.4. Four-point bending test setup schematic for (a) in-plane and (b) layer-to-layer specimens. Reproduced with permission from [3].

Table 3.1. Wave infill geometry variables and experimental [3] and CSM flexural stiffness values for in-plane and layer-to-layer specimens.

Experimental Variables (mm)					Stiffness, K (N/mm)					
					In-Plane			Layer-to-Layer		
No.	W	T	P	O	Experiment K_X^E	CSM K_X^C	Error ϵ_R	Experiment K_Z^E	CSM K_Z^C	Error ϵ_R
1	0.80	8.79	2.00	0.22	47.3	45.3	4%	274.5	281.9	-3%
2	0.47	5.07	1.46	0.13	8.9	9.7	-9%	50.4	55.0	-9%
3	0.53	10.39	1.34	0.18	48.9	32.1	34%	380.0	420.7	-11%
4	0.81	7.84	2.66	0.10	37.9	36.5	4%	176.0	193.9	-10%
5	0.89	5.86	2.78	0.28	20.3	22.3	-10%	82.3	95.9	-17%
6	0.73	3.35	3.17	0.12	4.7	5.2	-11%	20.3	22.1	-9%
7	0.87	5.30	10.00	0.32	15.3	16.0	-4%	54.4	71.1	-31%

3.4.2 CSM of Bending TWS

To validate the CSM for wave infill geometries, a FEM of the four-point bending tests in Sec. 3.4.1 was performed. Both the in-plane (Figure 3.5) and layer-to-layer (Figure 3.6) four-point bending specimen geometries were modelled with quarter symmetry (symmetry in the YZ- and XY- planes) in FEM to match the dimensions of the experimental bending specimen in Figure 3.4. The quarter symmetry specimens were modelled as a 3-ply composite shell with ply orientations set according to the local coordinate system (1,2, n) shown in Figure 3.5 and Figure 3.6. The thickness of the plies was set (according to Figure 3.3) with an outer lamina thickness of W and an inner lamina thickness of T_C. Loading and support pins with the same radius of 5 mm were modelled as rigid shells and were used for applying the four-point flexural load and support, as shown in Figure 3.5 and Figure 3.6. Material properties for the inner and outer lamina were the base material properties of the Nylon-12 thermoplastic. The effective core material properties were determined according to the analytical models of Sec. 3.3. The mesh used in the FEM is shown in Figure 3.5 and Figure 3.6. The 3-ply composite shell were meshed using 4-node general-purpose

shell element (S4R in Abaqus) with a length of 1 mm. The support and loading pins were meshed into 4-node three-dimensional rigid elements (R3D4) with 30 swept elements along the outer diameter of the pins.

Contact properties between the loading and support pins and the part were characterized by normal contact and a tangential-behavior interaction with a frictional coefficient, μ, of 0.15. Boundary conditions applied to the center of the support and loading pins were encastre and a Y-direction deformation of U_Y = –4 mm, respectively. Symmetry boundary conditions for the YZ- and XY- planes were $U_X = R_Y = R_Z = 0$ and $U_Z = R_X = R_Y = 0$, respectively, where U_X and U_Z are linear deformations in the X- and Z- directions, respectively, and R_X, R_Y, and R_Z are rotational deformations about the X-, Y-, and Z-axes, respectively. Reaction forces and deformation were measured at the reference point on the loading pin. After simulation, stiffness, K, of the quarter-symmetry specimen was quantified by determining the linear slope of deformation-force curve.

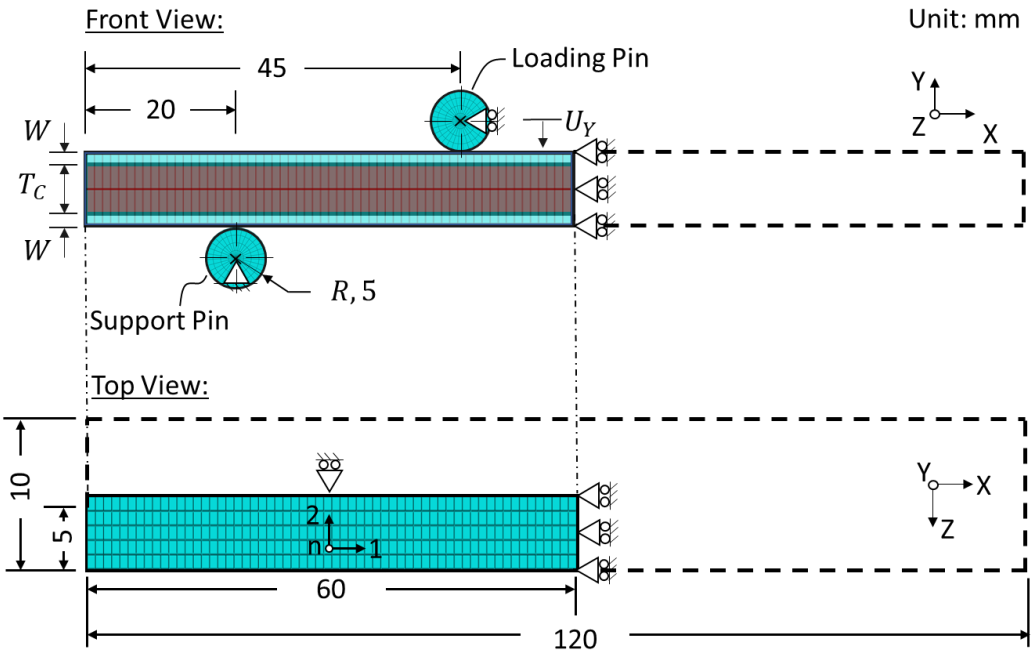

Figure 3.5. In-plane quarter symmetry CSM for the four-point flexural loading of wave infill specimens

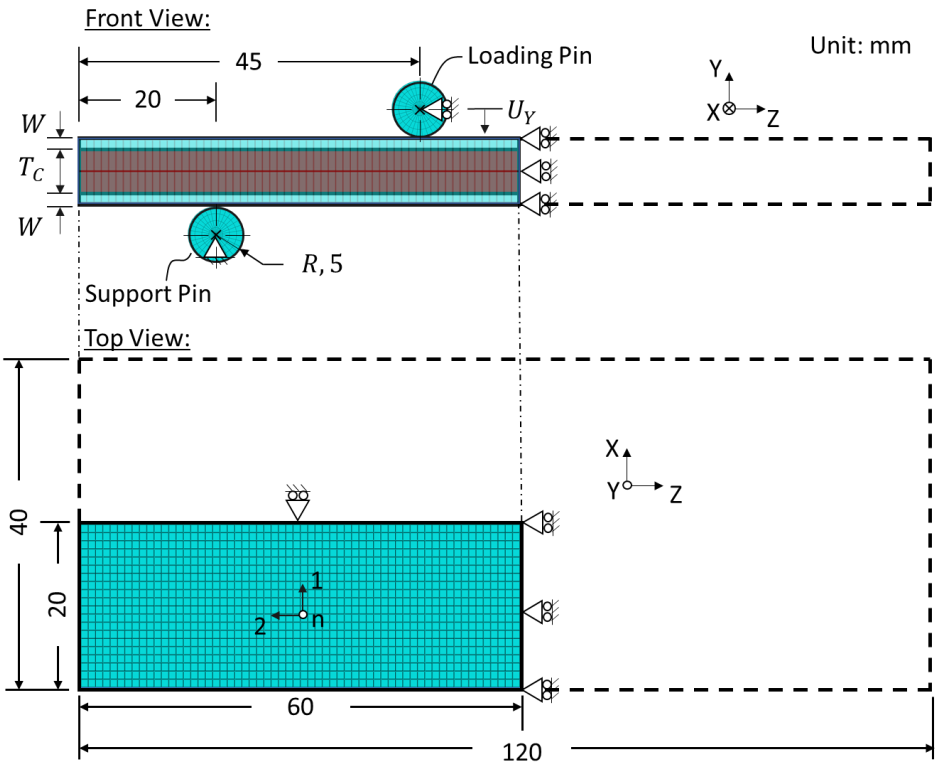

Figure 3.6. Layer-to-layer quarter symmetry CSM for the four-point flexural loading of wave infill specimens

3.4.3 Comparison of FEM of CSM to MEX Wave Infill Bending Experiments

The flexural stiffness determined by the CSM method, K_X^C, for each flexural specimen in both the in-plane and layer-to-layer orientation was calculated according to Sec. 3.4.2 and reported in Table 3.1. The base and effective material properties for Nylon-12 as input into the CSM are shown in Table 3.2 [62,64] and Table 3.3, respectively. Because E_X^C and G_{XZ}^C are negligible according to Eqs. (4) and (7), very small values (E_X^C = 20 MPa and G_{XZ}^C = 10 MPa) compared to the effective core properties of Table 3.3 were input into the CSM to allow the simulation to solve without errors.

As shown in Table 3.1, the in-plane and layer-to-layer numerical results matched well. Among 7 in-plane specimens, all errors are below 11% except Experiment 3, which had the worst numerical performance with an underestimation error ϵ_R = 34%. Experiment 3 has the highest thickness of the group and a low period wave infill. The higher experimental stiffness is due to the

low period wave infill. Through the center of this specimen, the material bridges between successive waves, which contributes to the experimental stiffness, but is not accounted for in the CSM effective in-plane core modulus E_X^C. Additionally, because of the high thickness of the part, this bridging occurs far from the neutral axis increasing the estimation error. The average error for the in-plane specimens is 10%.

For the layer-to-layer specimens, as shown in Table 3.1, all errors were below 10% except Experiments 5 and 7. Experiment 5 had an overestimation error of ϵ_R = 17%. Experiment 7 had the worst numerical performance with an overestimation error ϵ_R = 31%. Experiment 5 and 7 both have large overlap, which likely leads to an underprediction of the area moment of inertia ratio of Eq. (3.5). Experiment 7 has the highest period of each of the experiments. The high period likely causes overestimation errors in the analytical estimation of G_{YZ}^C and E_Z^C. The average error for the layer-to-layer specimens was 12%.

A sensitivity analysis was performed to determine the effect of each property on the overall material stiffness. Each core property was varied for both the in-plane and layer-to-layer directions to determine the corresponding change in stiffnesses of the experiments. For the in-plane specimens, E_X^C and G_{YX}^C contributed most significantly to the stiffness and G_{YZ}^C and E_Z^C had no effect because the in-plane bending loads only generate normal and shear deformations along the X-direction. For the layer-to-layer specimens, E_Z^C and G_{YZ}^C contributed most significantly to the stiffness and G_{YX}^C and E_X^C had no effect because the layer-to-layer bending loads only generate normal and shear deformations along the Z-direction. ν_{XZ} and ν_{ZX} had little effect because of the relatively small deformations and high Poisson ratio of the material. Mesh size also was found to have little effect on the stiffness.

Table 3.2. Base material properties of Nylon-12 material

E_X (MPa)	E_Z (MPa)	G_{ZX} (MPa)	ν_{ZX}
1276	1138	800	0.3

Table 3.3. Effective material properties of the wave infill core for wave infill bending experiments reported in [3].

No.	Core Properties		
	E_Z^C (MPa)	G_{YX}^C (MPa)	G_{YZ}^C (MPa)
1	970.8	29.9	600.2
2	788.1	28.7	478.8
3	921.2	7.8	618.4
4	784.2	33.2	430.6
5	842.8	108.9	442.9
6	820.9	178.0	235.2
7	359.5	29.6	76.7

3.5 Finite Element CSM for a Lightweight Cantilevered TWS with MEX Wave Infill

The CSM is applied to a lightweight cantilevered TWS with uniform and non-uniform wave infill to demonstrate the design of the TWS with MEX wave infill.

3.5.1 Finite Element CSM Setup for a Lightweight Cantilevered TWS with Wave Infill

In this analysis, a fixed cantilever TWS (Figure 3.7) with wave infill and a distributed transverse edge load is analyzed using the finite element CSM. The TWS has a width w_c and a height h_c. Three cases of the wave infill are analyzed: (1) uniform wave infill, (2) non-uniform wave infill varied in the Z-direction, and (3) outer contour and wave beadwidth variation with uniform wave infill. For all cases, the cantilevered beam was modeled as a 3-ply composite shell with ply orientations set according to the local coordinate system (1,2, n) shown in Figure 3.7. For Cases (1) and (2), the composite had an outer lamina thickness W and inner lamina thickness T_C as shown in the top view of Figure 3.7. For Case (3), the modeled structure had an outer facing and wave infill beadwidth, W_f, and W_c, respectively, as shown in Figure 3.7(c). A 3-ply composite shell was meshed using 4-node general-purpose shell element (S4R in Abaqus) and dimensions of 20 mm x 4 mm.

For Case 1 with the uniform wave infill (Figure 3.7(a)), a composite shell structure with uniform properties throughout the part was generated. Structures with uniform values of period P were analyzed according to Table 3.4. The effective material properties for the core lamina structure for each period is shown in Table 3.4. Infill densities above 95% and below 45% lead to overfilling and underfilling, respectively, of the specimen. Therefore, as shown in Figure 3.8, the allowable design range for this beam setup was with a period between 1.125 and 3 mm. Material properties for the outer lamina are shown in Table 3.2. For Case 2 with the non-uniform wave infill (Figure 3.7(b)), a composite shell structure was used but was discretized into sections along the Z-direction. Sections had a height of dz (dz = 20 mm with 5 layers of elements) and the width of the beam w. For each of the sections, the wave infill effective core material properties according to Sec. 3.3.3 were applied to each Z-direction section of the TWS (Table 3.6). For Case (3), a composite shell structure with uniform properties throughout the part was generated. Structures with uniform values of period P were analyzed according to Table 3.5. The effective material properties for the core lamina structure for each period is shown in Table 3.5. For Cases (1) and (2), each cantilever had a beadwidth, W, thickness, T, and overlap, O of 0.5, 7.0, and 0.1 mm, respectively. For Case (3), the cantilever had an outer facing beadwidth, W_f, and inner core beadwidth, W_c, thickness, T, and overlap, O, of 1.0, 0.5, 7.0, and 0.1 mm, respectively. An isometric view of the cantilever beam with wave infill is shown in Figure 3.7(d).

The cantilever TWSs of each case was loaded with a distributed edge load of magnitude ψ per unit length. The load was applied about the TWS X-axis such that the MEX layers were subject to the bending load. Encastre boundary conditions at the base edge of the cantilever were applied. The beam stiffness, K was determined by:

$$K = \frac{\psi}{\delta} \tag{3.10}$$

where δ is the maximum deflection at the top of the cantilever. The mass of the beam and density of the infill was calculated using analytical models developed in [3].

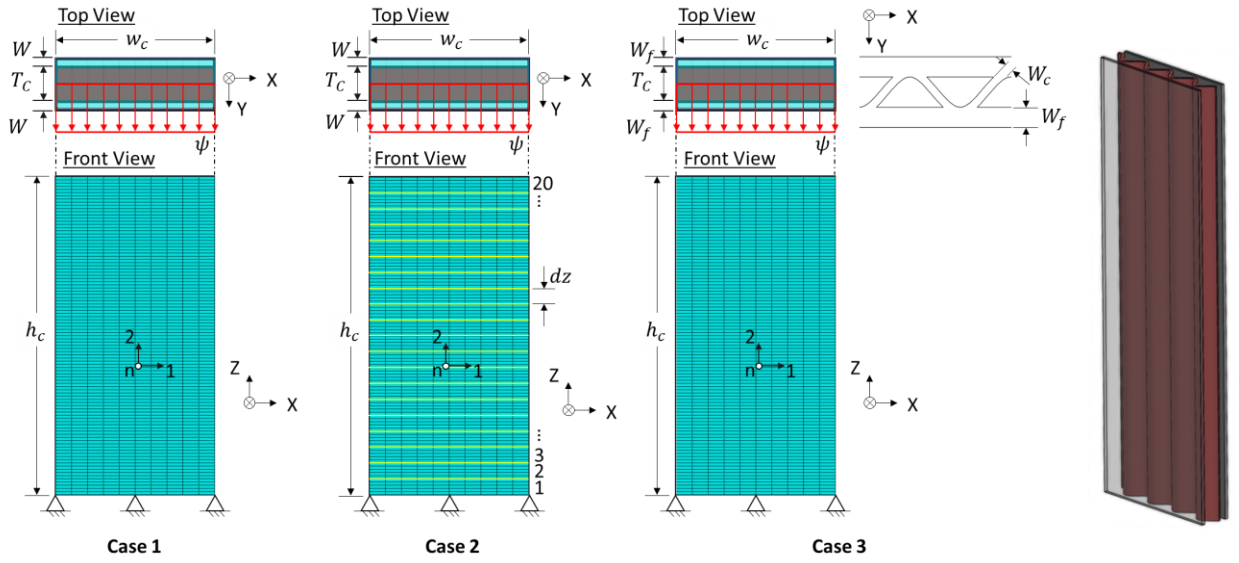

Figure 3.7. Fixed cantilever TWS for finite element CSM of (a) uniform wave infill, (b) non-uniform wave infill varied in Z-direction, and (c) uniform wave infill with differing beadwidths for the core, W_c, and facing W_f. Yellow lines represent sections across which the wave infill in varied. (d) Isometric view of an example cantilever beam with uniform wave infill.

Table 3.4. Cantilever MEX TWSs with uniform wave infill period were analyzed. Effective core properties, E_Z^c, G_{YX}^c, and G_{YZ}^c were found for periods between 1.125 and 3.000 mm and varying core thickness, T_c. Stiffness, K, mass, M, and infill density were calculated for each analyzed cantilever. Beadwidth, W, and overlap, O were 0.5, 7.0, and 0.1 mm, respectively. Example effective core properties for the flat plate cantilever with T_c of 7 mm are shown here.

P (mm)	E_Z^c (MPa)	G_{YX}^c (MPa)	G_{YZ}^c (MPa)	K (N/mm)	M (grams)	Infill Density (%)
1.125	706.1	16.6	505.5	0.566	494.4	94.9
1.25	590.6	16.0	454.3	0.370	452.7	87.0
1.5	433.6	15.0	377.2	0.244	390.2	75.1
1.75	332.9	14.1	322.1	0.198	345.7	66.6
2	263.9	13.1	280.6	0.174	312.6	60.2
3	128.3	10.0	183.1	0.138	235.7	45.6

Table 3.5. Cantilever MEX TWSs with uniform wave infill period were analyzed. Effective core properties, E_Z^c, G_{YX}^c, and G_{YZ}^c were found for periods between 1.05 and 2.6 mm. Stiffness, K, mass, M, and infill density were calculated for each cantilever. For each beam, thickness, T and overlap, O, were 7.0, and 0.1 mm, respectively. For constant beadwidth beams, beadwidth W was 0.5 mm. For differing beadwidth beams, facing beadwidth, W_f, and core beadwidth, W_c, were 1.0, 0.5, mm, respectively.

	P (mm)	E_Z^c (MPa)	G_{YX}^c (MPa)	G_{YZ}^c (MPa)	K (N/mm)	M (grams)
Constant Beadwidth, W	1.05	794.5	16.98	542.1	0.47	524.2
	1.25	590.6	16.02	454.3	0.19	452.7
	1.45	459.3	15.21	390.5	0.13	401.0
	1.65	368.4	14.44	342.1	0.11	362.1
	1.75	332.9	14.09	322.1	0.10	345.8
	2.25	214.5	12.31	248.2	0.08	286.7
	2.6	165.8	11.20	213.2	0.08	259.0
W_c and W_f Beadwidth	1.05	794.5	16.98	451.8	0.4	503.2
	1.25	590.6	16.02	378.6	0.2	448.4
	1.45	459.3	15.21	325.4	0.1	408.8
	1.65	368.4	14.44	285.1	0.1	378.9
	1.75	332.9	14.09	268.4	0.1	366.4
	2.25	214.5	12.31	206.8	0.1	321.1
	2.6	165.8	11.20	177.7	0.1	299.9

Table 3.6. Cantilever MEX TWSs with linearly varying wave infill period through the Z-direction were analyzed. Effective core properties, E_Z^c, G_{YX}^c, and G_{YZ}^c were found for periods between 1.125- and 3.000-mm. Stiffness, K, mass, M, and infill density were calculated for each analyzed cantilever. Beadwidth, W, thickness, T, and overlap, O were 0.5, 7, and 0.1 mm, respectively.

Section	P (mm)	E_Z^c (MPa)	G_{YX}^c (MPa)	G_{YZ}^c (MPa)
1	1.125	706.1	16.6	505.5
2	1.224	612.2	16.1	464.2
3	1.322	536.9	15.8	429.0
4	1.421	475.3	15.3	398.6
5	1.520	424.1	14.9	372.2
6	1.618	380.9	14.5	349.0
7	1.717	344.0	14.2	328.4
8	1.816	312.3	13.8	310.0
9	1.914	284.9	13.4	293.6
10	2.013	260.9	13.1	278.7
11	2.112	239.9	12.7	265.2
12	2.211	221.3	12.4	252.8
13	2.309	204.8	12.1	241.6
14	2.408	190.1	11.8	231.2
15	2.507	177.0	11.5	221.6
16	2.605	165.2	11.2	212.8
17	2.704	154.5	10.9	204.6
18	2.803	144.9	10.6	196.9
19	2.901	136.2	10.3	189.8
20	3.000	128.3	10.0	183.1

3.5.2 Results from Finite Element CSM of a Cantilevered TWS with Wave Infill

With the finite element CSM described in Sec. 3.5.1, cantilever beams with the period and effective core material properties shown in Table 3.4 were analyzed. The stiffness, mass, and infill density for each cantilever was calculated for each beam and shown in Table 3.4. Within this design range, a plot of the stiffness-to-mass ratio (i.e. stiffness, K and mass, M) of the cantilever beam versus period is shown in Figure 3.9. For both mass and stiffness, the trend is a rapid decline between P of 1 and 3 mm. Increasing the core thickness offsets each curve to a higher stiffness-to-mass ratio. Increasing the period reduces the stiffness-to-mass ratio of the beam. A minimum in the stiffness-to-mass ratio for core thickness can be seen at $P \approx 2.0$ mm.

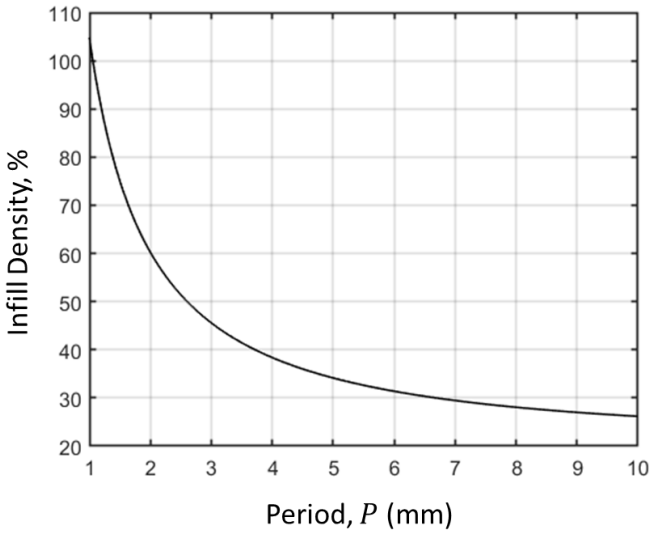

Figure 3.8. Infill density versus period for cantilever beam with thickness of 7.0 mm.

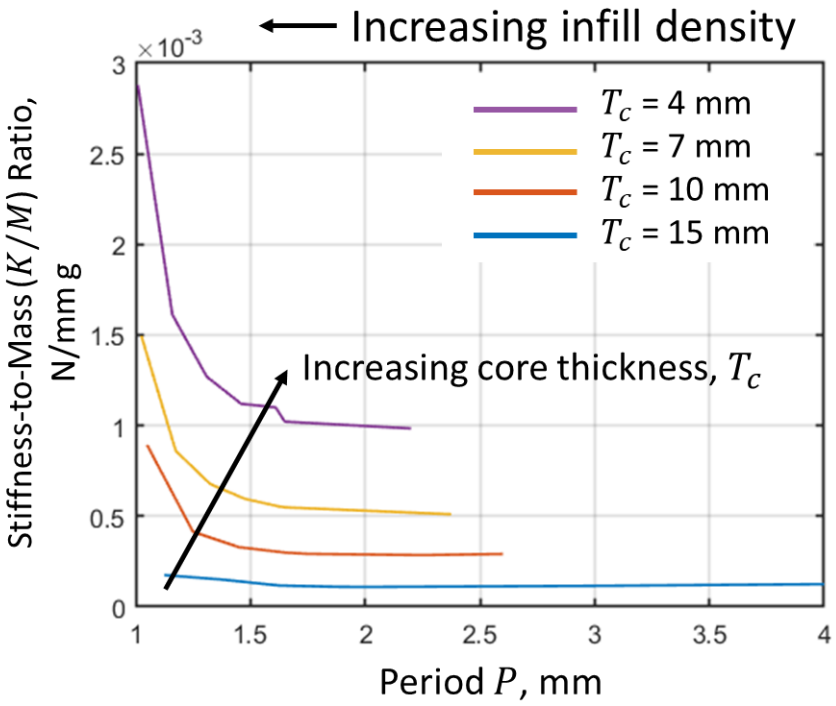

Figure 3.9. Stiffness-to-mass ratio of uniform wave infill cantilever TWS beams with varying core thickness, T_c, and varying period.

With the finite element CSM described in Sec. 3.5.1, cantilever beams with the period and effective core material properties shown in Table 3.5 were analyzed. The stiffness and mass for each cantilever was calculated for each beam and shown in Table 3.5. Within this design range, a plot of the stiffness-to-mass ratio (i.e. stiffness, K and mass, M) of the cantilever beam versus period is shown in Figure 3.10. At high periods, cantilever beams with differing beadwidths are shown to have higher stiffness-to-mass ratios. This result indicates that the core geometry contributes negligibly to the cantilever stiffness. Therefore, its thickness can be reduced to improve the stiffness-to-mass ratio of wave infill beams.

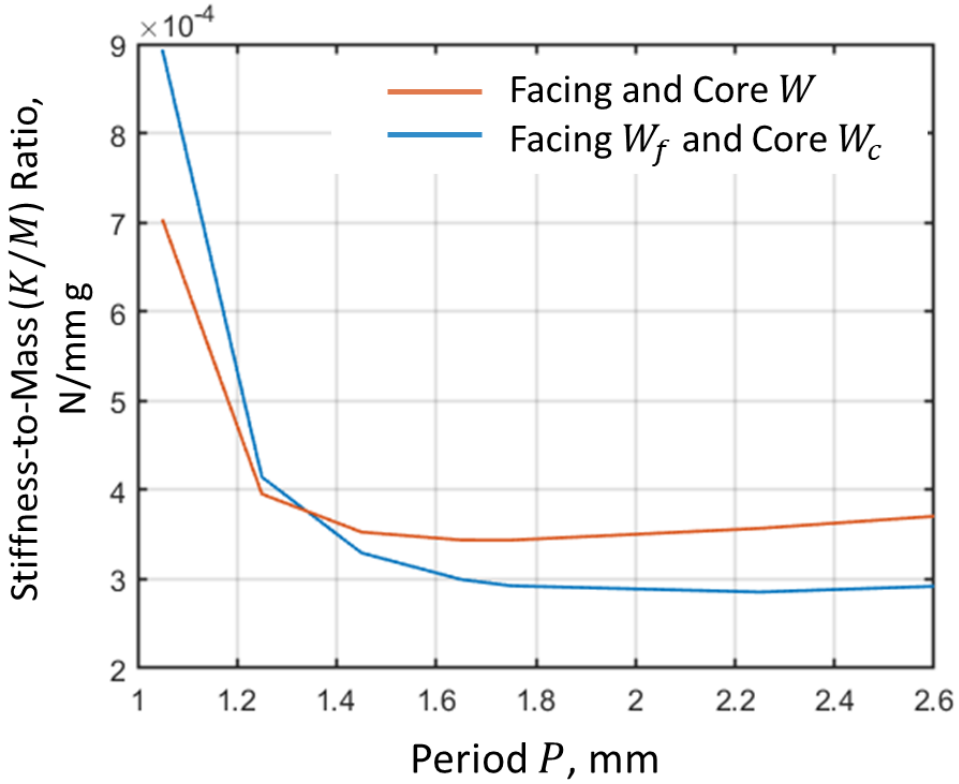

Figure 3.10.Comparison of stiffness-to-mass ratio versus period, P, for fixed flat plate cantilevers with constant beadwidth W and differing core, W_c, and facing, W_f, beadwidths.

With the finite element CSM described in Sec. 3.5.1, a cantilever beam with a linearly varying period and effective core material properties shown in Table 3.6 were analyzed. The stiffness and mass of the cantilever beam were calculated to be 0.25 N/mm and 325.7 g, respectively.

3.6 Finite Element CSM for a MEX Wave Infill AFO

The CSM is applied to a TWS AFO with uniform wave infill to demonstrate the application potential of CSM.

3.6.1 Finite Element CSM Setup for an AFO TWS with Wave Infill

In this analysis, the bending stiffness of a TWS AFO (Figure 3.11) with wave infill was determined. The AFO bending stiffness is determined in the literature [1] using:

$$S = \frac{F\ h_F}{\theta} \tag{3.11}$$

where F is the load applied at the vertical height h_F, which is the region that supports the leg during AFO use, and θ, which is the deformation angle about the ankle axis that occurs during loading. θ is:

$$\theta = \text{atan}\left(\frac{\delta}{h}\right) \tag{3.12}$$

AFO bending stiffnesses range between 1-8 N-m/°. A solid-filled MEX AFO with the same geometry and material as the one analyzed in this study was found to have a stiffness of 3.8 N-m/° (Sec. 1.2). Using the same loading conditions, CSM was applied to the AFO to determine its stiffness. The AFO was fixed at its base and was subjected to a transverse bending load. The deflection under loading was determined using finite element. The loading height, h_F, in which force F was applied was 250 mm and distance from maximum deflection to the ankle axis was 350 mm. Two wave infill periods were tested while keeping other variables constant. A period, P = 1.15 mm, which yields an infill density of 98%, was used to simulate a solid-filled MEX AFO, like the one experimentally tested in Sec. 1.2. P = 3 mm was used as another example to estimate the stiffness of a low-density wave infill AFO.

All elements above the ankle axis were modeled as a 3-ply composite shell with ply orientations set according to the local coordinate system shown in Figure 3.11. The composite had an outer lamina thickness W and inner lamina thickness T_C. The 3-ply composite shell was meshed with the original STL file mesh, which are 3-node general-purpose shell element (S4R in Abaqus).

The AFO had wave infill properties above the ankle axis. Below the ankle axis, the material was modeled with solid material with isotropic material properties because this region was expected to contribute negligibly to ankle stiffness. Structures with two uniform values of period

P were analyzed according to Table 3.7. The effective material properties for the core lamina structure for each period is shown in Table 3.7. Material properties for the outer lamina are shown in Table 3.2. The AFO had a beadwidth, W, thickness, T, and overlap, O of 0.5, 4.0, and 0.1 mm, respectively.

The AFO TWS was loaded on its rear surface at height h_F with a concentrated load of 1N in the X-direction. The load was applied about the TWS X-axis such that the MEX layers were subject to the bending load. Encastre boundary condition at the base of the foot that modeled loading conditions during gait were applied.

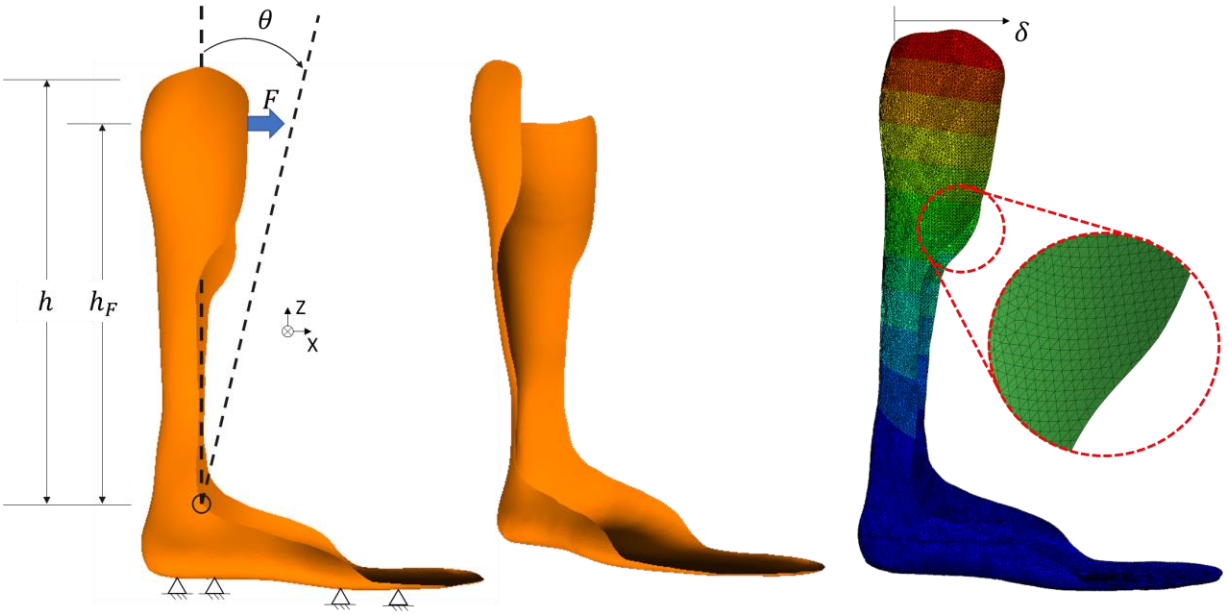

(a) (b) (c)

Figure 3.11. (a) Side-view of fixed AFO TWS for finite element CSM of a uniform wave infill. (b) Isometric view of AFO. (c) AFO showing mesh and deflection, δ, of the AFO subjected to force F.

Table 3.7. Cantilever MEX TWSs with uniform wave infill period were analyzed. Effective core properties, E_Z^c, G_{YX}^c, and G_{YZ}^c were found for periods 1.5 and 3.0 mm. Stiffness, K, mass, M, and infill density were calculated for each analyzed cantilever. Beadwidth, W, thickness, T, and overlap, O were 0.5, 4.0, and 0.1 mm, respectively.

P (mm)	E_Z^c (MPa)	G_{YX}^c (MPa)	G_{YZ}^c (MPa)	K (N-m/°)	Infill Density (%)
1.15	571.6	57.7	350.7	23.3	98.5
3	177.1	35.2	161.4	3.8	56.1

3.6.2 Results from Finite Element CSM of an AFO TWS with Wave Infill

With the finite element CSM described in Sec. 3.6, the AFO with the period and effective core material properties shown in Table 3.7 were analyzed. The stiffness of the AFO with P = 1.15 mm and P = 3 mm was measured to be 4.2 N-m/° and 2.3 N-m/°, respectively. The CSM-estimated stiffness of the solid-filled AFO with P = 1.15 mm matches the stiffness of the experimentally measured stiffness of 3.8 N-m/° in Sec. 1.2 experiments. This finding indicates that the CSM technique can be applied to predict the stiffness of the AFO. For the P = 3 mm AFO, the stiffness is reduced by half of stiffness of the solid AFO. This finding indicates that the stiffness of the AFO can be tuned by altering the period within the part. Also, these applications demonstrate the effectiveness of CSM in predicting the stiffness of TWSs with generalized geometries and loading conditions.

3.7 Conclusions

This study presented the finite element CSM for the modelling of the MEX wave infill of TWSs with generalized geometries and loadings. In CSM, the wave infill and TWS faces are modelled as a homogenous stacked composite, which reduces computation and setup time. Analytical models were presented to determine the effective material properties of the homogeneous core of the CSM. Using the effective material properties from these analytical models, the CSM was validated using previously reported stiffness values from four-point flexural experiments. The CSM of this four-point flexural setup predicted stiffness of the specimens within 15% of experimental measurements. Using CSM, a fixed flat-plate cantilever and AFO with uniform and varying wave infill were analyzed. These analyses show CSM to be a powerful finite element tool that can be used in the future to optimize the wave infill for TWSs.

Chapter 4
Thresholding Method for the Computed Tomography Inspection of the Internal Composition of Parts Fabricated using Additive Manufacturing

4.1 Abstract

This study presents a thresholding method for analyzing and quantifying the internal composition of additive manufacturing (AM) parts using computed tomography (CT) data. A Mixed Skew Gaussian Distribution (MSGD) algorithm, derived from a statistical image analysis technique called Mixed Gaussian Distribution (MGD) clustering, integrates a mixture of skewed Gaussian distributions to model the internal phases from CT data. The parameters of the MSGD algorithm (i.e. probability, mean, standard deviation, and skew) are inferred from the measured grayscale histogram using the least-squares fitting and assigned to phases present in the CT data. Upon fitting, the MSGD technique guides the thresholding of phases in CT data. From the MSGD fitted and thresholded CT data, phase volume percentages and spatial variations of density of the phases are quantified. The MSGD algorithm was validated using previously reported CT analysis and experimental porosity measurements of a Cobalt Chrome (CoCr) specimen fabricated by powder bed fusion (PBF). Compared with the 13.5% porosity measured by the Archimedes method, the MSGD method predicted 14.5% +/- 1.9% porosity, a measured increase of 1.0%. This difference may due to surface pores, which were neglected in the density measurement using the Archimedes method.

4.2 Introduction

Additive manufacturing (AM) is a layer-by-layer material deposition process that is increasingly being applied to create customized, high-performance end-use parts. Parts fabricated

with AM commonly exhibit intentional or unintentional porosity. Unintentional porosity typically occurs between adjacent layers as well as within the deposited material and may yield poor part performance by adversely affecting part mechanical properties. Intentional uses of porosity within AM parts include stiffness and damping tuning, complex cooling channels, slots for embedded electronics, or scaffolding for biologic in-growth. For both intentional and unintentional porosity, AM parts require methods of quantitative inspection for quality control of these internal features.

Quantitative inspection techniques for quality control of AM parts can be grouped into destructive and non-destructive testing methods. Destructive testing methods provide a macroscopic characterization of the structure but typically do not provide localized information of the porous internal structure of the part. Non-destructive testing methods, such as computed tomography (CT), can provide detailed internal views of the inspected part without damaging the specimen. CT uses X-rays and reconstruction techniques to visualize the internal structure of a specimen with sub-μm scale resolution. This study discusses the use of CT and the advancement of a segmentation algorithm that processes CT data to quantify the internal structure of AM parts and that provides physical insights into part density.

In Sec. 4.3, prior experimental work on the porosity quantification of powder bed fusion (PBF) Cobalt-Chrome (CoCr) AM parts by Slotwinski et al. [39] and Kim et al. [42] at NIST is presented and their CT inspection process for these parts is discussed. In Sec. 4.4, CT image processing techniques, specifically a mixed skew Gaussian distribution method (MSGD) and a thresholding and small feature filtering algorithm, for analyzing the internal structure of the CT-scanned filament and part are presented. In Sec. 4.5, the algorithm is validated based on CT data from Slotwinski et al. [39]. For validation, the porosity of NIST CoCr part CT data is analyzed and compared to the measurements [42]. Conclusions and discussions are presented in Sec. 4.6.

4.3 Experimental Setup

In this section, experimental porosity measurements from Slotwinski et al. [39] of a Cobalt Chrome (CoCr) powder bed fusion (PBF) part are described. Experimental measurements [39] are used as the standard for validation of CT data analysis algorithms.

4.3.1 Archimedes Method Measurement of Porosity of CoCr Parts [39]

The Archimedes method was utilized to experimentally measure the porosity of AM parts at NIST [39]. Based on the mass of the PBF CoCr cored cylinder measured in both water and air, the density of water, and the density of CoCr, the porosity of the CoCr AM part could be measured. In this study, "Sample 5" with 13.5% porosity [39] was selected as the "gold standard" to validate subsequent CT analyses.

4.3.2 CT Setup and Measurement of Porosity of CoCr Parts [39,42]

In [39] and [42], the porosity of the PBF CoCr cored cylinder was estimated using the data acquired in an industrial CT, with a rotating specimen and fixed X-ray source. Upon passing through the specimen, the concentrated X-ray is attenuated linearly according to the regional density at the exposed location. For example, a higher regional density corresponds to higher X-ray attenuation, and a lower regional density corresponds to lower X-ray attenuation. The attenuated X-ray is projected onto a 2D detector plate for each rotational angle, and the resulting X-ray intensity is recorded. A reconstruction procedure is then used to assign a grayscale value, which is linearly mapped from the measured X-ray intensity [44], to each incremental volume, or voxel, throughout the part [44]. From the 3D volume, 2D image slices are generated, as shown in Figure 4.1(a), which are composed of voxels with grayscale intensity values, I, at a position (x, y) within the image. As shown in Figure 4.2(a), the intensity values, $I(x, y)$, can then be mapped to

a measured histogram, $h_m(I)$, of intensity values and their frequencies of occurrence in the CT image.

For the CoCr PBF cylinder in [39], a CT scan was taken at a 3D voxel resolution of 2.52 μm^3. Each voxel had a corresponding intensity represented by a 16-bit grayscale intensity value between 0 to 65535. The cored cylinder was reconstructed into 758 image slices (2.48 mm x 2.55 mm x 2.52 mm). A cross-sectional CT image of the PBF CoCr, as shown in Figure 4.1(a), was used to identify and segment two internal phases: pore and CoCr (Figure 4.1(b)). Analyses [39] and [42] of the CT data of the PBF cored cylinder ("Sample 5" in [39]) estimated a porosity of 12.0% and 10.9%, respectively.

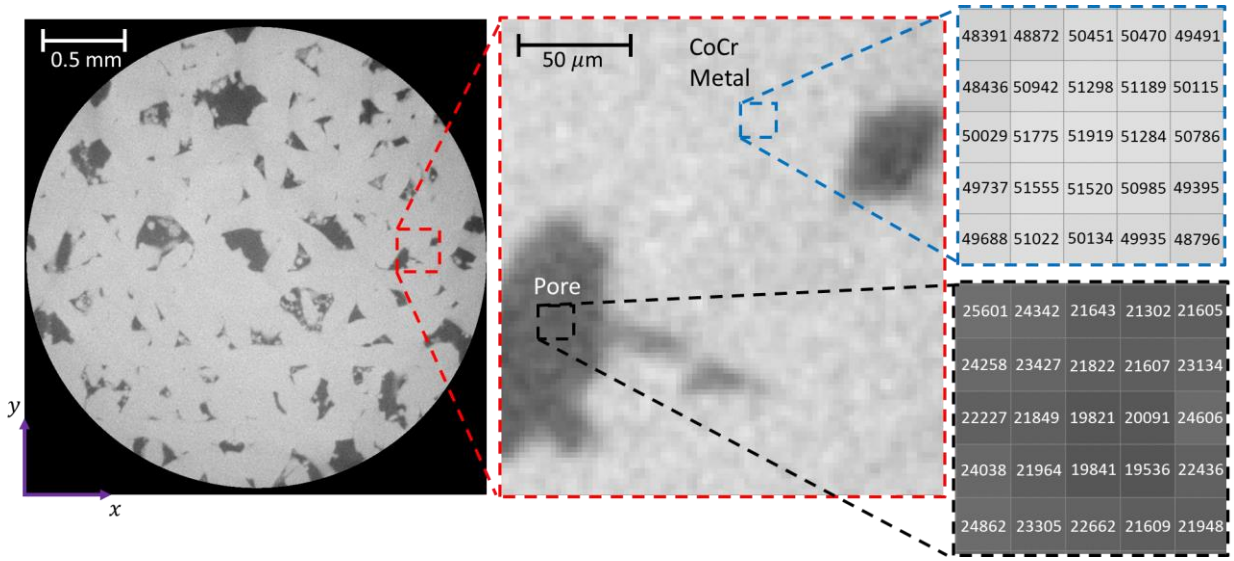

Figure 4.1. (a) CT image of the PBF CoCr part, which is composed of (b) pore and CoCr phases with grayscale values proportional to the measured X-ray intensity.

4.4 CT Image Processing and Segmentation Algorithm

Image processing and segmentation algorithms are presented for quantifying the internal structure of CT image slices.

4.4.1 CT Image Slicing and Histogram

From each CT image, a normalized histogram of voxel intensity frequency in grayscale was generated by normalizing the frequency of voxels at a grayscale level to the total number of voxels. An example of a measured histogram, denoted as $h_m(I)$, for the CoCr PBF specimen (Figure 4.1(a)) showing the voxel intensities, I, in grayscale vs. the normalized voxel frequency is shown in Figure 4.2(a). Because the CT process contains noise, edge effects, and imperfect material and beam size [46], the measured histogram of a homogeneous material will be distributed about a mean intensity value (in grayscale) proportional to the density of the scanned material. For a heterogenous material comprised of n phases with varying volume ratios, the histogram will be composed of n distinct individual modes, ψ_i ($i = 1, \dots, n$), each centered about a mean attenuation corresponding to the relative density of each phase. When the relative density (and attenuation) of the phases are similar and the contrast between the phases are poor, the modes are mixed into a single, superposed unimodal histogram of normalized voxel frequency vs. intensity.

For example, the measured histogram, $h_m(I)$, of the CoCr PBF specimen in Figure 4.2(a) can be decomposed into $n = 2$ modes, $\psi_1 = \psi_P$ and $\psi_2 = \psi_C$, where $n = 1$ is the pore (P) phase and $n = 2$ is the PBF CoCr (C) phase, respectively, as shown in Figure 4.2(b). These two phases sum to an estimated histogram, $h_e(I)$, which is fit to $h_m(I)$. Several segmentation techniques have been developed to distinguish between the two phases within the CT scanned specimen.

4.4.2 Review of Segmentation Techniques

Segmentation techniques have been developed for unimodal and multimodal segmentation of CT data. These techniques can be grouped into histogram shape-based, clustering-based, entropy-based, object attribute-based, spatial-based, and local-based methods [65]. For segmentation and analysis of NDT images such as those from CT, mixed Gaussian distribution

(MGD) clustering [66,67] is recognized as one of the best-performing segmentation algorithms [65] to distinguish between the internal phases of a scanned specimen because it models the inherent randomness of the CT measurement process. In MGD clustering, the imaged internal phases are modeled as a mixture of Gaussian distributions. Parameters of the Gaussian distributions (i.e. probability, mean, and standard deviation) are inferred from the measured grayscale histogram using least-squares fitting. By fitting with the MGD technique, the randomness of the CT process is modeled and used to guide the thresholding of the CT data. For example, as shown in Figure 4.2(b) of the CoCr PBF specimen, each phase of the CT data can be modeled as a Gaussian distribution with a mean and standard deviation value of pore and PBF CoCr grayscale values. These two modeled phases are combined to fit the measured histogram of the CT data.

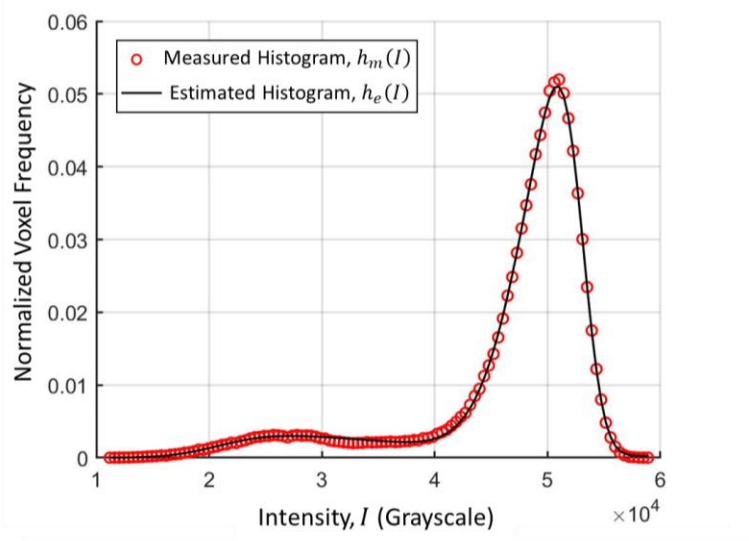

(a)

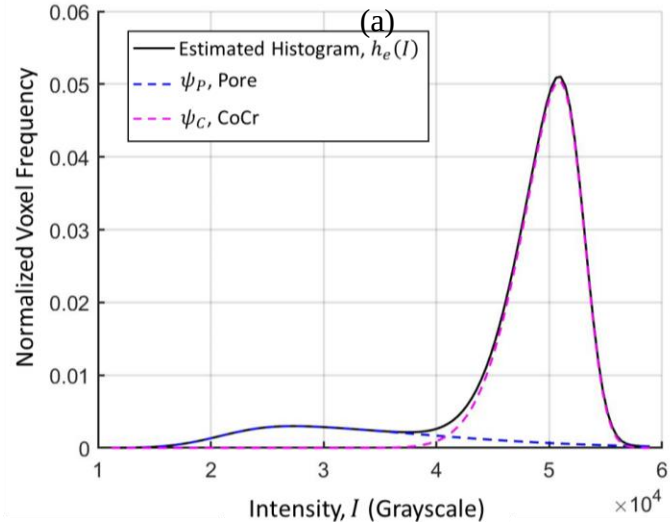

(b)

Figure 4.2. From the CoCr PBF cylindrical specimen CT slice image shown in Figure 4.1(a): (a) the measured normalized histogram, $h_m(I)$, of voxel intensity values in grayscale with the estimated histogram, $h_e(I)$, and (b) the CoCr PBF cylindrical specimen composed of two phases – CoCr and pore – with two distinct modes. The two phase modes sum to the estimated histogram, $h_e(I)$, which is fit to $h_m(I)$.

4.4.3 MGD of CT Images

In the generalized case where the CT data has n distinct phases, the MGD technique generates n Gaussian distributions, ψ_i $(i = 1, \dots, n)$, about a mean intensity value. The estimated histogram $h_e(I)$ is then the superposition of the Gaussian phase modes ψ_i:

$$h_e(I|\,\mu_i,\sigma_i,P_i)=\sum_{i=1}^{n}\psi_i\,(I\mid\mu_i,\sigma_i,P_i) \tag{4.1}$$

where I is the voxel intensity, μ_i is the mean of the i^{th} phase, σ_i is the standard deviation of the i^{th} phase, and P_i is the probability of the i^{th} phase. Phase parameters μ_i, σ_i, and P_i are inferred by fitting $h_e(I|\,\mu_i,\sigma_i,P_i)$ to the measured histogram, $h_m(I)$, of the CT data. The probability density function (PDF) of the i^{th} Gaussian phase mode ψ_i is:

$$\psi_i(I\mid\mu_i,\sigma_i,P_i)=P_i\,f_i(I\mid\mu_i,\sigma_i)=P_i\left(\frac{1}{\sqrt{2\pi\sigma_i^2}}e^{\frac{-(I-\mu_i)^2}{2{\sigma_i}^2}}\right) \tag{4.2}$$

$$\int_{-\infty}^{\infty}f_i(I\mid\mu_i,\sigma_i)\;dI=1 \tag{4.3}$$

$$\sum_{i=1}^{n}P_i=1 \tag{4.4}$$

where $f_i(I\mid\mu_i,\sigma_i)$ is the standard form of the Gaussian distribution. The phase modes, ψ_i, are ordered according to the magnitude of their mean value, i.e., $\mu_1<\cdots<\mu_i<\cdots<\mu_n$. Physically, μ_i and σ_i represent the average density (or X-ray attenuation) and density variation of the i^{th} phase, respectively, and P_i represents the phase volume percentage in the CT data.

For the CT data measured in this study, it was observed that the Gaussian distributions were skewed about a mean value. To account for these skewed distributions, this study uses a mixed skew Gaussian distribution (MSGD) method, which is discussed in the next section, to fit the measured histogram of the CT data.

4.4.4 MSGD of CT Images

Similar to MGD, the MSGD method generates n Gaussian distributions, ψ_i $(i = 1, \dots, n)$, that sum to $h_e(I)$ and whose parameters (i.e. mean, standard deviation, and probability) are inferred from $h_m(I)$ of the CT data. In CT data utilized in this study, however, the phase distributions were skewed about a mean value because of edge effects and the (lack of) contrast between components. To account for skewness in the normally distributed mode, the PDF of the i^{th} Gaussian phase mode ψ_i is:

$$\psi_i(I \mid \mu_i, \sigma_i, \alpha_i, P_i) = P_i\, f_i(I \mid \mu_i, \sigma_i, \alpha_i) = P_i \left(\frac{2}{\sqrt{2\pi\sigma_i^2}} e^{\frac{-(I-\mu_i)^2}{2{\sigma_i}^2}} \int_{-\infty}^{\alpha_i(\frac{I-\mu_i}{\sigma_i})} \frac{1}{\sqrt{2\pi}} e^{-\frac{t^2}{2}} dt \right) \quad (4.5)$$

$$\int_{-\infty}^{\infty} f_i(I \mid \mu_i, \sigma_i, \alpha_i)\ dI = 1 \quad (4.6)$$

$$\sum_{i=1}^{n} P_i = 1 \quad (4.7)$$

where $f_i(I \mid \mu_i, \sigma_i, \alpha_i)$ is the standard form of a skewed Gaussian distribution [68], μ_i is the mean of the i^{th} component, σ_i is the standard deviation of the i^{th} component, α_i is the skewness parameter of the i^{th} component, and P_i is the probability of the i^{th} phase. The phase modes, ψ_i, are ordered according to the magnitude of their mean value, i.e., $\mu_1 < \cdots < \mu_i < \cdots < \mu_n$. Physically, μ_i and σ_i represent the average density (or X-ray attenuation) and density variation of the i^{th} phase, respectively, P_i represents the phase volume percentage in the CT data, and α_i represents the magnitude and direction of the skew from the mean density of the material. Examples of the skew parameter of the Gaussian distribution are shown in Figure 4.3. A positive α skews the distribution to the right of the mean, and a negative α skews the distribution to the left of the mean. Increasing the magnitude of α shifts measurements to the left or right of the mean.

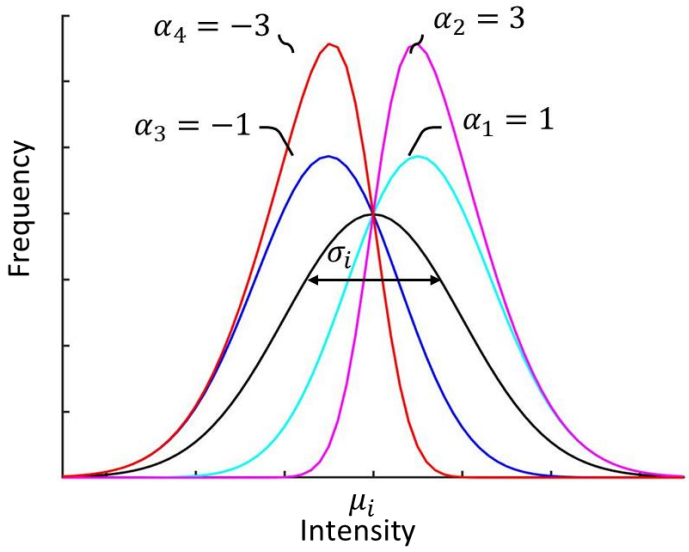

Figure 4.3. Representation of each parameter used in the MSGD fitting of the CT data histogram. Skew parameters $(\alpha_1 = |\alpha_3|) < (\alpha_2 = |\alpha_4|)$.

With a vector parameter, $\boldsymbol{\omega_i}$, defined to represent $[\mu_i, \sigma_i, \alpha_i, P_i]^T$, the estimated histogram $h_e(I|\boldsymbol{\omega})$ is then the superposition of the Gaussian phase modes, $\psi_i(I\ |\boldsymbol{\omega_i})$:

$$h_e(I|\boldsymbol{\omega}) = \sum_{i=1}^{n} \psi_i\ (I\ |\boldsymbol{\omega_i}) \tag{4.8}$$

The least-squares fitting error, $\epsilon(I|\boldsymbol{\omega})$, between the measured $h_m(I)$ and estimated $h_e(I|\boldsymbol{\omega})$ is:

$$\epsilon(I|\boldsymbol{\omega}) = |h_m(I) - h_e(I|\boldsymbol{\omega})| \tag{4.9}$$

where $|\bullet|$ is the Euclidean norm (i.e. $\sqrt{\epsilon_1^2 + \cdots + \epsilon_p^2}$). The vector parameters, $\hat{\boldsymbol{\omega}}$**,** that minimize the least-squares fitting error, $\epsilon(I|\boldsymbol{\omega})$, (i.e. the argmin function) are:

$$\hat{\boldsymbol{\omega}} = \underset{\boldsymbol{\omega}}{\operatorname{argmin}}(\epsilon(I|\boldsymbol{\omega})) \tag{4.10}$$

which is subject to the constraints:

$$\eta_i: \quad C_i^l \leq \mu_i \leq C_i^u \tag{4.11}$$

$$\gamma_i: \quad \sum_{i=1}^{n} P_i = 1 \tag{4.12}$$

where η_i is the lower and upper bound constraint on the mean value, μ_i; C_i^l, and C_i^u are the lower and upper bound grayscale values, respectively, that encompass the i^{th} phase peak intensity value on the histogram; γ_i is the equality constraint on the sum of the n phase probabilities, P. To guide the optimization of Eq. (4.10), the lower and upper intensity bounds (C_i^l and C_i^u) indicate a region of intensity values that the phase mean, μ_i, is expected to be located. These bounds are provided based on examination of the i^{th} phase intensity values $I(x, y)$ from the CT data.

A numerical gradient-based optimization, *fmincon* in Matlab, was used to find $\widehat{\boldsymbol{\omega}}$ with Eq. (4.10) subject to the constraints in Eqs. (4.11) and (4.12). To initialize the least-squares optimization, constraints C_i^l and C_i^u and initial conditions for $\boldsymbol{\omega_i}$ are provided, as will be discussed in Sec. 4.5.1. From the optimization, parameters $\widehat{\boldsymbol{\omega}}_{\boldsymbol{i}}$ are defined for each phase ψ_i ($i = 1, \dots, n$). From $\psi_i(I\,|\widehat{\boldsymbol{\omega}}_{\boldsymbol{i}})$, regions of intensity values on the CT histogram are assigned to a phase, a process known as thresholding, for visualization of the separate phases in the CT data. Because of the Gaussian modes, thresholding regions are determined using a Bayesian decision rule (BDR), which is described in Sec. 4.4.5.

4.4.5 Thresholding of CT Images using BDR

For analysis and visualization of the CT image, the CT data is thresholded, which is the process of determining the intensity regions on the measured histogram that are associated with a phase [69]. The CT data, with grayscale intensity values $I(x, y)$, is simplified to a thresholded image, $T(x, y)$, with n unique intensity values corresponding to each phase. For the n phases, ψ_i ($i = 1, \dots, n$), modeled as Gaussian distributions with mean values ($\mu_1 < \cdots < \mu_{i-1} < \mu_i <$

$\cdots < \mu_n$), BDR is used to generate $n-1$ threshold limits, L_i $(i = 1, \ldots, n-1)$ between adjacent phase distributions, ψ_{i-1} and ψ_i. The grayscale intensity region, $\Re_i$, for ψ_i, is:

$$\Re_i \in (L_{i-1}, L_i\,] \tag{4.13}$$

where L_{i-1} and L_i are intensity limits between phase distributions ψ_{i-1} and ψ_i and ψ_i and ψ_{i+1}, respectively. For the special cases of ψ_1 and ψ_n, the regions $\Re_1$ and $\Re_n$ are:

$$\Re_1 \in [\min(I)\,, L_1] \tag{4.14}$$

$$\Re_n \in (L_{n-1}, \max(I)] \tag{4.15}$$

where L_1 and L_{n-1} are intensity limits between phase distributions ψ_1 and ψ_2 and ψ_{n-1} and ψ_n, respectively, and $\min(I)$ and $\max(I)$ are the minimum and maximum intensities of the CT data. The thresholded image, $T(x, y)$ is therefore:

$$T(x, y) = B_i \;\forall\; I(x, y) \in \Re_i \tag{4.16}$$

where the intensities $I(x, y)$ in $\Re_i$ are mapped to a unique value, B_i for $i = 1, \ldots, n$. The generalized form of BDR for determining the threshold limit L_i is [66]:

$$L_i = \frac{\mu_{i-1}\,\sigma_i^2 - \mu_i\,\sigma_{i-1}^2}{\sigma_i^2 - \sigma_{i-1}^2} + \frac{\sigma_{i-1}\,\sigma_i}{\sigma_i^2 - \sigma_{i-1}^2}\left((\sigma_i^2 - \sigma_{i-1}^2)\log\left(\frac{\sigma_i^2}{\sigma_{i-1}^2}\right) + 2(\sigma_{i-1}^2 - \sigma_i^2)\log\left(\frac{P_i}{P_{i-1}}\right) + (\mu_{i-1} - \mu_i)^2 \right)^{\frac{1}{2}} \tag{4.17}$$

For example, within a CT data histogram (Figure 4.4(a)) corresponding to the CoCr PBF part CT image (Figure 4.4(b)), BDR yields two regions, $\Re_1 = \Re_P$ and $\Re_2 = \Re_C$, for the pore and PBF CoCr phases, respectively:

$$\Re_P \in [\min(I), L_P] \tag{4.18}$$

$$\Re_C \in (L_P, \max(I)] \tag{4.19}$$

where L_P is the intensity limit between ψ_P and ψ_C. The thresholded image, $T(x, y)$, is then:

$$T(x,y) = \begin{cases} B_P \; \forall \; I(x,y) \in \Re_P \\ B_C \; \forall \; I(x,y) \in \Re_C \end{cases} \tag{4.20}$$

where B_P and B_C are unique intensity values prescribed to the pore and PBF CoCr phase regions, respectively, as shown in Figure 4.4(c). The CoCr PBF is analyzed and the resulting thresholded image, $T(x, y)$, is shown in Figure 4.4(d).

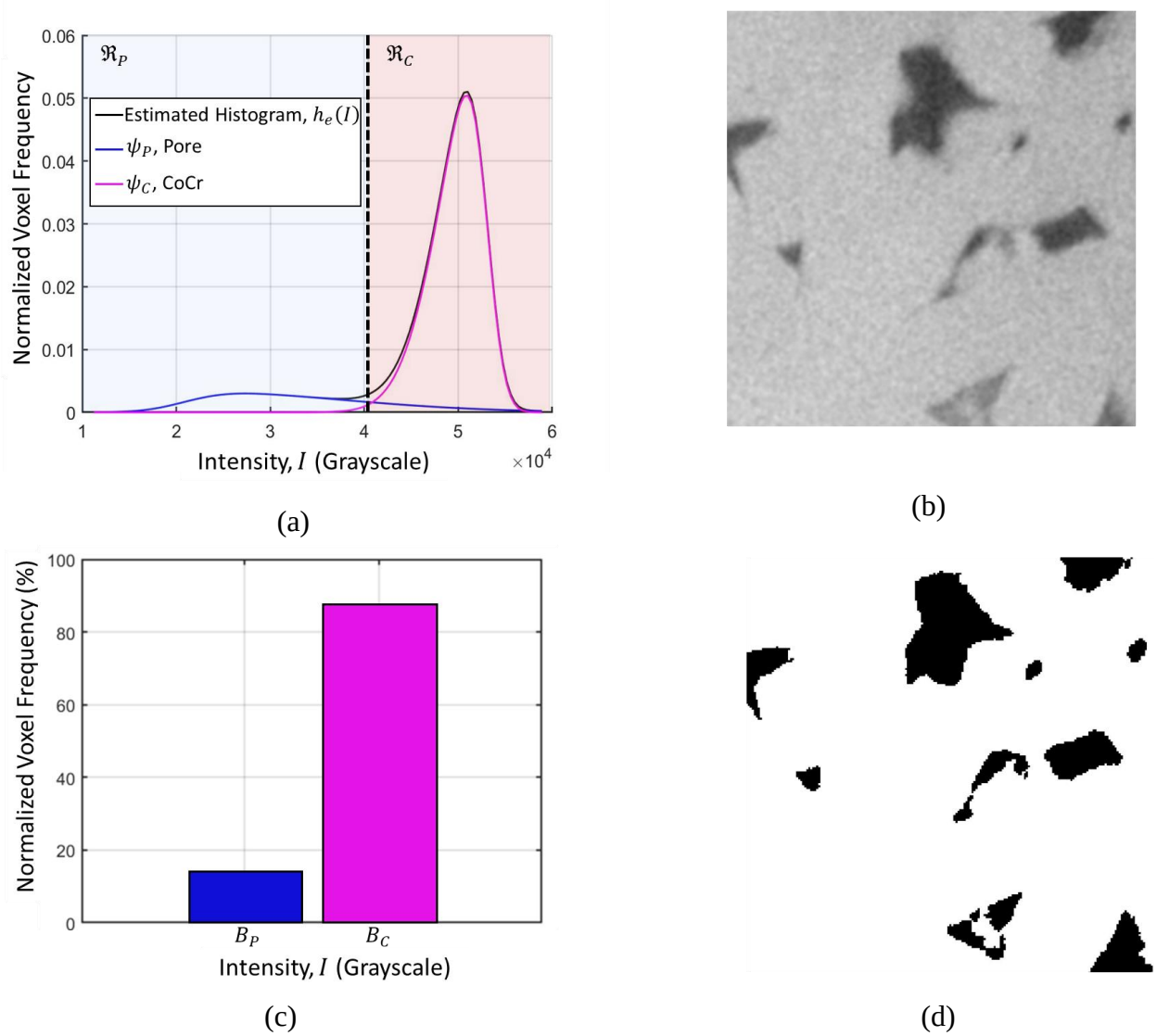

Figure 4.4. (a) The MSGD algorithm fits an estimated histogram $h_e(I)$ with two Gaussian distributions (ψ_P, and ψ_C), representing the pore and PBF CoCr, respectively, to the measured CT data. BDR is used to generate regions $\Re_P$ and $\Re_C$ corresponding to the intensity values associated with the pore and CoCr phases, respectively. (b) With this process, the data in the intensity regions $\Re_P$ and $\Re_C$ of the CT image are (c) assigned unique intensity values, B_P and B_C, respectively, and are converted into the (d) thresholded image $T(x, y)$.

4.4.6 Small Feature Filtering

Because of the overlapping distributions, the thresholded image $T(x, y)$ (Figure 4.5(a)) yields small connected features that are smaller than the resolving power of the CT machine, as marked in Figure 4.5(b). These small features do not have physical meaning and, therefore, are filtered and blended into the surrounding image features.

Filtering small features requires identifying connected phases in the thresholded CT image $T(x, y)$ that have a volume smaller than a minimum volume, V_{min}. V_{min} is based on the resolving capability of the CT machine, which is a multiple, m, times the voxel volume. Therefore, V_{min} is defined as:

$$V_{min} \coloneqq V_{conn} \leq m\, V_V \tag{4.21}$$

where V_V is the voxel volume of the scan and V_{conn} is the volume of the connected features. Connected features are voxel sets of a single phase that are connected through a common edge or corner. To find all the connected features in $T(x, y)$, *bwconncomps,* a Matlab function, was used. After identifying V_{min}, the intensity values of each small feature in the CT data $I(x, y)$ are adjusted to the mean value, μ_i, of the phase surrounding the small feature. MSGD and BDR were performed on the adjusted image. This procedure is repeated until the number of small features stabilizes after several iterations or reaches zero. As opposed to simply removing small features in the thresholded image, the small feature intensity values are replaced with the optimized mean value of the region surrounding the small feature in the original CT image and the MSGD algorithm is repeated.

Figure 4.5 shows an example of small feature filtering for the CoCr part. In the CoCr PBF part CT scan, the voxel volume, V_V was 2.52 μm^3 and m was 3 [46]. Therefore, the CT scanner's capability for resolving a minimum feature size, $V_{min} = 7.5$ μm^3 (Figure 4.5(b)). After four iterations of the procedure outlined above, the number of small components reached zero or stabilized from the previous iteration. The region of Figure 4.5(b) after small feature removal is shown in Figure 4.5(c).

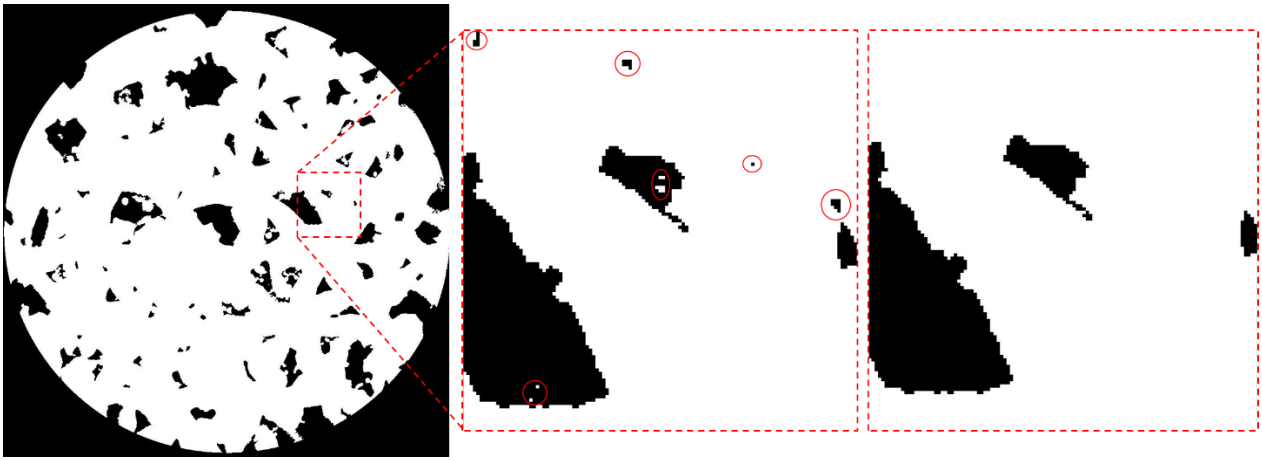

(a) (b) (c)

Figure 4.5. (a) Representative thresholded CT slice of CoCr PBF specimen with two components: pore (black) and CoCr PBF (white). (b) Small features below the resolution power of the CT scanner are identified and circled. The original image $I(x, y)$ is replaced with the phase mean value surrounding the small feature, and MSGD and BDR are performed again. (c) This process is iterated until small components are removed.

4.4.7 CT Image Analysis Algorithm: MSGD Algorithm

To process the CT image slices, the algorithm used for CT image processing (i.e. the MSGD algorithm) in this study is shown in Figure 4.6. The steps of the algorithm and the sections in which each step is discussed are: 1) CT image slicing and histogram generation (Sec. 4.4.1), 2) MSGD fitting of the CT histogram (Sec. 4.4.4), 3) image thresholding using BDR (Sec. 4.4.5), and 4) small feature filtering (Sec. 4.4.6).

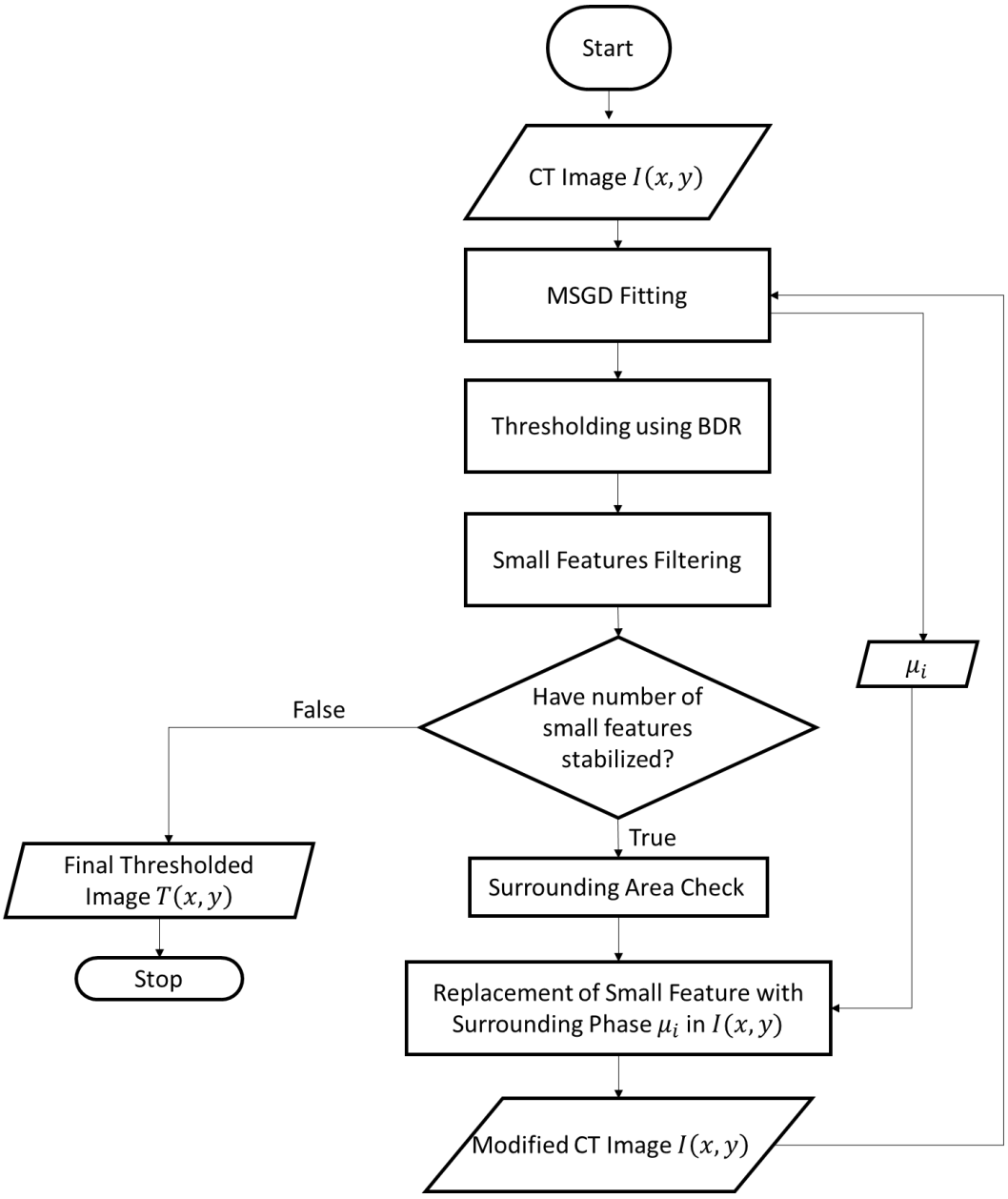

Figure 4.6. Algorithm for processing the CT data to identify phases.

4.5 Results from the MSGD Segmentation of the PBF CoCr Cored Cylinder

In this section, the MSGD algorithm of Sec. 4.4 (Figure 4.6) will be validated using experimental porosity measurements from Slotwinski et al. [39] of a CoCr PBF part. Sec. 4.5.1 describes the CT histogram, MSGD fitting initialization, thresholding, and small feature filtering results. Sec. 4.5.2 presents the porosity results of the PBF CoCr cylinder from the MSGD

algorithm. Sec. 4.5.3 compares the porosity estimates for the CoCr part using the MSGD algorithm and the experimental Archimedes method.

4.5.1 Optimization Setup of MSGD Algorithm for PBF CoCr Cored Cylinder

The algorithm was applied to analyze the PBF CoCr cored cylinder CT data of Figure 4.1(a), provided by the author of [42]. The experimental measured histogram $h_m(I)$ is shown in Figure 4.7(a). The Pore (P) Gaussian mode $\psi_P(I|\boldsymbol{\omega_P})$ and CoCr (C) Gaussian mode $\psi_C(I|\boldsymbol{\omega_C})$ were the two phases (i.e. $n = 2$) presented. To fit $h_m(I)$, an estimated histogram, $h_e(I|\hat{\boldsymbol{\omega}})$ was fit according to Eq. (4.10) where $\hat{\boldsymbol{\omega}} = [\hat{\boldsymbol{\omega}}_{\boldsymbol{P}}, \hat{\boldsymbol{\omega}}_{\boldsymbol{C}}]$ were the optimized vector parameters for the pore and CoCr phases. To guide the optimization of Eq. (4.10), C_P^l and C_P^u were the region of intensity values that the pore phase mean, μ_P, was expected to be located. Similarly, C_C^l, and C_C^u were the region of intensity values that the CoCr phase mean, μ_C, was expected to be located. These bounds were determined based on examination of the phase intensity values $I(x, y)$ from the CT image in Figure 4.1(b) and $h_m(I)$ in Figure 4.7(a). Figure 4.7(a) shows the upper and lower bound intensity regions, C_P^l, C_P^u, C_C^l, and C_C^u, that were provided for the constraints of Eq. (4.11). Table 4.1 shows the initial conditions for all $\boldsymbol{\omega}$ parameters.

The estimated histogram, $h_e(I|\hat{\boldsymbol{\omega}})$, and two Gaussian modes $\psi_P(I|\boldsymbol{\omega_P})$ and $\psi_C(I|\boldsymbol{\omega_C})$ are shown in Figure 4.7(b). BDR was performed on two Gaussian modes to generate two intensity regions, $\Re_P$ and $\Re_C$, for the pore and CoCr phases, respectively, to generate thresholded image $T(x, y)$ shown in Figure 4.8(a). Comparing a region of the thresholded image in Figure 4.8(b) to the same region in the original CT image (Figure 4.8(c)), boundaries between the pore and the CoCr are clearly delineated and are appropriately identified.

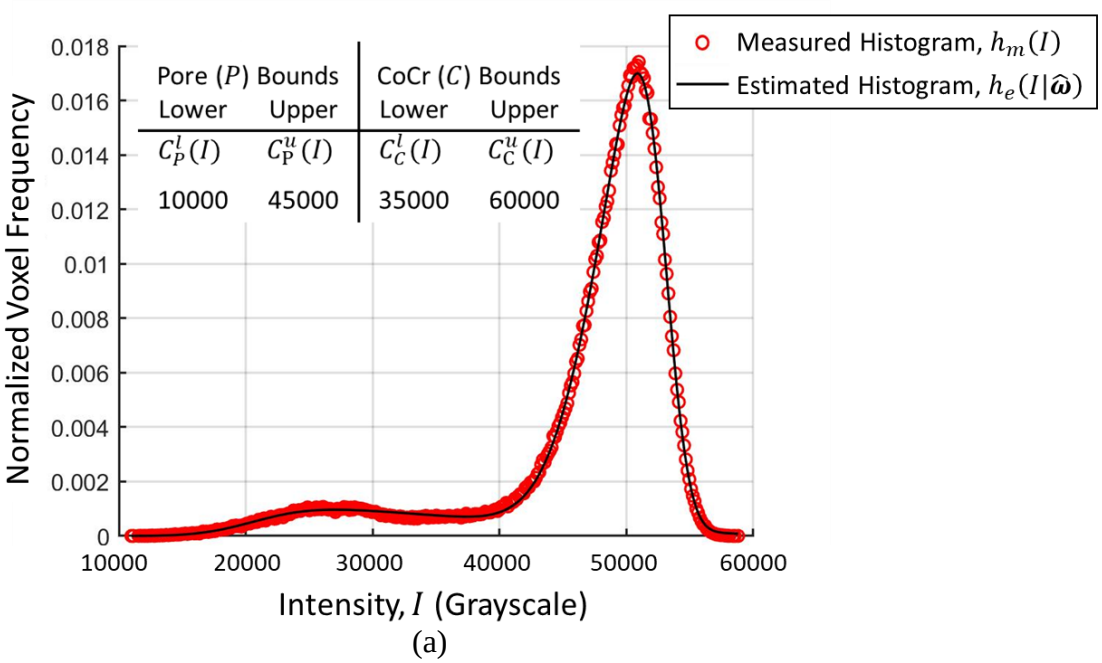

(a)

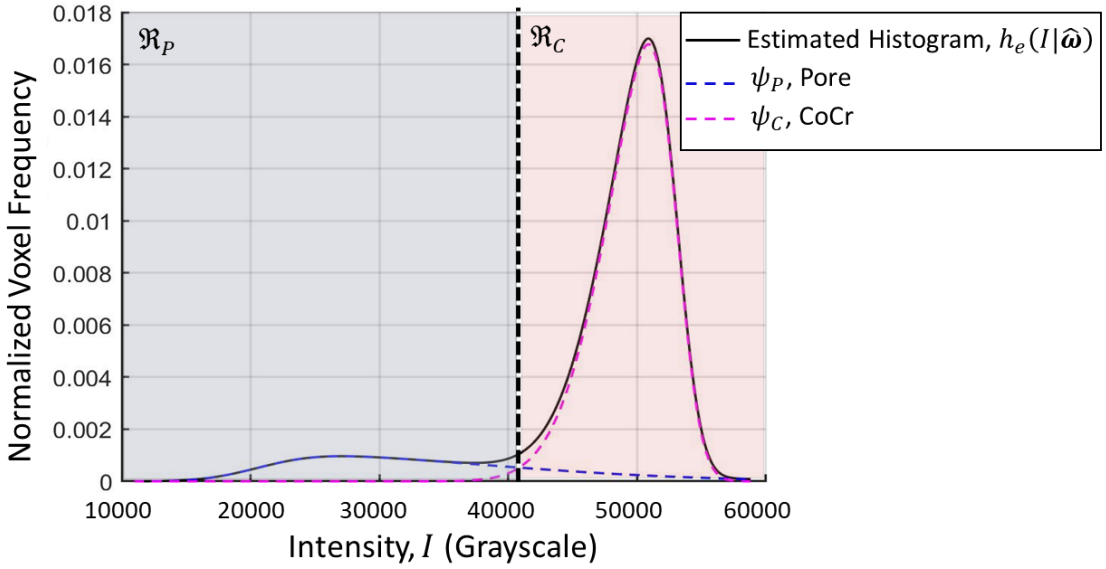

(b)

Figure 4.7. From the CoCr PBF cored cylinder CT slice image shown in Figure 4.1, (a) the measured normalized histogram, $h_m(I)$, of voxel intensity values in grayscale and estimated histogram, $h_e(I|\hat{\boldsymbol{\omega}})$, are generated. (b) The CoCr PBF cored cylinder is composed of two phases – pore and CoCr– with two Gaussian modes, ψ_P and ψ_C. The Gaussian modes sum to the estimated histogram, $h_e(I|\hat{\boldsymbol{\omega}})$. Using BDR, $h_e(I|\hat{\boldsymbol{\omega}})$ is thresholded into two intensity regions, $\Re_P$ and $\Re_C$, for pore and CoCr phases, respectively.

Table 4.1. MSGD algorithm initial conditions and optimized parameters for the PBF CoCr CT image slice shown in Figure 4.1(a). The fitted parameters, $\hat{\boldsymbol{\omega}}$, generate the estimated histogram, $h_e(I)$ of Figure 4.7(b).

	Phase	$\mu_i(I)$, Phase mean	$\sigma_i(I)$, Phase Standard Deviation	P_i, Phase Volume Percentage (%)	α_i, Phase Skew
Initial Conditions, $\boldsymbol{\omega}$	Pore, $\psi_P(I\|\boldsymbol{\omega})$	27000	700	30.0	0.0
	CoCr	55000	700	70.0	0.0
Optimized Parameters, $\hat{\boldsymbol{\omega}}$	Pore, $\psi_P(I\|\hat{\boldsymbol{\omega}})$	20700	16936	16.0	4.9
	CoCr, $\psi_C(I\|\hat{\boldsymbol{\omega}})$	53020	4502	84.0	-3.0

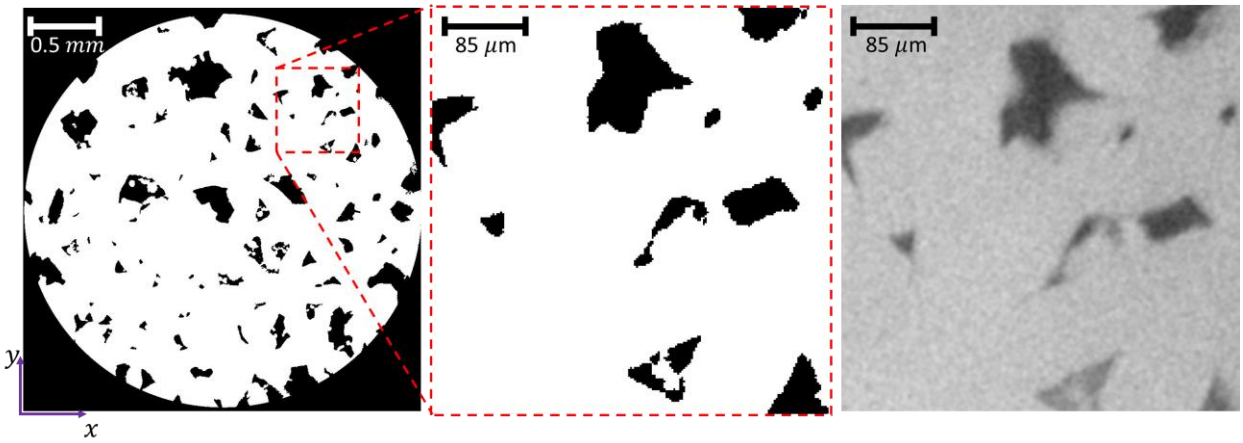

(a) (b) (c)

Figure 4.8. (a) Thresholded image, $T(x, y)$, corresponding to the CoCr PBF cored cylinder CT slice image shown in Figure 4.1 and the phase threshold regions, $\Re_P$ and $\Re_C$, for pore and CoCr phases, respectively, shown in Figure 4.7(b). In the thresholded images, the black color corresponds to pore, and the white color corresponds to CoCr. Comparing the thresholded region of (b) to the original CT image (c), the pore and CoCr regions are clearly delineated and are appropriately identified.

4.5.2 Results from MSGD Algorithm for PBF CoCr Cored Cylinder

Table 4.1 shows results from the optimization of the single CT slice image shown in Figure 4.1(a). The mean grayscale intensity values of the pore, μ_P, and CoCr, μ_C, were 20702 and 53021, respectively, which matches the intensity values shown in Figure 4.1(b) for both phases. The standard deviations for the pore, σ_P, and CoCr, σ_C, were 16936 and 4502, respectively, indicating that the pore intensity values were more widely spread about their mean intensity value than were

the CoCr phase values. However, the skew parameters for the pore, α_P, and CoCr, α_C, demonstrate the CoCr values were skewed negatively from their mean value. Physically, the skew of the CoCr may provide an indication of the amount of loose, un-sintered or poorly sintered powder in the metal matrix. Finally, the volume percentage of pore, P_P, and CoCr, P_C, are 16.0% and 84.0%, respectively. P_P is the porosity of the cored cylinder.

Based on MSGD algorithm of Sec. 4.4, all 758 CT image slices of the CoCr PBF specimen were analyzed. Figure 4.9 shows the localized pore and CoCr volume percentage, P_P and P_C, for each CT slice along the length of the CoCr cylinder. From Figure 4.9, the maximum and minimum porosity measured through the axial length of the CoCr cored cylinder was 22.1% and 10.6%, respectively. The average porosity across the axial length of the CT scanned cored cylinder was measured to be 14.5% with a standard deviation of 1.9%.

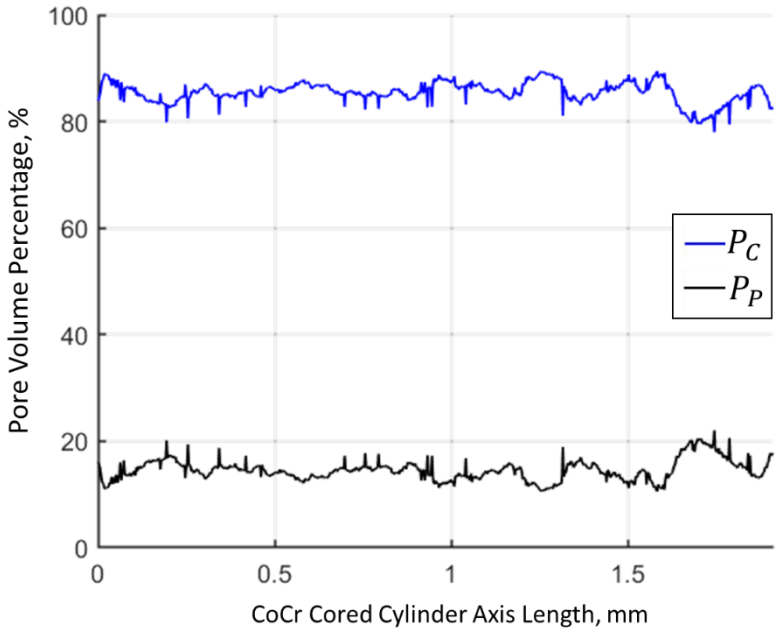

Figure 4.9. Volume percentage of pore and CoCr metal across the length of the PBF CoCr cored cylinder.

4.5.3 Comparison of CoCr Part Porosity using Archimedes Method and MSGD Algorithm

As summarized in Table 4.2, the MSGD algorithm estimated a porosity of 14.5% +/- 1.9% for the CoCr PBF part. This estimate matches closely with a porosity of 13.5% experimentally measured using Archimedes method in [39]. Differences in the estimates may be due to several reasons. One difference is that Archimedes method assumes that the part being measured has no surface pores that allow for water infiltration during measurement. However, as shown on the edges of the PBF CoCr cylinder in Figure 4.1, pores exist on the surface of the cylinder. These surface pores will not be accounted for when using Archimedes method, which will result in a lower experimental porosity measurement. Porosity measurements using CT do not suffer from this drawback, and thus, CT is expected to predict a higher average porosity, which is true for the porosity measured by the MSGD algorithm. Another potential reason is that only a fraction of the entire CoCr cored cylinder was scanned (2.5 mm scan length vs. 10 mm height of cored cylinder), whereas Archimedes method is a measurement of the total porosity of the part. The other difference may be the contrast between phases due to the lack of resolution or other artifacts present in CT image.

Table 4.2. Comparison of porosity measurements for validation of the MSGD method

	Experimental	**CT Analyses**			
	Archimedes Method Porosity [39]	CT Analysis [39]	CT Analysis [42]	MSGD Average Porosity	MSGD Standard Deviation of Porosity
Sample 5 (PBF CoCr)	13.5%	12.0%	10.9%	14.5%	1.9%

4.5.4 Comparison of MSGD with MGD

MSGD and MGD method results were compared to determine the effect of skew, α, in fitting Gaussian distributions to the CT data. Figure 4.10 shows the measured histogram, $h_m(I)$, of Figure 4.1(a) fitted with an MGD estimated histogram, $h_e(I|\hat{\boldsymbol{\omega}})$. The estimated histogram was

fitted using the same initial conditions of Table 4.1 but without a skew term, α. Figure 4.10 shows an average MGD method least-squares error between $h_m(I)$ and $h_e(I|\hat{\boldsymbol{\omega}})$ of 0.164. Error was determined as the average of the Euclidean norm of Eq. (9). Compared with the MSGD method average least-squares error of 0.027, the MGD error is 500% higher.

Table 4.3 shows the optimized parameters, $\hat{\boldsymbol{\omega}}$**,** of the MGD method across the length of the CoCr cylinder. The MGD method predicts a porosity of the cylinder of 17.2%, an overprediction of the experimental Archimedes Method Porosity by 4%. The comparison of MSGD and MGD method underscore the importance of the skew term in fitting the estimated and measured CT data histograms.

Table 4.3. MGD optimized parameters of pore and CoCr across the length of cylinder.

	Phase	$\mu(I)$, Phase mean	$\sigma(I)$, Phase Standard Deviation	P, Phase Volume Percentage (%)
Optimized Parameters, $\hat{\boldsymbol{\omega}}$	Pore, $\psi_P(I\|\hat{\boldsymbol{\omega}})$	30000	10550	17.2
	CoCr, $\psi_C(I\|\hat{\boldsymbol{\omega}})$	50300	2700	82.8

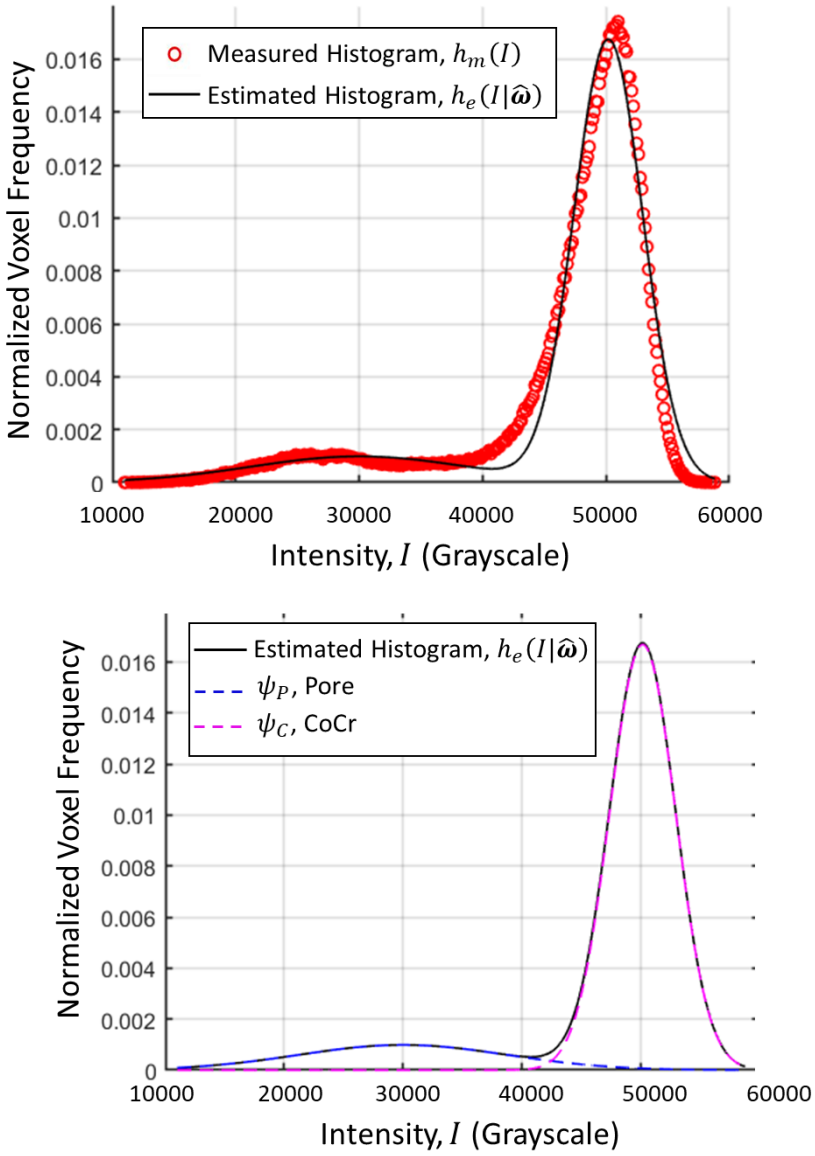

Figure 4.10. From the CoCr PBF cored cylinder CT slice image shown in Figure 4.1, (a) the measured normalized histogram, $h_m(I)$, of voxel intensity values in grayscale and estimated histogram, $h_e(I|\hat{\omega})$, are generated using MGD. (b) The CoCr PBF cored cylinder is composed of two phases – pore and CoCr– with two Gaussian modes, ψ_P and ψ_C. These Gaussian modes sum to the estimated histogram, $h_e(I|\hat{\omega})$.

4.6 Conclusions

This study presented a mixed skew Gaussian Distribution (MSGD) clustering method for analyzing and thresholding computed tomography images of AM parts. The MSGD algorithm was derived from Mixed Gaussian Distribution (MGD) clustering, in which the imaged internal phases were modeled as a mixture of Gaussian distributions. In MSGD, the parameters of a skewed

Gaussian distributions (i.e. probability, mean, standard deviation, and skew) were inferred from the measured grayscale histogram using the least-squares fitting. By fitting with the MSGD technique, the randomness of the CT process was modeled and used to guide the thresholding of the CT data. Furthermore, phase volume percentages and potential variations in the density of the phases were modeled and quantified.

The goal of the MGD and MSGD algorithm is to minimize the number of representative components that are used to fit the data to obtain the most physical meaning of the CT data. In theory, the CT data can be fit with an infinite set of delta functions at each intensity value. However, this infinite set will not provide meaningful information about the global distribution of component intensities throughout the part. Similar to data curve fitting, overfitting limits the effectiveness of the fitting process and reduces the physical meaning of the fitted curve.

The MSGD algorithm was validated using previously reported CT and experimental porosity measurements of an AM CoCr PBF part. Compared with the experimental Archimedes method results of the CoCr part, the MSGD method predicted a 1% higher porosity. The difference in porosity prediction may be accounted for by the limitations in the Archimedes method for surface pores, such as the CoCr part analyzed in [4].

Additionally, because of the global nature of the MSGD fitting process, various attributes of the CT data may be quantified. Firstly, the MSGD algorithm aims to model the random distribution of the voxel intensities with a skewed Gaussian distribution using the measured CT data. Therefore, the randomness of data may be used to estimate the phase percentages, mean density, and density distribution. Secondly, within the phase itself, the phase density may be skewed indicating a variation in the particle density of that phase. With respect to the CoCr PBF

specimen, this technique may provide a method for understanding the sintering quality and for determining the degree of un-sintered particles.

Limitations of the MSGD method (and CT analysis in general) lies in the difficulty of analyzing CT data with a unimodal histogram of grayscale intensities. The CT data with a unimodal histogram indicates that the phase densities have little grayscale contrast to the point that the phase distributions completely overlap. When this occurs, the process of analyzing and segmenting these data sets becomes difficult and leads to multiple solutions of the least-squares fitting problem. To improve the quality of these analyses, future work in software (i.e. improved algorithms for phase separation) and hardware (i.e. improved methodologies to increase the contrast between similar density phases) is required.

Chapter 5
Computed Tomography Evaluation of the Porosity and Fiber Orientation in a Short Carbon Fiber Material Extrusion Filament and Part

5.1 Abstract

The computed tomography (CT) evaluation of the material extrusion (MEX) of a short carbon fiber (SCF) Nylon-12 filament and part is presented. CT, a non-destructive testing method, was used to quantify the internal structure of specimens into three phases: pore, Nylon, and SCF. The intensity histograms from the CT data were fit using a mixed skew Gaussian distribution (MSGD) algorithm to segment the CT image into phases. Thresholded images were used to isolate pores in the CT image to determine pore volume and distribution within both the MEX SCF filament and part. The phase volume percentages of the MEX SCF filament were found to be 1.6% pore, 62.2% Nylon, and 36.2% SCF. The volume of most pores within the filament were found to be under 100 μm^3. The highest frequency of pores was located near the outside of the filament, but the large pores were located near the center of the filament. This result indicates that the thermoplastic filament extrusion process likely entraps large bubbles in the center of filament while bubbles at the periphery of the filament can escape during post-extrusion cooling. MSGD analysis of sections of the MEX SCF part estimated phase volume percentages to be 9.8% pore, 59.6% Nylon, and 30.9% SCF. This analysis showed a more than 8% increase in porosity from the MEX SCF filament to the part. For the MEX SCF part, the average pore area was found to be highest (>250 μm^2) at the bottom of the layer and smallest (<100 μm^2) at the top of the layer, which could be explained by a large temperature gradient between and contractile thermal stresses inside the layer that cause the thermoplastic to shrink into a smaller volume allowing the voids to grow.

5.2 Introduction

Material extrusion (MEX) is an additive manufacturing (AM) process in which a thermoplastic filament is extruded through a heated nozzle, which deposits material to build a part layer-by-layer [70]. Increasingly, MEX is being used to manufacture high-performance components for aerospace, biomedical, and other applications [3–6]. For these high-performance parts, short carbon fibers (SCF) are introduced as an additive in the MEX filament to increase the part strength and stiffness [38,71,72]. The quality of SCF MEX filaments, including the porosity and SCF distribution and spatial density, used to generate SCF MEX parts is critically important to their quality.

Composite MEX parts with SCF comprise a distribution of short fibers and surrounding thermoplastic matrix. SCFs are used to increase the strength and stiffness of MEX materials [73], but a high volume percentage of SCF may adversely increase the internal porosity [38]. Ning et al. [38] analyzed the tensile and flexural properties of SCF specimens fabricated by MEX and found that specimen strength and stiffness increased with SCF weight percentage until it decreased significantly after 15 wt% of SCF due to the significantly increased and uncontrolled porosity. To maximize SCF MEX part strength and stiffness, a balance exists between SCF density and porosity. Quantifying this balance requires inspection techniques that can visualize and quantify the internal structures. In this study, computed tomography (CT) is utilized for the inspection of the internal structure of a MEX SCF filament and part.

CT has been utilized increasingly to visualize fiber-filled molded polymer composites [39,41–46,74,75]. Kastner [45] applied CT to visualize the porosity in carbon fiber reinforced polymers. The CT data was analyzed using Otsu's thresholding method [52] to quantify the volume percentage and distribution of pores in the part. Garcea et al. reviewed the CT inspection

of polymer composites and the ability of CT to visualize the internal structure of both SCF and pore distribution, orientation, and morphology [44]. Nikishkov et al. [75] studied the visualization and segmentation of manufacturing defects based on CT data and proposed a new method for quantifying the porosity and void dimensions. For visualization of μm-scale features, Maire et al. [46] suggested a resolution-to-voxel ratio of 2 to 3 for CT data analysis. Therefore, to resolve the 8 μm diameter SCF, a voxel size below 2.5 μm is required. Due to the limited detector size in industrial CT and the short focus distance required to achieve a voxel size of 2.5 μm, small sample sizes must be used to visualize SCFs [44].

In Sec. 5.3, the MEX SCF filaments and specimens analyzed using CT are described, and the CT setup, process, and thresholding techniques are discussed. In Secs. 5.4 and 5.5, the composition of the MEX SCF filament and part are analyzed, respectively. Conclusions and discussions are presented in Sec. 5.6.

5.3 Experimental Setup

The MEX SCF filament and specimen, the CT study, and the CT image processing techniques are described in this section.

5.3.1 MEX Filament and Specimen

A SCF-embedded polyamide 10/12 (Nylon) filament sample, as shown in Figure 5.1(a), was taken from a larger filament roll and analyzed. The filament (provided by Stratasys, Eden Prairie, MN) had a nominal diameter of 1.75 mm, length of 3 mm, and approximately 35 wt% of SCF. The embedded SCFs had an average diameter of 8 μm and length of 100 μm. The fabrication method for the filament was the conventional melt-compounding extrusion. SEM micrograph of the end surface of the filament with Nylon and extruding SCF is shown in Figure 5.1(b). Using

CT analysis, the volume percentage and distribution of pore, Nylon, and SCF within this filament will be quantified.

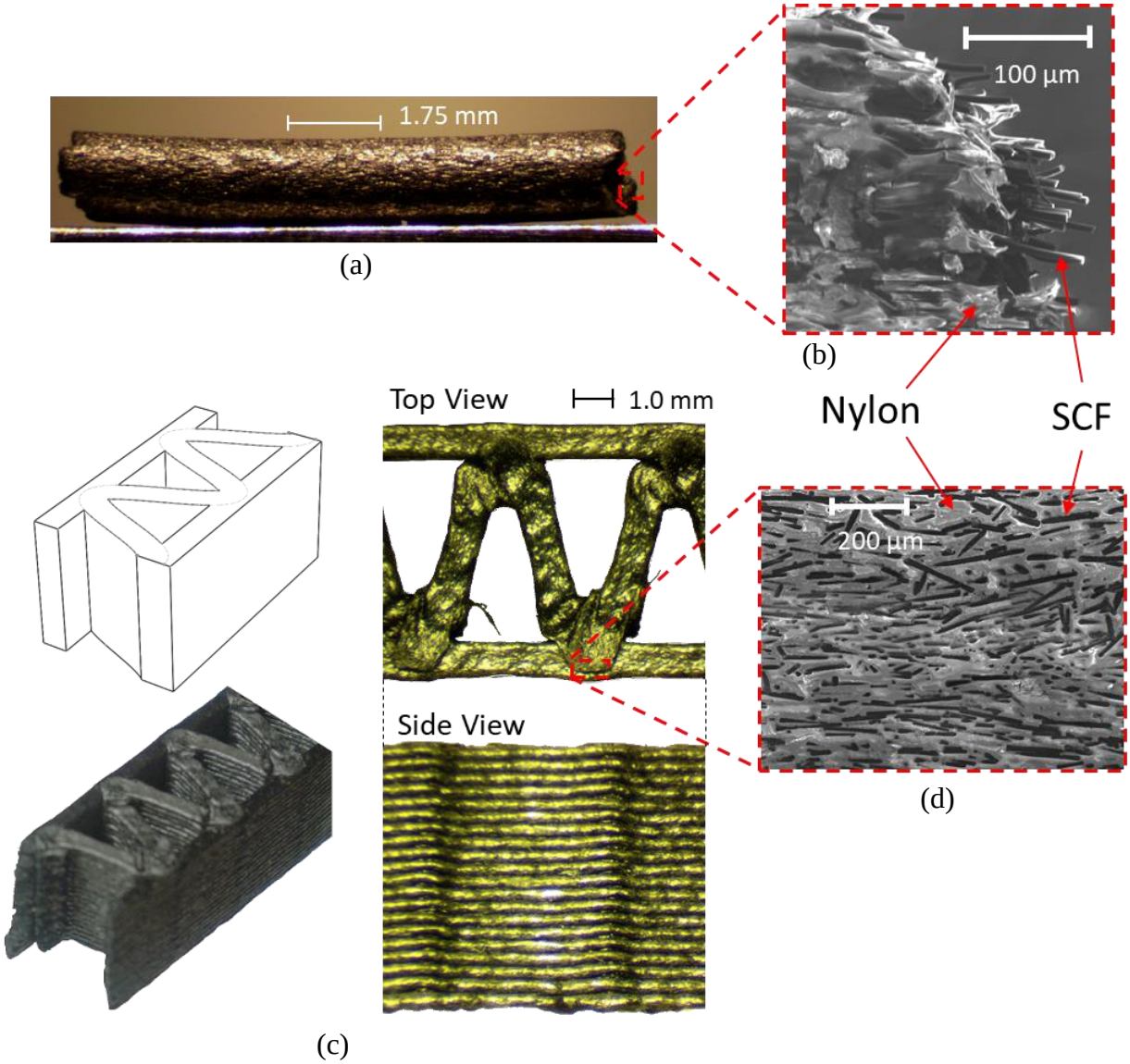

Figure 5.1. (a) A MEX Nylon SCF filament specimen that was examined with CT. (b) The end of the filament specimen was examined with SEM to visualize the protruding SCFs. (c) Perspective, top, and side views of MEX Nylon SCF specimen that was examined with CT. (d) The surface of the printed part was examined with SEM to visualize the embedded SCFs.

A MEX wave infill part, as shown in Figure 5.1(c), was fabricated on a MEX machine (Model 400mc by Stratasys) with the Nylon SCF filament. The MEX process parameters were: 0.5 mm layer height, 0.5 mm diameter nozzle orifice diameter, 295°C nozzle temperature, and 110°C oven temperature enclosing the whole part. A cube specimen with 3 mm edge length was

excised from the part for CT scanning. As shown in the SEM micrograph of the specimen surface in Figure 5.1(d), the part is composed of a Nylon-12 matrix with an irregular porous surface and with SCFs embedded inside the specimen. Using CT analysis, the volume percentage and distribution of pore, Nylon, and SCF within the MEX SCF part will be quantified.

5.3.2 CT Setup

In CT, an X-ray source focuses an X-ray beam within a rotating specimen. By measuring the X-ray attenuation with a detector plate while rotating the specimen, the regional density at unique three-dimensional locations, or voxels, of the part can be reconstructed. Each of the voxels, or 3D pixels, is assigned a grayscale unit, which represents the relative density of the voxel [44]. From the CT reconstruction, a 3D volume is generated [12], which can be used to create sets of 2D orthogonal images, e.g., Figure 5.2(a) and Figure 5.3. Each CT image is composed of voxels with grayscale intensity values, I, at a position (x, y) within the image, which are used for phase segmentation. As shown in Figure 5.4(a), the intensity $I(x, y)$ can be mapped to a measured histogram, $h_m(I)$, of the CT data.

A CT machine (Model Phoenix Nanotom® S by GE Measurement and Control, Billerica, MA) [13], was used in this study. Each specimen was scanned with a 70 kV tube voltage at 400 μA, and a 1000 ms exposure time. To achieve such high resolution, the rotating stage and specimen were positioned 5 mm from the X-ray tube. Three measurements were recorded and averaged for each position in the volume. The volume generated after CT was then converted to individual slice files.

5.3.3 CT Image Slicing and Histogram

The CT scan of the MEX SCF filament and part were taken at a 3D voxel resolution of 1.1 μm and 1.5 μm, respectively. Each voxel had a corresponding intensity represented by a 16-bit

grayscale intensity value between 0 to 65535. The filament specimen was reconstructed into 493 image slices (length of 0.54 mm and diameter of 1.78 mm), corresponding to a file size of 2.82 GB. As shown in Figure 5.2(a), the filament images were cropped to a diameter of 1.78 mm. The cropped image, as shown in Figure 5.2(b), was used for image analysis to identify and segment three phases: pore, Nylon, and SCF (Figure 5.2(c)).

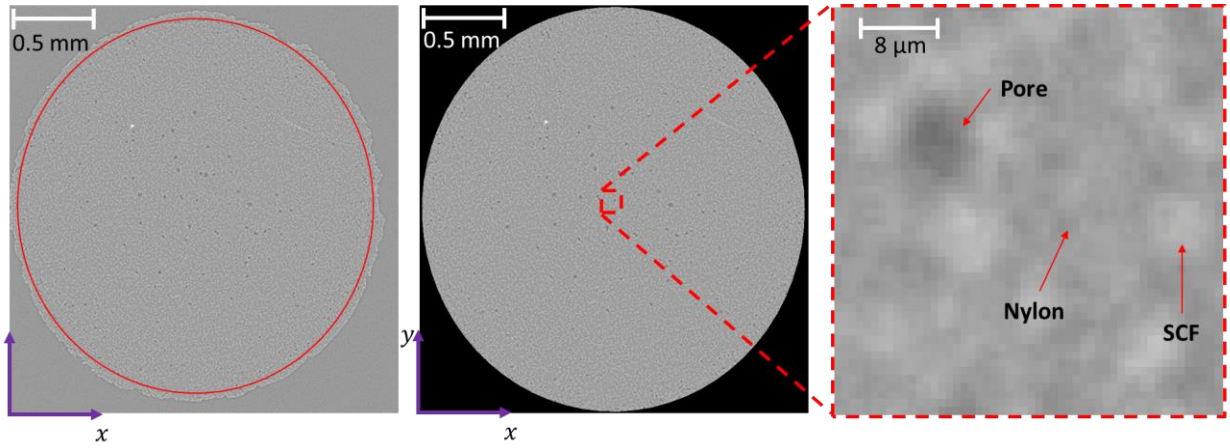

(a) (b) (c)

Figure 5.2. (a) CT image slices of the MEX SCF filament were circle cropped to remove the rough filament edges and non-filament volume. Analyses were performed on the (b) cropped image, which contains (c) three phases: pore, Nylon, and SCF.

The MEX SCF specimen was reconstructed into three orthogonal views (shown in Figure 5.3) – XY (top), XZ (front), and ZY (side) – with 1900 slices (2.8 x 2.8 x 4.5 mm), corresponding to a file size of 120 GB. Because of various artifacts in the CT data, the entire MEX SCF part was not analyzed. Six regions of interest (ROI), marked as A, B, and C in XY view, D in XZ view, and E and F in ZY view in Figure 5.3, were analyzed to identify and segment the pore, Nylon, and SCF phases.

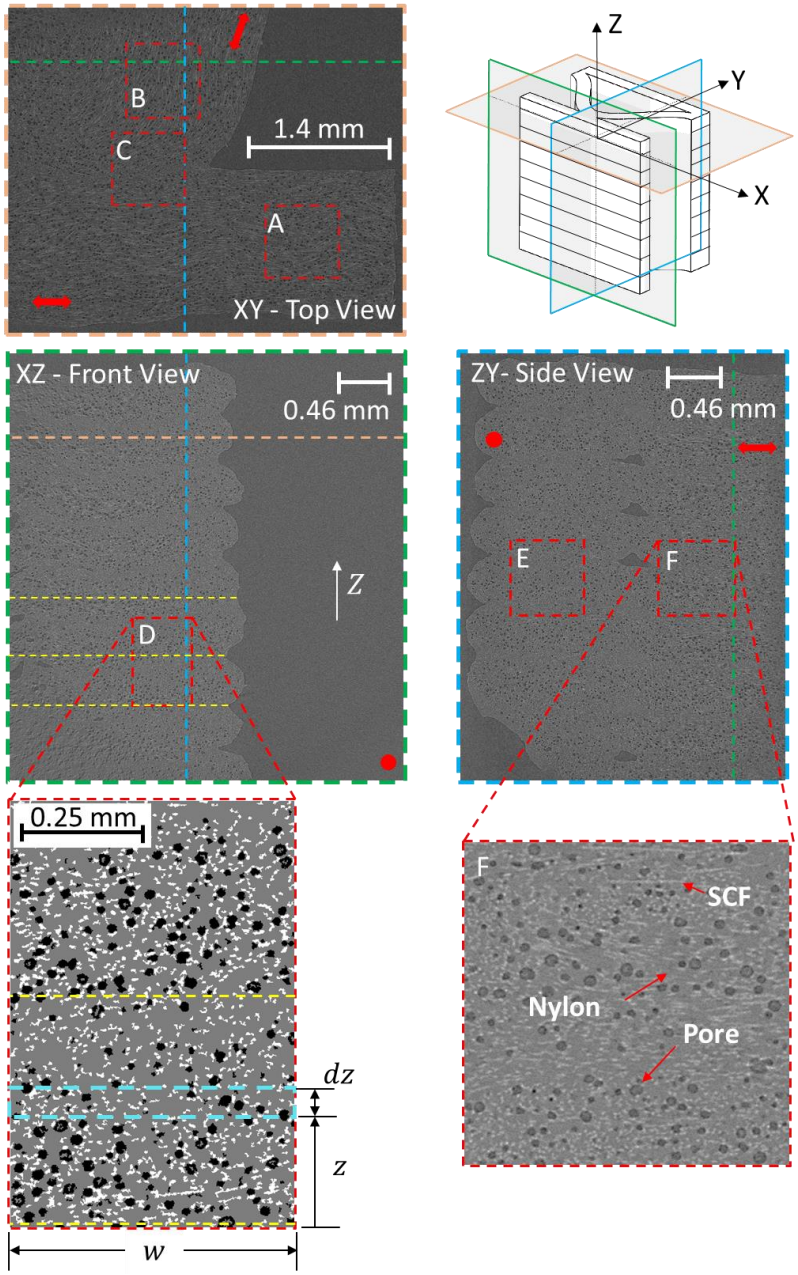

Figure 5.3. Top, front, and side cross-sectional views and isometric view of CT of MEX SCF part. Blue, orange, and green dotted lines and colors represent cross-sectional views of MEX layers and straight and curved sections. Red dotted boxes are ROIs that will be analyzed using MSGD. The XY view shows the intersection of a straight and curved raster with three ROIs: A – the straight raster, B – the curved raster, and C – the intersection zone. The XZ view shows the MEX layer stacking and the porosity distribution across the layer interface using ROI D with the porosity distribution determined in w x Δz areas along the Z-direction. The ZY view shows the side cross-section of the straight (ROI E) and curved (ROI F) regions.

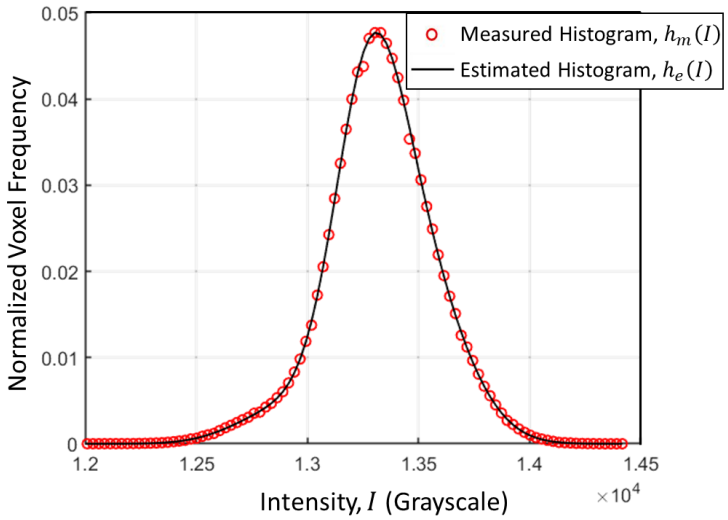

(a)

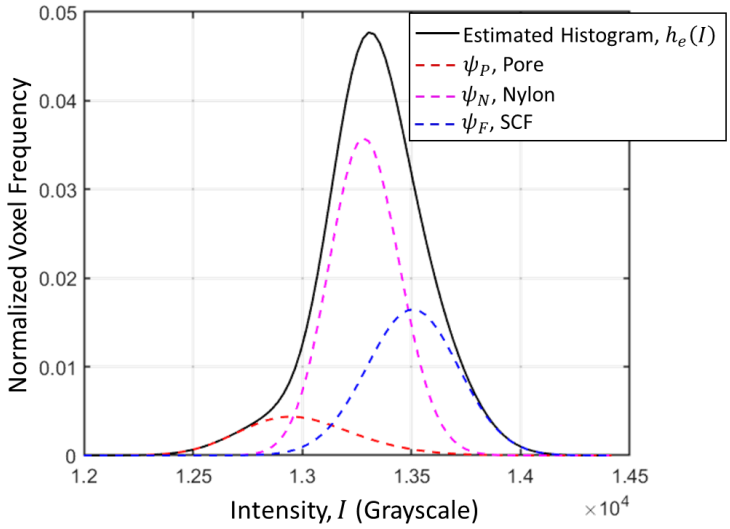

(b)

Figure 5.4. From the CT slice image of the MEX SCF part shown in Figure 5.3 (ROI A): (a) the measured normalized histogram, $h_m(I)$, of voxel intensity values in grayscale with the estimated histogram, $h_e(I)$, and (b) the MEX SCF part composed of three phases – pore, Nylon, and SCF – with three distinct modes. The three phase modes sum to the estimated histogram, $h_e(I)$.

From each CT image slice, a normalized histogram of voxel intensity frequencies in grayscale was generated by normalizing the frequency of voxel intensities to the total number of voxels. An example of the ROI A in the XY view of the MEX SCF specimen is illustrated in Figure 5.4, which shows the measured histogram $h_m(I)$ of the normalized voxel frequency vs.

voxel intensities I in grayscale in Figure 5.4(a) and three distinct modes of pore, Nylon, and SCF phases and their sum to the estimated histogram $h_e(I)$ in Figure 5.4(b).

5.3.4 MSGD Algorithm for Image Processing and Segmentation

Using the mixed skew Gaussian Distribution (MSGD) algorithm presented in [76], the measured histogram, $h_m(I)$, (Figure 5.4(a)) of the MEX SCF specimen can be decomposed into $n = 3$ modes: $\psi_1 = \psi_P$, $\psi_2 = \psi_N$, and $\psi_3 = \psi_F$, where $n = 1$ is the pore (P) phase, $n = 2$ is the Nylon (N) phase, and $n = 3$ is the SCF (F) phase, respectively (Figure 5.4(b)). These three phases sum to an estimated histogram, $h_e(I)$, which is fit to $h_m(I)$.

In the MSGD method [76], n skewed Gaussian distributions, ψ_i $(i = 1, \dots, n)$, are generated, that sum to $h_e(I)$ and with parameters (mean, standard deviation, and probability) inferred from $h_m(I)$ of the CT data. The PDF of the i^{th} skewed Gaussian phase mode ψ_i is:

$$\psi_i(I \mid \mu_i, \sigma_i, \alpha_i, P_i) = P_i \, f_i(I \mid \mu_i, \sigma_i, \alpha_i) = P_i \left(\frac{2}{\sqrt{2\pi\sigma_i^2}} e^{\frac{-(I-\mu_i)^2}{2{\sigma_i}^2}} \int_{-\infty}^{\alpha_i(\frac{I-\mu_i}{\sigma_i})} \frac{1}{\sqrt{2\pi}} e^{-\frac{t^2}{2}} dt \right) \quad (5.1)$$

$$\int_{-\infty}^{\infty} f_i(I \mid \mu_i, \sigma_i, \alpha_i) \; dI = 1 \quad (5.2)$$

$$\sum_{i=1}^{n} P_i = 1 \quad (5.3)$$

where $f_i(I \mid \mu_i, \sigma_i, \alpha_i)$ is the standard form of a skewed Gaussian distribution, μ_i is the mean of the i^{th} phase, σ_i is the standard deviation of the i^{th} phase, α_i is the skewness parameter of the i^{th} phase, and P_i is the probability of the i^{th} phase. The phase modes, ψ_i, are arranged according to the magnitude of their mean value, i.e., $\mu_1 < \cdots < \mu_i < \cdots < \mu_n$. With a vector parameter, $\boldsymbol{\omega_i} = [\mu_i, \sigma_i, \alpha_i, P_i]^T$, least-squared fitting is performed to minimize the error between $h_m(I)$ and $h_e(I|\boldsymbol{\omega})$:

$$\epsilon(I|\boldsymbol{\omega}) = |h_m(I) - h_e(I|\boldsymbol{\omega})| \tag{5.4}$$

where $|\bullet|$ is the Euclidean norm (i.e. $\sqrt{\epsilon_1^2 + \cdots + \epsilon_p^2}$). The vector parameters, $\hat{\boldsymbol{\omega}}$**,** that minimize the least-squares fitting error, $\epsilon(I|\boldsymbol{\omega})$, (i.e. the argmin function) are:

$$\hat{\boldsymbol{\omega}} = \underset{\boldsymbol{\omega}}{\operatorname{argmin}}(\epsilon(I|\boldsymbol{\omega})) \tag{5.5}$$

which is subject to the constraints:

$$\eta_i : \quad C_i^l \leq \mu_i \leq C_i^u \tag{5.6}$$

$$\gamma_i : \quad \sum_{i=1}^{n} P_i = 1 \tag{5.7}$$

where η_i is the lower and upper bound constraint on the mean μ_i; C_i^l and C_i^u are the lower and upper bound, respectively, that encompass the i^{th} phase peak intensity value on the histogram; γ_i is the equality constraint on the sum of the phase probabilities, P_i. To guide the optimization of Eq. (5.5), the lower and upper intensity bounds (C_i^l and C_i^u) indicate a region of intensity values where the phase mean μ_i is expected to be located. These bounds are provided based on examination of the i^{th} phase intensity values $I(x, y)$ from the CT data.

For analysis and visualization of the CT image, the CT data is thresholded, which is the process of determining the intensity regions on the measured histogram that are associated with a phase [69]. The CT data with grayscale intensity values $I(x, y)$ is simplified to a thresholded image, $T(x, y)$:

$$T(x, y) = B_i \; \forall \; I(x, y) \in \; \Re_i \tag{5.8}$$

where $\Re_i$, is the grayscale intensity region for ψ_i:

$$\Re_i \in (L_{i-1}, L_i \,] \tag{5.9}$$

and L_i is the threshold limit found using a Bayesian Decision Rule (BDR):

$$L_i = \frac{\mu_{i-1}\,\sigma_i^2 - \mu_i\,\sigma_{i-1}^2}{\sigma_i^2 - \sigma_{i-1}^2} + \frac{\sigma_{i-1}\,\sigma_i}{\sigma_i^2 - \sigma_{i-1}^2}\left((\sigma_i^2 - \sigma_{i-1}^2)\log\left(\frac{\sigma_i^2}{\sigma_{i-1}^2}\right) + 2(\sigma_{i-1}^2 - \sigma_i^2)\log\left(\frac{P_i}{P_{i-1}}\right) + (\mu_{i-1} - \mu_i)^2 \right)^{\frac{1}{2}} \tag{5.10}$$

For example, within a CT data histogram (Figure 4.4(a)) corresponding to the MEX SCF part (Figure 4.4(b)), BDR yields three regions, $\Re_1 = \Re_P$, $\Re_2 = \Re_N$, and $\Re_3 = \Re_F$, for the pore, Nylon, and SCF phases, respectively:

$$\Re_P \in [\min(I), L_P] \tag{5.11}$$

$$\Re_N \in (L_P, L_N] \tag{5.12}$$

$$\Re_F \in (L_N, \max(I)] \tag{5.13}$$

where L_P is the intensity limit between ψ_P and ψ_N and L_N is the intensity limit between ψ_N and ψ_F. The thresholded image, $T(x, y)$, is then:

$$T(x,y) = \begin{cases} B_P \;\forall\, I(x,y) \in \Re_P \\ B_N \;\forall\, I(x,y) \in \Re_N \\ B_F \;\forall\, I(x,y) \in \Re_F \end{cases} \tag{5.14}$$

where B_P, B_N, and B_F are unique intensity values assigned to the pore, Nylon, and SCF phase regions, respectively, as shown in Figure 4.4(c). The resulting thresholded image, $T(x, y)$, is shown in Figure 4.4(d).

5.3.5 Pore Volume, Distribution, and Spatial Density in the MEX SCF Filament

The volume, distribution, and spatial density of pores within MEX SCF filaments and parts is important to the strength and durability of MEX parts. By quantifying the porosity within these specimens, process parameters for fabrication of filaments and MEX of parts may be optimized to reduce porosity.

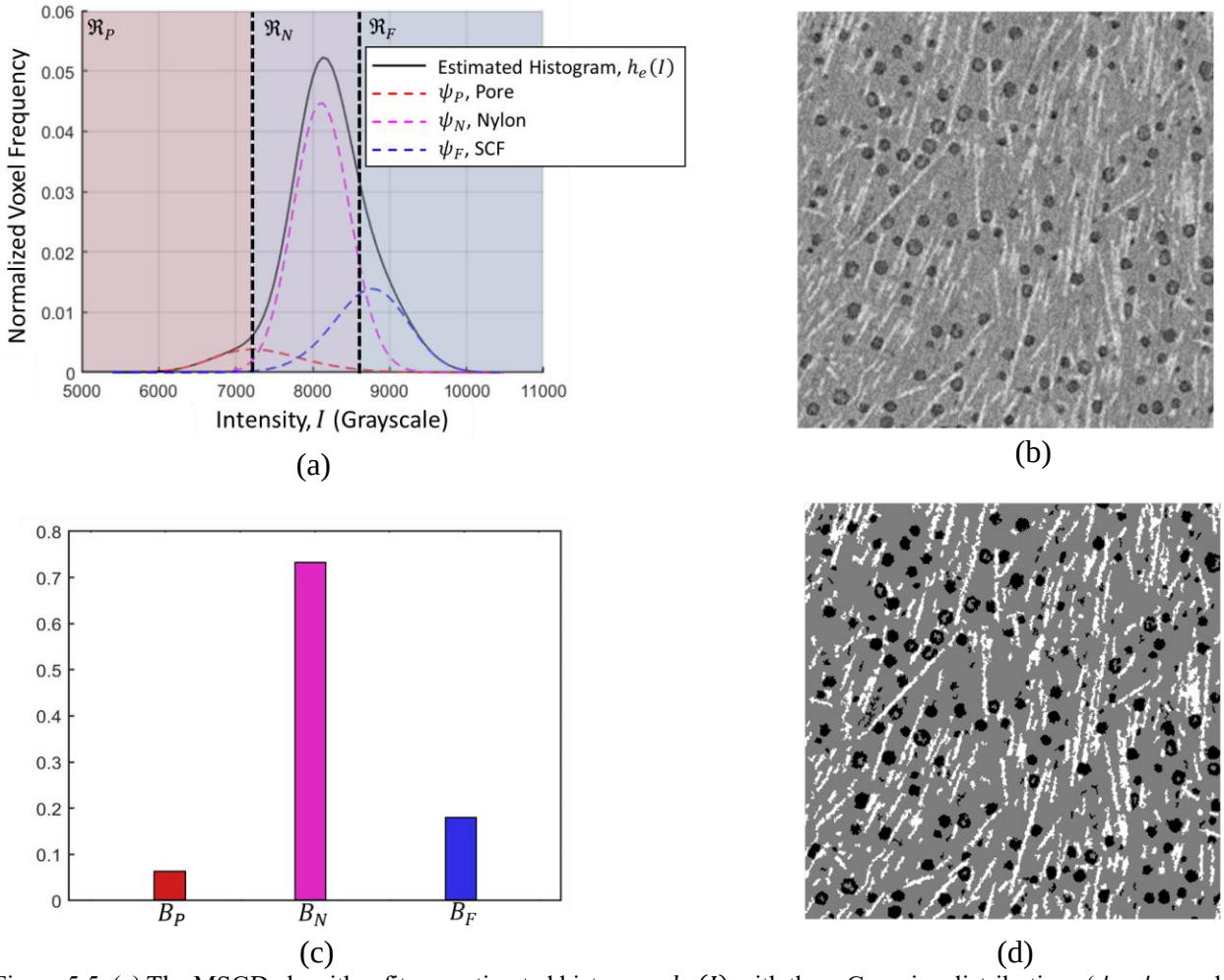

Figure 5.5. (a) The MSGD algorithm fits an estimated histogram $h_e(I)$ with three Gaussian distributions (ψ_P, ψ_N, and ψ_F) representing the pore, Nylon, and SCF, respectively, to the (b) measured CT data. BDR is used to generate regions $\Re_P$, $\Re_N$, and $\Re_F$ corresponding to the intensity values associated with the pore, Nylon, and SCF phases, respectively. (c) Unique intensity values, B_P, B_N, and B_F, are assigned to the intensity regions $\Re_P$, $\Re_N$, and $\Re_F$, respectively. With this process, the CT data with intensities $I(x, y)$ is converted into the (d) thresholded image $T(x, y)$.

To quantify the distribution, spatial density, and size of pores, 3D connected pores $P_C(x, y)$ at position (x, y) in the CT image are identified from the thresholded and filtered CT data $T(x, y)$. From the full set of thresholded MEX SCF filament CT images, connected 3D pores, $P_C(x, y)$,

with a common edge or corner were defined as connected pores. To find these connected pores, Matlab equation *bwconncomps* was used. The volume, V_P, of these connected pores is:

$$V_P = V_V \, N_P \tag{5.15}$$

where N_P is the total number of voxels per pore and V_V is the voxel resolution.

During filament fabrication, extrusion of the plastic causes the outside of the filament to cool before the inside inducing voids radially through the filament. To quantify this effect, the radial distribution of the connected pores, $P_C(x, y)$, within the MEX SCF filament was analyzed. The total number and average volume of connected pores within a differential radial ring, with length L, width Δr, and radius r (as shown in Figure 5.6) of the cylindrical filament were summed and normalized by the total volume $2\pi r \Delta r L$ of the specimen. In this study, Δr = 0.05 mm and L = 0.5 mm.

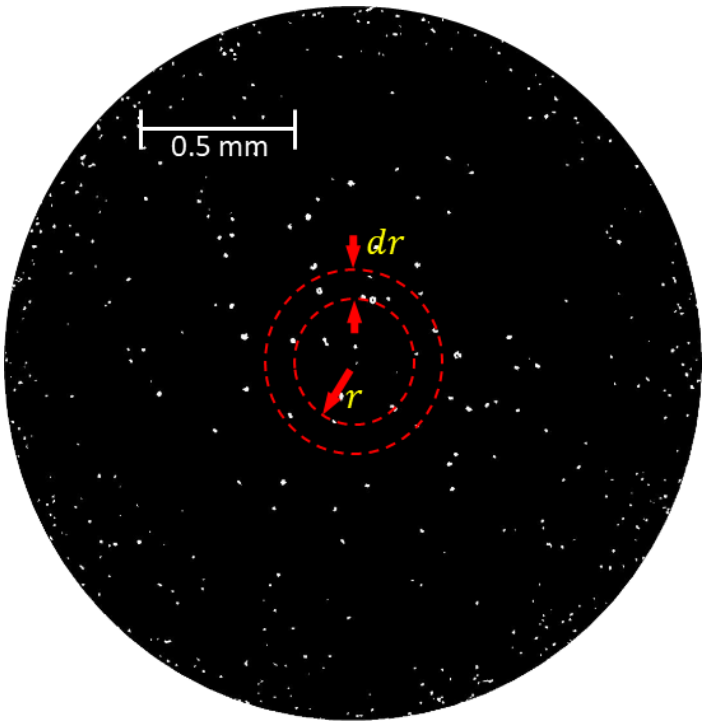

Figure 5.6. Pores (white) shown within the thresholded image for porosity distribution analysis. Pore volume and density were analyzed along differential rings with radius r, width Δr, and filament length L.

5.3.6 Pore Volume, Distribution, and Spatial Density in the MEX SCF Specimen

An isometric view of the reconstructed CT of the MEX SCF part along with three orthogonal views (XY top, XZ front, and ZY side) are shown in Figure 5.3. In the top XY cross-sectional view, a curved and straight segment of the MEX extrudate are shown intersecting. The front (XZ) and side (ZY) cross-sectional views show the layer stacking in the MEX process, as indicated by the radii at the edges of the part.

Figure 5.3 shows each of the ROIs chosen for analysis and thresholding. The XY (top view) plane in Figure 5.3 has three ROIs identified with the direction of the toolhead travel indicated by an arrow: A – the straight raster, B – the curved raster, and C – the intersection zone. ROI C is the intersection of these straight and curved MEX rasters. In the front XZ view, ROI D is the cross-section of the curved MEX extrudate, as can be seen from the top XY view. The toolhead travel direction for this cross-section is normal to the image. Finally, the side ZY view shows the cross-section of the intersection of the straight, ROI E, and curved, ROI F, MEX extrudate. In ROI E, toolhead travel is normal to the image, and in ROI F, toolhead travel is transverse to the image.

The porosity distribution was analyzed in and at the intersection between MEX layers. Because only single CT slices were analyzed for the MEX SCF part, only two-dimensional area analyses were performed. Based on the single thresholded CT data, Matlab equation *bwconncomps* was used to find the connected pores and to calculate their area. The pore frequency and area were measured for each ROI. Within the ROI D, the porosity was measured within a differential area of width w and thickness Δz along the z-direction. In this study, w = 0.6 mm and Δz = 38 μm. The MEX layer thickness (distance between two adjacent yellow lines) was 0.46 mm.

5.4 Results of MSGD Segmentation of the MEX SCF Filament CT Data

In this section, results of the MSGD algorithm [76] and porosity analysis of the CT of the MEX SCF filament are presented.

5.4.1 Optimization Setup of MSGD Algorithm for the MEX SCF Filament

A CT image with intensities, $I(x, y)$, of the MEX SCF filament with pore, Nylon, and SCF phases is shown in Figure 5.7(a). The associated measured histogram, $h_m(I)$, is shown in Figure 5.8(a). Pore (P) with Gaussian mode $\psi_P(I|\boldsymbol{\omega_P})$, Nylon ($N$) with Gaussian mode $\psi_N(I|\boldsymbol{\omega_N})$, and SCF ($F$) with Gaussian mode $\psi_F(I|\boldsymbol{\omega_F})$ were the three phases (i.e. $n = 3$) present in the MEX SCF filament. To fit $h_m(I)$, an estimated histogram, $h_e(I|\hat{\boldsymbol{\omega}})$ was fit according to Eq. (5.5) where $\hat{\boldsymbol{\omega}} = [\hat{\boldsymbol{\omega}}_{\boldsymbol{P}}, \hat{\boldsymbol{\omega}}_{\boldsymbol{N}}, \hat{\boldsymbol{\omega}}_{\boldsymbol{F}}]$ were the optimized vector parameters for the pore, Nylon, and SCF phases. To guide the optimization of Eq. (5.5), three intensity regions, C_P^l and C_P^u for the pore phase mean μ_P, C_N^l and C_N^u for the Nylon phase mean μ_N, and, C_F^l and C_F^u for the SCF phase mean μ_F, were defined based on the examination of the phase intensity values $I(x, y)$ from Figure 5.7(b) and $h_m(I)$ in Figure 5.8(a). Figure 5.8(a) shows upper and lower bound intensity regions, C_P^l, C_P^u, C_N^l, C_N^u, C_F^l and C_F^u, that were provided for Eq. (5.6) constraints. Table 5.1 shows the initial conditions for all $\boldsymbol{\omega}$ parameters.

The estimated histogram, $h_e(I|\hat{\boldsymbol{\omega}})$, and the Gaussian modes $\psi_P(I|\boldsymbol{\omega_P})$, $\psi_N(I|\boldsymbol{\omega_N})$, and $\psi_F(I|\boldsymbol{\omega_F})$ for the pore, Nylon, and SCF phases, respectively, are shown in Figure 5.8(b) corresponding to the CT data of Figure 5.7(a). BDR was performed on the Gaussian modes to define three intensity regions, $\Re_P$, $\Re_N$, and $\Re_F$, for the pore, Nylon, and SCF phases, respectively. From these phase regions, the thresholded image, $T(x, y)$, shown in Figure 5.9(a), was generated. Comparing a region of the thresholded image in Figure 5.9(b) to the same region in the original CT data (Figure 5.9(c)), boundaries between the pore, Nylon, and SCF can be distinguished.

Because the SCF were oriented axially along the filament length, the SCF are white circles with approximately 8 μm diameter. From the resolving power of the CT machine, the minimum allowable feature size was 3.3 μm^3. Because of the low resolution compared with the small features, the circles representing the SCF are often jagged and not perfectly rounded, as seen in Figure 5.9(b).

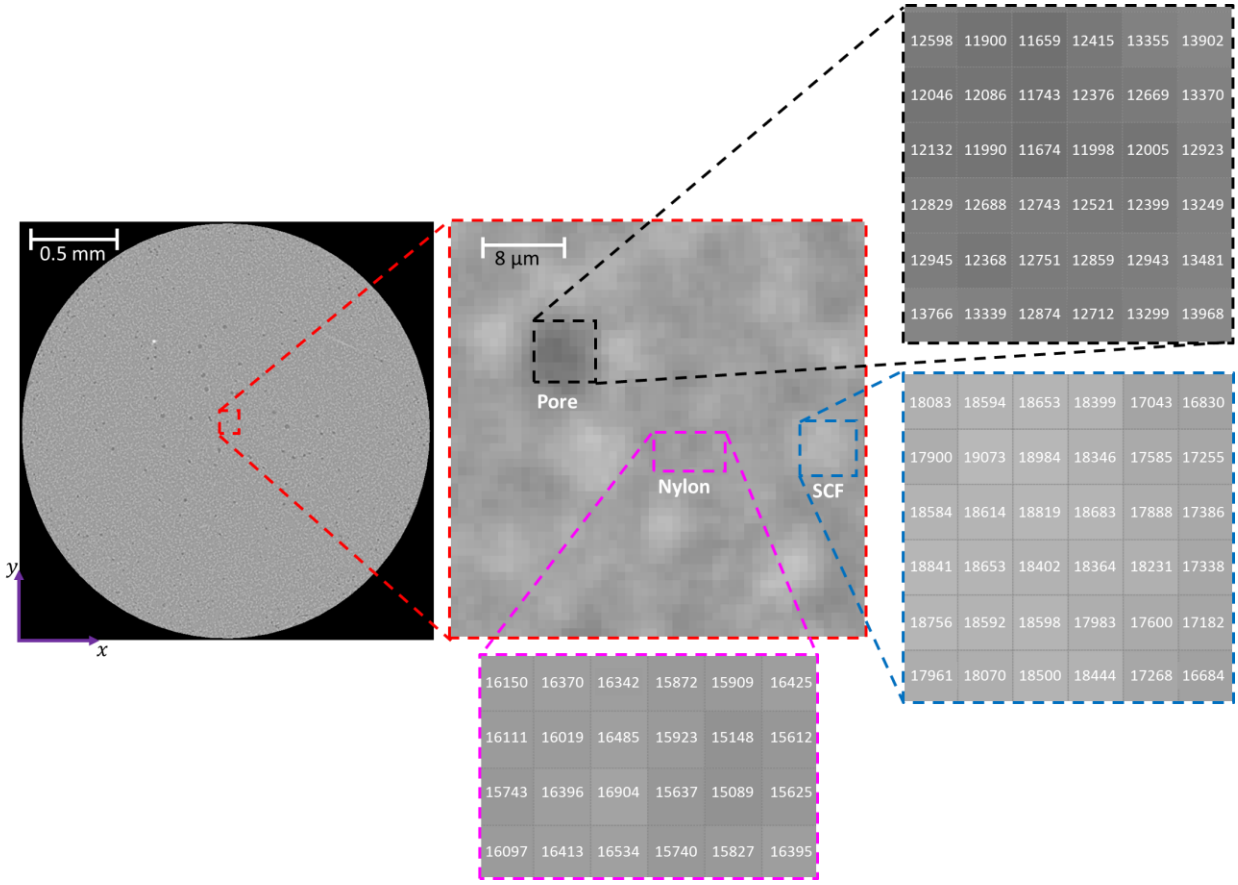

(a) (b)

Figure 5.7. (a) A CT image of the MEX SCF filament, which is composed of (b) pore, Nylon, and SCF phases.

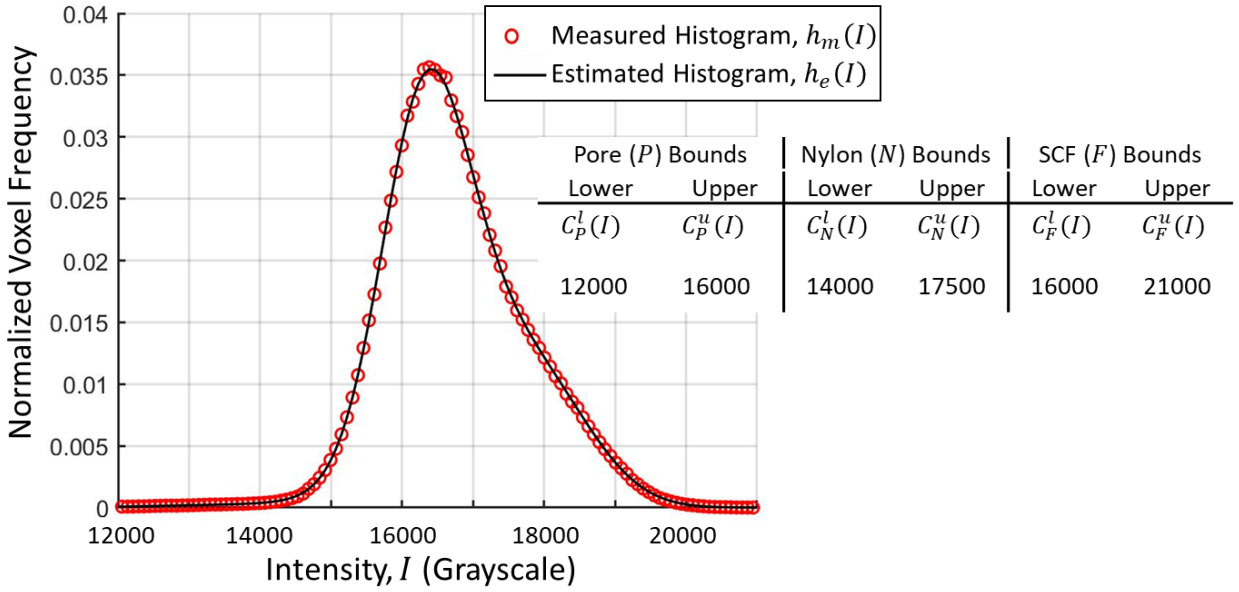

Pore (P) Bounds		Nylon (N) Bounds		SCF (F) Bounds	
Lower	Upper	Lower	Upper	Lower	Upper
$C_P^l(I)$	$C_P^u(I)$	$C_N^l(I)$	$C_N^u(I)$	$C_F^l(I)$	$C_F^u(I)$
12000	16000	14000	17500	16000	21000

(a)

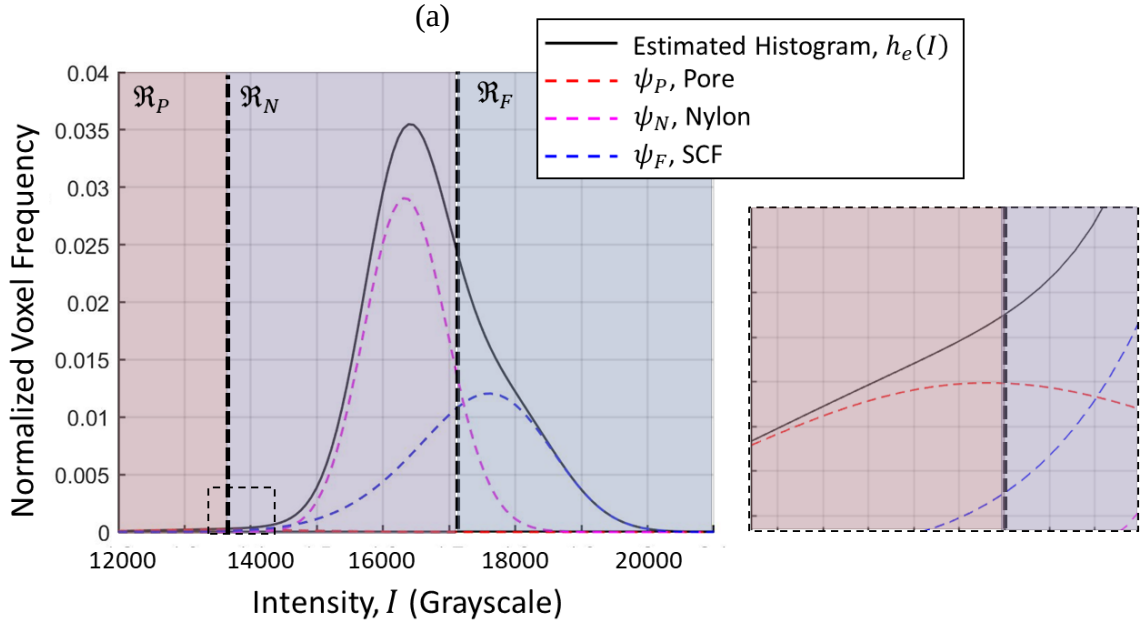

(b)

Figure 5.8. (a) The measured normalized histogram, $h_m(I)$, of voxel intensity values in grayscale and estimated histogram, $h_e(I|\hat{\boldsymbol{\omega}})$, of the MEX SCF filament CT image shown in Figure 5.7 and (b) three phases – pore, Nylon, and SCF – with three Gaussian modes, ψ_P, ψ_N, and ψ_F. The Gaussian modes sum to the estimated histogram, $h_e(I|\hat{\boldsymbol{\omega}})$. Using BDR, $h_e(I|\hat{\boldsymbol{\omega}})$ is thresholded into three intensity regions, $\Re_P$, $\Re_N$, and $\Re_F$, for pore, Nylon, and SCF phases, respectively.

Table 5.1. MSGD algorithm initial conditions and optimized parameters for the MEX SCF filament CT image slice shown in Figure 5.7(a). The fitted parameters, $\hat{\boldsymbol{\omega}}$, generate the estimated histogram, $h_e(I)$ of Figure 5.8(b).

	Phase	$\mu_i(I)$, Phase Mean	$\sigma_i(I)$, Phase Standard Deviation	P_i, Phase Volume Percentage (%)	α_i, Phase Skew
Initial Conditions, $\boldsymbol{\omega}$	Pore, $\psi_P(I\|\boldsymbol{\omega_P})$	12000	700	5.0	0.0
	Nylon, $\psi_N(I\|\boldsymbol{\omega}_N)$	16000	700	60.0	0.0
	SCF, $\psi_F(I\|\boldsymbol{\omega_F})$	19000	700	35.0	0.0
Optimized Parameters, $\hat{\boldsymbol{\omega}}$	Pore, $\psi_P(I\|\hat{\boldsymbol{\omega}}_{\boldsymbol{P}})$	12730	1551.5	0.79	1.2
	Nylon, $\psi_N(I\|\hat{\boldsymbol{\omega}}_{\boldsymbol{N}})$	15990	730.9	59.2	0.8
	SCF, $\psi_F(I\|\hat{\boldsymbol{\omega}}_{\boldsymbol{F}})$	18390	1452.3	40.0	-1.7

5.4.2 Results from MSGD Algorithm for the MEX SCF Filament

Using the MSGD algorithm of Sec. 5.3.4, all 493 MEX SCF filament CT images were analyzed. For the individual CT image of Figure 5.7, the optimized parameters, $\hat{\boldsymbol{\omega}}$, for estimated histogram $h_e(I)$ of the CT data of Figure 5.8(a) are shown in Table 5.1. Table 5.2 shows the average of each optimized parameter over the length of the filament. From Table 5.2, the mean grayscale intensity values of the pore μ_P, Nylon μ_N, and SCF μ_F, were 13320, 16240, and 18330, respectively. These mean grayscale intensity values are within the range of intensity values seen in Figure 5.7(b) for each of the phases. The standard deviations for the pore σ_P, Nylon σ_N, and SCF σ_F, were 2385, 667, and 1247, respectively. As shown in Figure 5.8(b), the standard deviation of the Nylon was small compared to the standard deviation of the SCF and pore phases. The standard deviations of the pore and SCF phases were broader indicating a wider range of grayscale values associated with the phase and less certainty of the measurement. The skew parameters for the pore α_P, Nylon α_N, and SCF α_F, were 0.9, 0.1, and –1.3, respectively. Because the magnitude of skew parameters is small, it is expected that most intensity values for each phase fall close to their respective mean value. Finally, the volume percentage of the pore P_P, Nylon P_N, and SCF

P_F, phases were 1.6%, 62.2%, and 36.2%, respectively. Using a density of Nylon and SCF of 1.15 g/cm^3 and 1.55 g/cm^3, respectively, the estimated SCF weight percentage was estimated to be 47%, which is within 10% of the 35 wt% of SCF provided by the manufacturer.

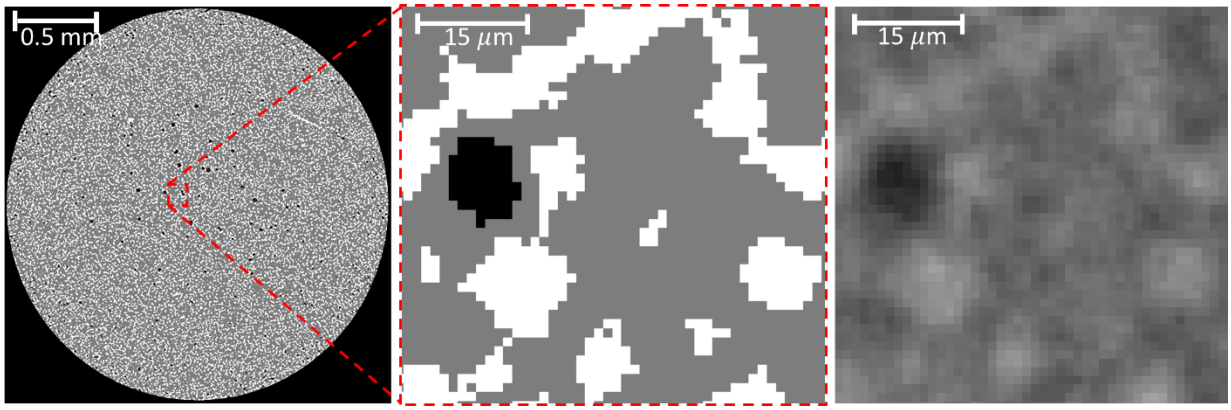

(a) (b) (c)

Figure 5.9. (a) Thresholded image, $T(x, y)$, corresponding to the MEX SCF filament CT image slice shown in Figure 5.7(a) and the phase threshold regions, $\Re_P$, $\Re_N$, and $\Re_F$, shown in Figure 5.8(b). Black, gray, and white correspond to pore, Nylon and SCF, respectively. Comparing the thresholded region of (b) to the original CT image (c), the pore, Nylon, and SCF phase are appropriately identified. Note that SCFs appear circular in shape because their axes are perpendicular to the CT image plane.

Figure 5.10 shows the volume percentages of the pore, Nylon, and SCF phases across the 0.5 mm segment length (L) of the MEX SCF filament. Small variations (i.e. +/- 10% for each phase) in each of the phase volume percentages were measured. These small variations were due to multiple local minima (no unique solution) present in the MSGD fitting of $h_e(I)$ to $h_m(I)$. These local minima occur because there are small differences in density of the internal phases that result in a lack of contrast between phase histograms. To identify these minima, several initial conditions, as listed in Table 5.3, were tested. Across the various initial conditions, solutions for volume percentages of pore, Nylon, and SCF from each tested initial condition were found to be within a standard deviation range of 0.11%, 0.26%, and 0.36%, respectively. Although these volume percentage estimates are similar, such variations indicate the possibility of multiple solutions. Furthermore, the number of solutions depends on the range of intensity regions, C_P, C_N,

and C_F. Increasing these ranges will increase the solution space or provide no solution, ultimately reducing the reliability of the algorithm.

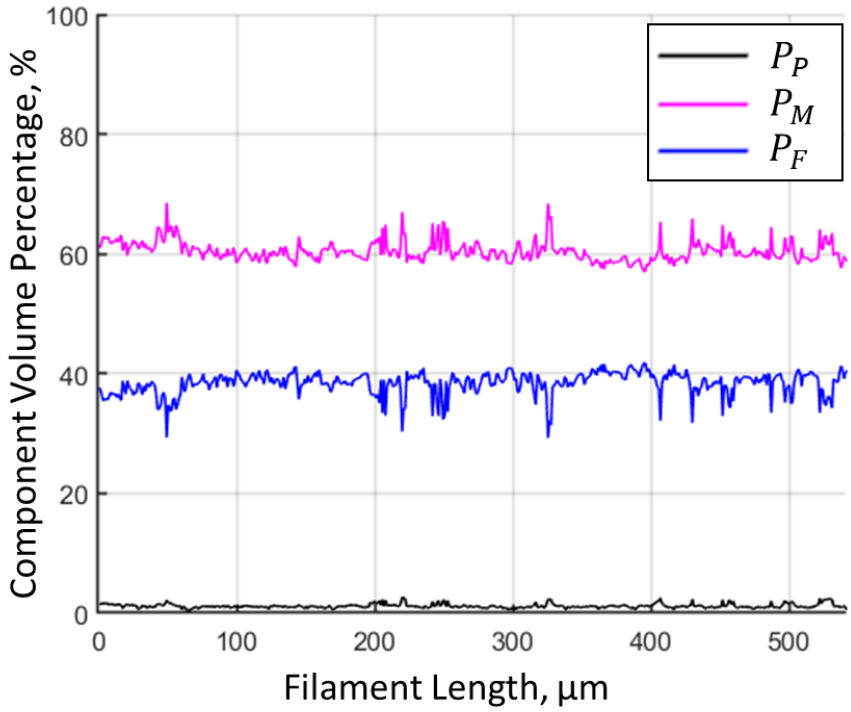

Figure 5.10. Volume percentage of pore, Nylon, and SCF across the length of the filament.

Table 5.2. Average of optimized parameters across the length of the filament.

Pore				Nylon				SCF			
$\mu_P(I)$	$\sigma_P(I)$	$P_P(\%)$	α_P	$\mu_N(I)$	$\sigma_N(I)$	$P_N(\%)$	α_N	$\mu_F(I)$	$\sigma_F(I)$	$P_F(\%)$	α_F
13320	2384.7	1.6	0.9	16240	667.4	62.2	0.1	18330	1247.0	36.2	-1.3

Table 5.3. Initial conditions tested to identify local minimum solutions.

Initial Conditions, $\boldsymbol{\omega_i} = [\mu_i(I), \sigma_i(I), P_i(\%), \alpha_i]$												Optimized P_i, $\widehat{\boldsymbol{\omega}}_{\boldsymbol{i}}$, (%)		
Pore, $i = P$				Nylon, $i = N$				SCF, $i = F$				P_P	P_N	P_F
12000	700	0.2	0.0	16000	700	0.3	0.0	19000	700	0.5	0.0	2.2	65.7	32.2
14000	700	0.2	0.0	17000	700	0.4	0.0	20000	700	0.4	0.0	1.9	65.3	32.7
12000	500	0.2	0.0	16000	1000	0.4	0.0	19000	500	0.4	0.0	2.1	66.0	31.7
12000	700	0.2	0.0	16000	700	0.3	0.0	19000	700	0.5	0.0	2.1	65.8	32.1
12000	700	0.2	3.0	16000	700	0.4	3.0	19000	700	0.4	3.0	2.0	65.6	32.3

5.4.3 Results from Porosity Analysis of MEX SCF Filament

Using Eq. (5.15), the volume of pores in the MEX SCF filament were calculated. Figure 5.11 shows the frequency of pores versus pore volume, V_P. From Figure 5.11(a), the mean pore volume was 50 μm^3 with 92% of pores having a volume less than 100 μm^3. Higher volume pores, which occurred less frequently throughout the part, are shown in the exploded view of the number of pores versus pore volume of Figure 5.11(b). The largest pore volume in the filament was 400 μm^3.

The radial distribution of the pores in the filament were measured according to the method in Sec. 5.3.5. Results of pore density and percentage of pore per unit volume vs. r/a, where a is the radius of the filament, are shown in Figure 5.12 and Figure 5.13, respectively. The number of pores within radial rings along the radius of the filament were counted and divided by the volume of the radial ring with Δr = 0.05 mm (20 rings in total) and $L = 0.5$ mm. The highest density of pores was located near the outside ($r/a = 1$) of the filament, as shown in Figure 5.12.

Results of the percentage of pore per unit volume within radial rings (with Δr = 0.05 mm) along the radius are shown in Figure 5.13. The large size pores near the center of the filament ($r/a = 0$) dominate the pore volume ratio. One explanation for this finding is that the filament extrusion process may cause large bubbles to be trapped in the center of filament and small bubbles to form during the post-extrusion cooling of thermoplastic material around the periphery of the filament. Another explanation could be due to uneven thermal shrinkage during the cooling process. Because the exterior of the filament cools before the interior, the filament periphery contracts causing internal thermal stresses to be generated that may cause expansion of the voids at the center of the filament.

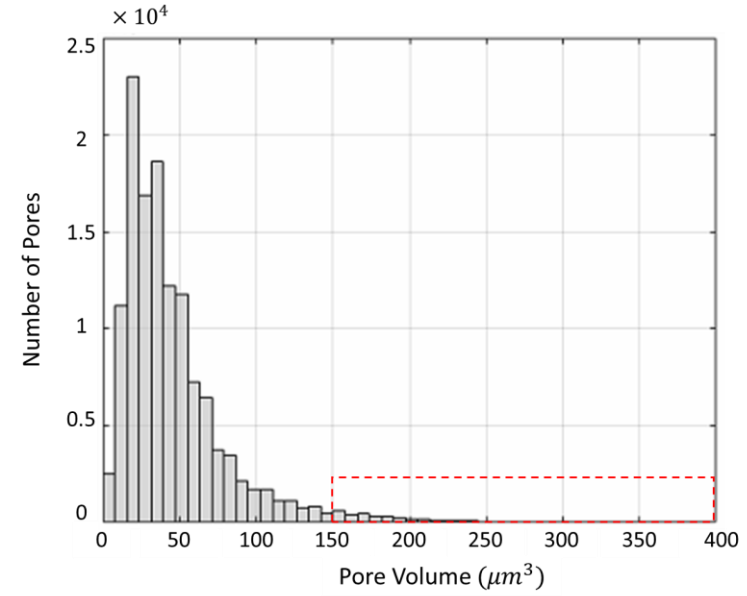

(a)

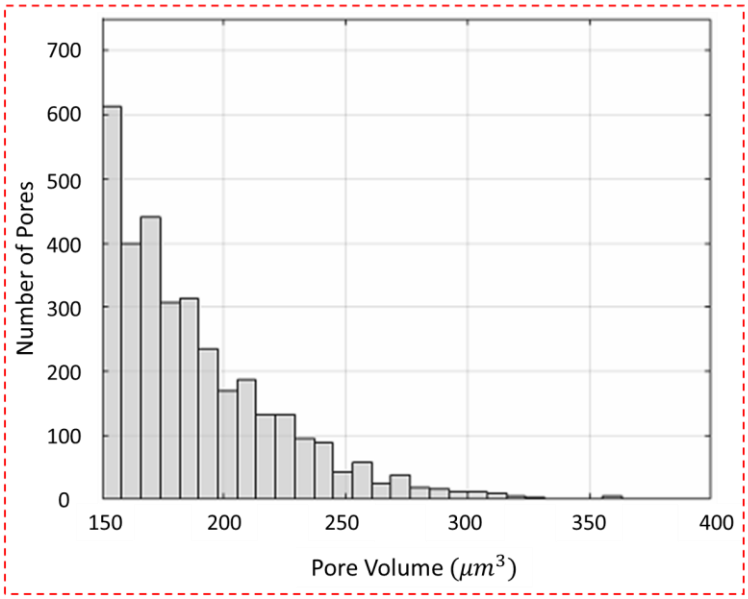

(b)

Figure 5.11. (a) Number of pores versus pore volume with most pores smaller than 100 μm^3 and (b) the number of pores versus pore volume for pores larger than 150 μm^3.

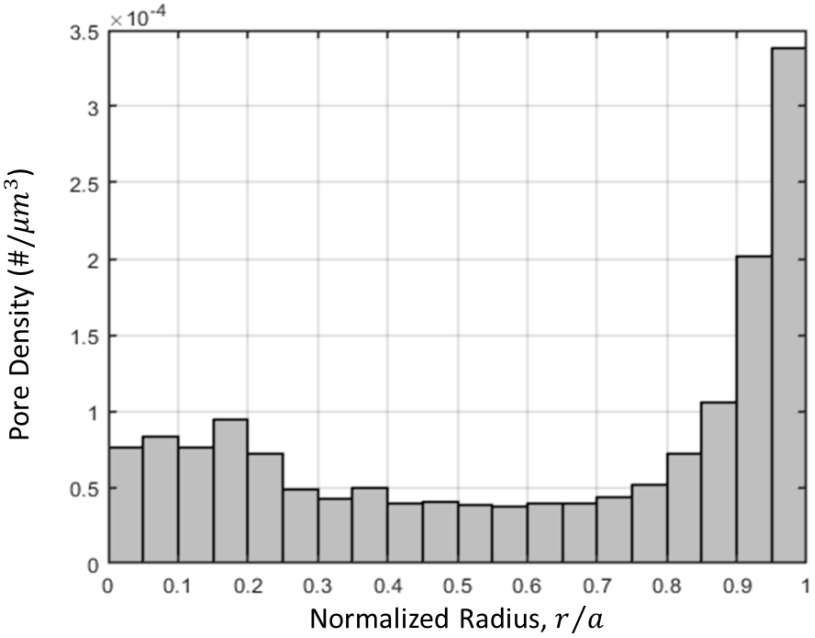

Figure 5.12. Pore density along the radius of the filament. A higher number of pores was found at larger radii ($r/a > 0.9$).

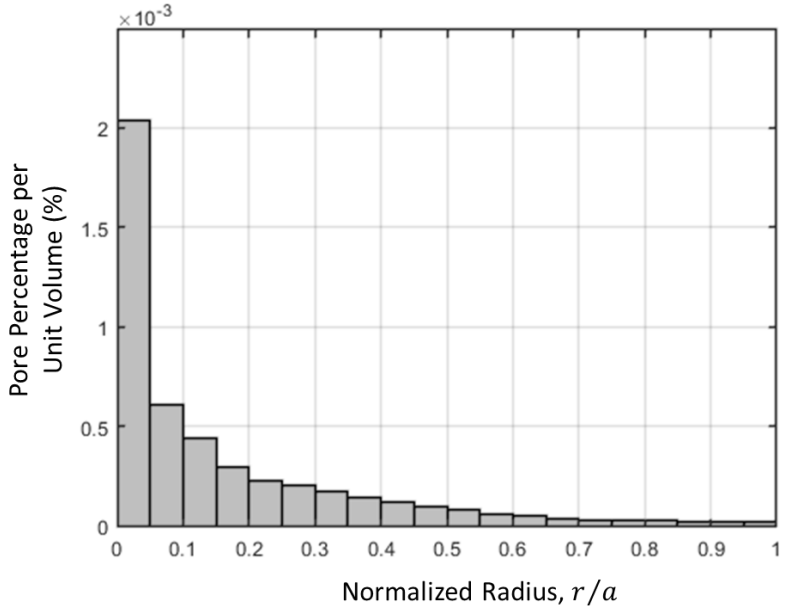

Figure 5.13. Pore percentage per unit volume along the radius of the filament. Larger volume pores occur closer to the center ($r/a = 0$) of the filament.

5.5 MEX SCF Part CT Analysis Results

In this section, results of the segmentation algorithm and analysis of the CT scanned MEX SCF part are presented.

5.5.1 Optimization Setup of MSGD Algorithm for the MEX SCF Part

Each MEX SCF part ROI indicated in Figure 5.3 was analyzed individually as an image with intensities, $I(x,y)$, according to Secs. 5.3.2-5.3.4. For each of these ROIs, the measured histogram of intensity values, $h_m(I)$, did not change significantly. Therefore, only one of the processed histograms – the ROI A in Figure 5.3 – is shown in Figure 5.14(a). The pore (P) with Gaussian mode $\psi_P(I|\boldsymbol{\omega_P})$, Nylon ($N$) with Gaussian mode $\psi_N(I|\boldsymbol{\omega_N})$, and SCF ($F$) with Gaussian mode $\psi_F(I|\boldsymbol{\omega_F})$ were three phases (i.e. $n = 3$) present in the MEX SCF part. To fit $h_m(I)$, an estimated histogram, $h_e(I|\widehat{\boldsymbol{\omega}})$ was fit according to Eq. (5.5) where $\widehat{\boldsymbol{\omega}} = [\widehat{\boldsymbol{\omega}}_{\boldsymbol{P}}, \widehat{\boldsymbol{\omega}}_{\boldsymbol{N}}, \widehat{\boldsymbol{\omega}}_{\boldsymbol{F}}]$ were the optimized vector parameters for the pore, Nylon, and SCF phases, respectively. To guide the optimization of Eq. (5.5), three intensity regions, C_P^l and C_P^u for the pore phase mean μ_P, C_N^l and C_N^u for the Nylon phase mean μ_N, and C_F^l and C_F^u for the SCF phase mean μ_F, were defined based on the examination of the phase intensity values $I(x,y)$ from each ROI and $h_m(I)$ in Figure 5.14(a). Figure 5.14(a) shows upper and lower bound intensity regions, C_P^l, C_P^u, C_N^l, C_N^u, C_F^l and C_F^u, that were provided for Eq. (5.6) constraints. Table 5.4 shows the initial conditions for three $\boldsymbol{\omega}$ parameters.

Table 5.4. MSGD algorithm initial conditions and optimized parameters for the MEX SCF part ROI A.

	Phase	$\mu_i(I)$, Phase Mean	$\sigma_i(I)$, Phase Standard Deviation	P_i, Phase Volume Percentage (%)	α_i, Phase Skew
Initial Conditions, $\boldsymbol{\omega}$	Pore, $\psi_P(I\|\boldsymbol{\omega_P})$	6000	500	20	0.0
	Nylon, $\psi_N(I\|\boldsymbol{\omega_N})$	8000	500	50	0.0
	SCF, $\psi_F(I\|\boldsymbol{\omega_F})$	9500	500	30	0.0

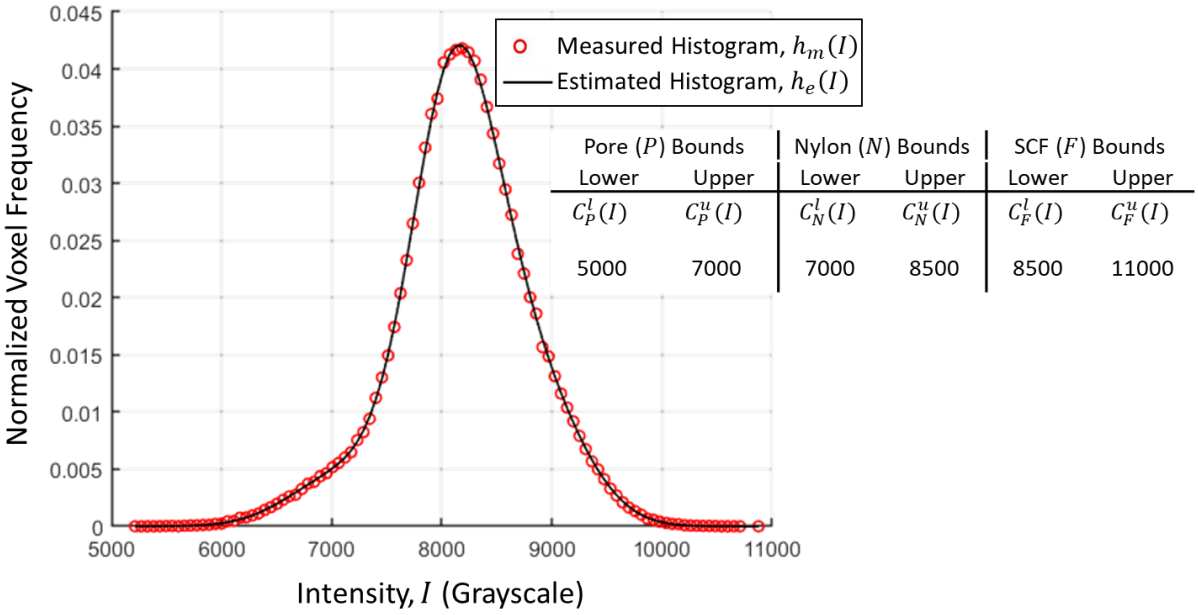

Pore (P) Bounds		Nylon (N) Bounds		SCF (F) Bounds	
Lower	Upper	Lower	Upper	Lower	Upper
$C_P^l(I)$	$C_P^u(I)$	$C_N^l(I)$	$C_N^u(I)$	$C_F^l(I)$	$C_F^u(I)$
5000	7000	7000	8500	8500	11000

(a)

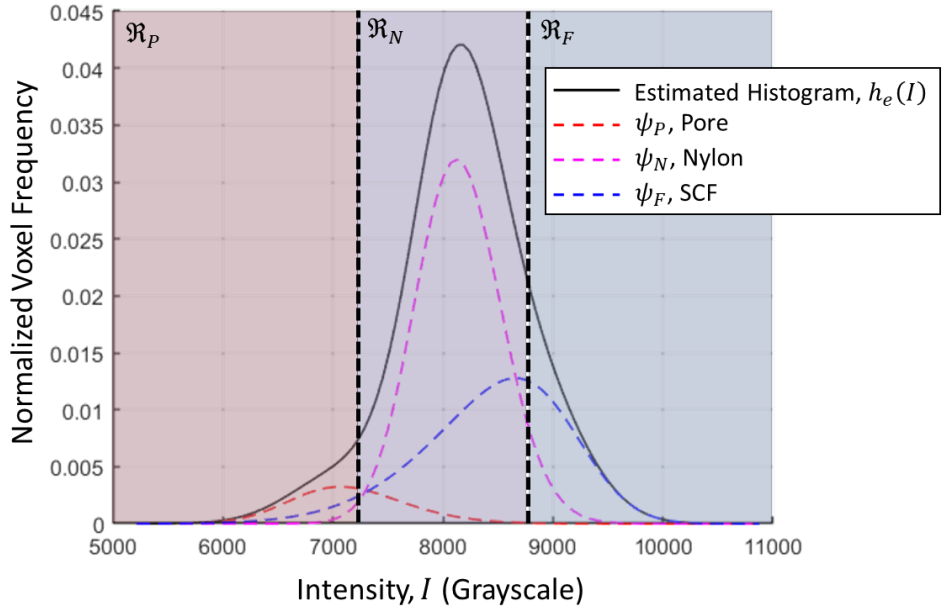

(b)

Figure 5.14. (a) The measured normalized histogram, $h_m(I)$, of voxel intensity values in grayscale and estimated histogram, $h_e(I|\hat{\boldsymbol{\omega}})$, of ROI A and (b) three phases – pore, Nylon, and SCF – with three Gaussian modes, ψ_P, ψ_N, and ψ_F. The Gaussian modes sum to the estimated histogram, $h_e(I|\hat{\boldsymbol{\omega}})$. Using BDR, $h_e(I|\hat{\boldsymbol{\omega}})$ is thresholded into three intensity regions, $\Re_P$, $\Re_N$, and $\Re_F$, for pore, Nylon, and SCF phases, respectively.

The estimated histogram, $h_e(I|\hat{\boldsymbol{\omega}})$, and the Gaussian modes $\psi_P(I|\boldsymbol{\omega_P})$, $\psi_N(I|\boldsymbol{\omega_N})$, and $\psi_F(I|\boldsymbol{\omega_F})$ for the pore, Nylon, and SCF phases, respectively, are shown in Figure 5.14(b) corresponding to the ROI A indicated in Figure 5.3. BDR was performed on the Gaussian modes

to define three intensity regions, $\Re_P$, $\Re_N$, and $\Re_F$, for the pore, Nylon, and SCF phases, respectively. From the resolving power of the CT machine and the 1.5 μm^3 resolution of the scan, the minimum allowable feature size was 4.5 μm^3. The MSGD algorithm was applied to segment each ROI into pore, Nylon, and SCF phases. The resultant thresholded images are shown in Figure 5.15.

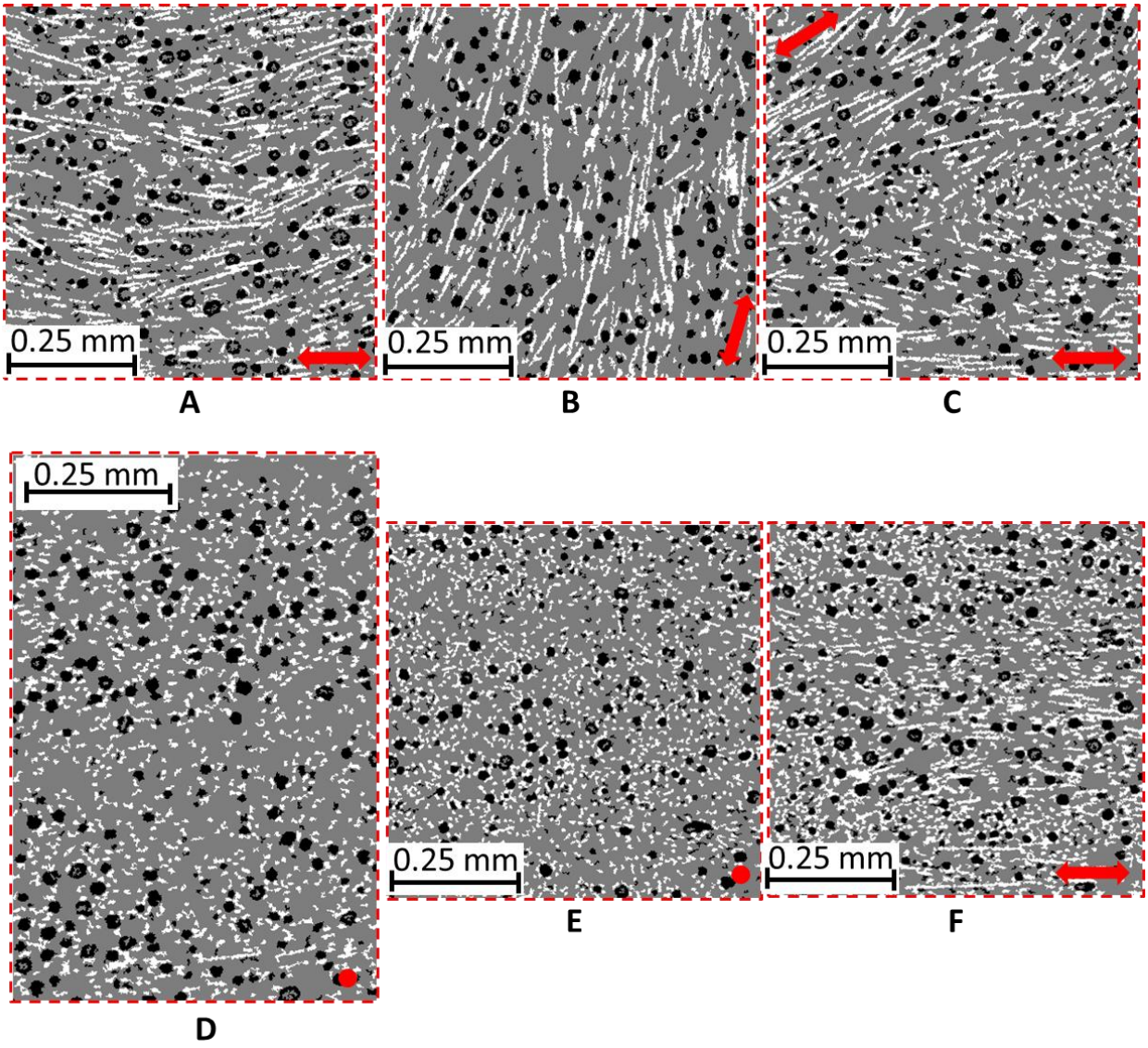

Figure 5.15. Thresholded ROIs of Figure 5.3. Toolhead travel directions indicated by red arrows (raster direction transverse to image) or red dot (raster direction normal to image).

5.5.2 Results from MSGD Algorithm for the MEX SCF Part

Using the MSGD algorithm of Sec. 5.3.4, each of the ROIs of Figure 5.3 were analyzed. Optimized phase parameters for each ROI are shown in Table 5.5. The average grayscale intensity values of the pore μ_P, Nylon μ_N, and SCF μ_F, were 6778, 7969, and 9027, respectively. The average standard deviations for the pore σ_P, Nylon σ_N, and SCF σ_F, were 795, 427, and 713, respectively. The standard deviations indicate, similar to the MEX SCF filament, that the intensity values of the pore and SCF phases were broader with a wider range of grayscale values and less certainty in the measurement compared with Nylon. The skew parameters for the pore α_P, Nylon α_N, and SCF α_F, were 1.7, 0.7, and -1.3, respectively. Similar to the MEX SCF filament, these skew parameters have a small magnitude indicating that most intensity values for each phase occurred symmetrically about their mean value. A higher contrast between phase distributions would be required to determine if the skew in the measurement suggests a physical phenomenon. Finally, the volume percentage of the pore P_P, Nylon P_N, and SCF P_F, phases were 9.8%, 59.6%, and 30.9%, respectively. The 9.8% porosity volume percentage indicates that the porosity in the part increased by more than 8% from the MEX SCF filament.

5.5.3 MEX SCF Part: Area and Distribution of Porosity

ROIs A to F were thresholded according to Secs. 5.3.4 and 5.5.1 and are shown in Figure 5.15. ROIs A and B show thresholded top views of a straight and curved MEX raster, respectively. ROI C shows the intersection between these rasters. From ROIs A and B, the SCFs can be seen mostly oriented in the direction of the toolhead travel, which indicates that the SCFs maintain their orientation from the MEX SCF filament. At the intersection zone (ROI C), the SCFs of the curved and straight raster can be seen following their respective toolpath directions at the top and bottom of the image. However, across the middle of ROI C, the SCFs appear to become reoriented to an

orientation normal to the image (round circles indicate SCFs normal to the image). This finding indicates a shearing effect that occurs at the intersection and causes the SCFs to rotate 90° into the XZ plane. From Sec. 5.3.6, the porosity distribution was quantified for ROIs A, B, and C.

Table 5.5. Optimized phase parameters for ROIs of each cross-sectional view.

ROI	Pore				Nylon				SCF			
	$\mu_P(I)$	$\sigma_P(I)$	$P_P(\%)$	α_P	$\mu_N(I)$	$\sigma_N(I)$	$P_N(\%)$	α_N	$\mu_F(I)$	$\sigma_F(I)$	$P_F(\%)$	α_F
A	6682	712.8	7.4	1.6	7901	461.2	55.8	0.9	9173	987.3	36.8	-2.2
B	6652	1074.8	11.2	3.4	7930	455.5	59.8	1.0	9198	914.0	29.0	-2.5
C	7000	469.2	8.1	0.2	8206	372.8	61.1	-0.4	8654	472.8	30.8	0.2
D	6771	1065.2	14.1	2.3	7945	409.7	58.6	0.8	9006	565.0	27.3	-1.0
E	6770	844.6	8.9	1.8	7938	409.4	65.6	0.7	9109	624.3	26.5	-1.2
F	6794	604.4	8.8	1.1	7898	454.7	56.5	0.9	9024	712.5	34.7	-1.3
Ave	6778	795.2	9.8	1.7	7969	427.2	59.6	0.7	9027	712.7	30.9	-1.3
StDev	122.4	246.2	2.5	1.1	117	35.5	3.6	0.5	198	201.5	4.1	1.0

Figure 5.16 shows the number of pores per ROI area (0.75 mm × 0.75 mm) and the average area of pores for each ROI of the XY cross-section. The intersection zone (ROI C) was found to have the highest number of pores per ROI area but not the largest average area of pores. One possible explanation is the shearing that reorients the SCFs acts to compress the voids in this intersection zone.

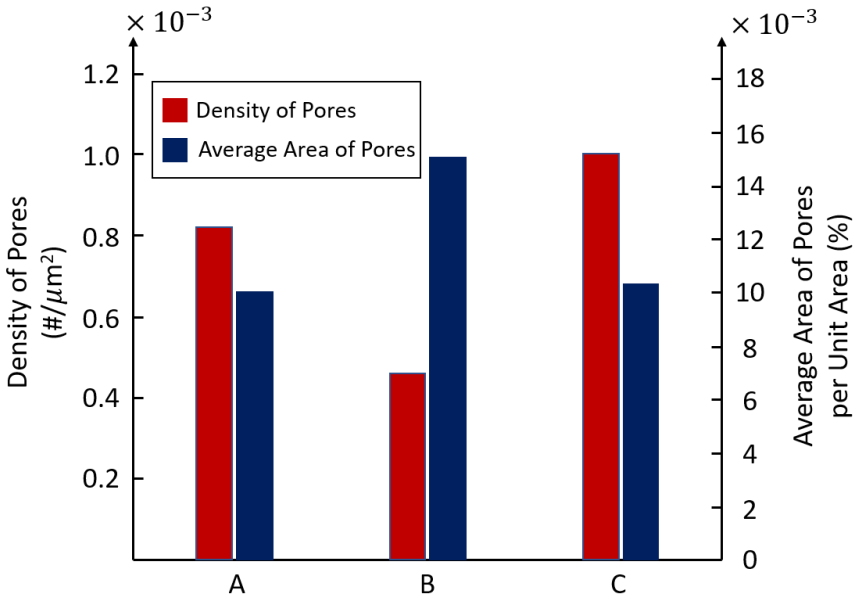

Figure 5.16. Pore density per ROI area and average area of pores per ROI area for ROI A (straight raster), B (curved raster), and C (intersection zone).

The porosity distribution and average pore area of ROI D, which is a view of the MEX layers, is shown in Figure 5.17 (dotted yellow lines represent layer interfaces corresponding to Figure 5.3). Throughout the layers of the part, the average pore area changed significantly across the ROI. At the interface between the two layers, the region below the interface (top of the layer during deposition) has nearly non-existent porosity with average pore area < 100 μm^2. The region above the interface has high average porosity (average pore area > 250 μm^2). This phenomenon is indicative of the MEX process in which molten thermoplastic is being extruded from a heated nozzle and deposited onto a colder layer below. The air may become entrapped at the bottom of the newly deposited layer whereas the air bubble may escape from the molten upper layer. Another potential explanation could be due to a large thermal stress and shrinkage of the Nylon at the bottom of a deposited layer compared to the top. A larger temperature gradient and contractile thermal stresses above the interface would shrink the thermoplastic into a smaller volume allowing the voids to grow. These voids contribute to the transverse isotropy in MEX parts.

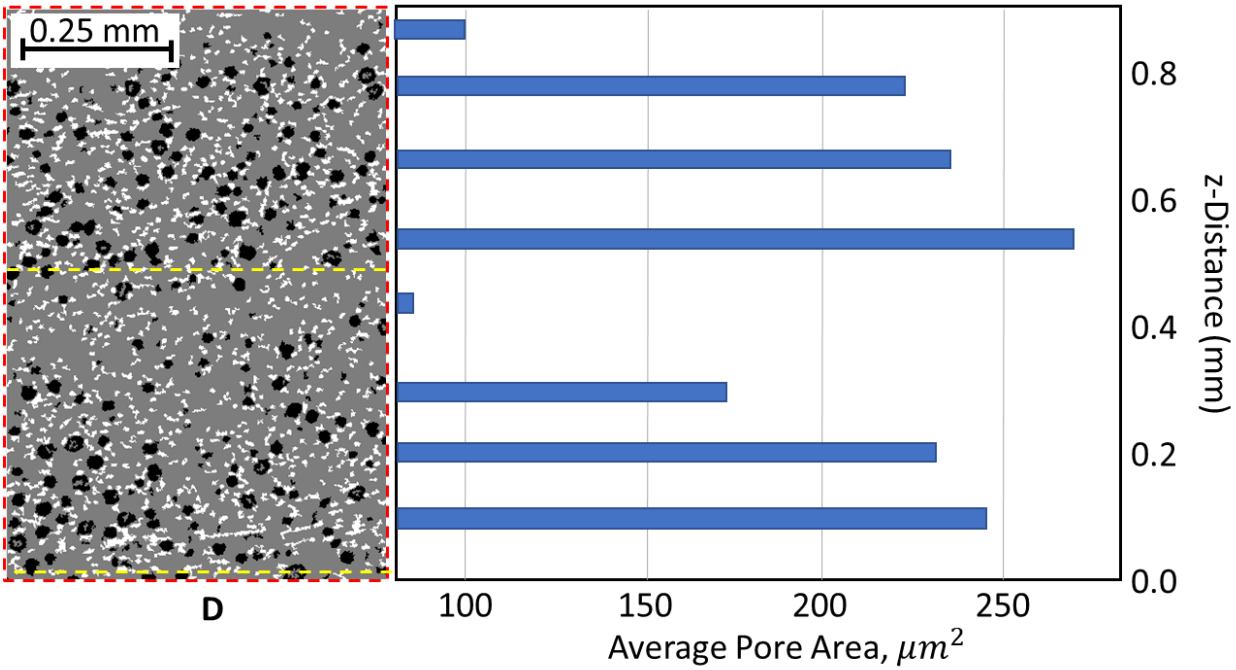

Figure 5.17. Average pore area along Z-direction in layer-to-layer XZ cross-sectional view (ROI D). The average pore area was found for pores within differential elements, dz =38 μm, along the z-direction. The largest area pores occur immediately above the layers, shown by the dotted line.

In Figure 5.15, the ROIs E and F show a cross-section of the straight and curved rasters, respectively. SCFs in ROI E are shown as circles indicating that their orientation is normal to the image and along the toolpath direction. The SCFs in ROI F are elongated but not the full expected length of the SCFs, indicating that the toolpath direction has a component normal and transverse to the image.

5.6 Conclusions

This paper presented the CT evaluations of a SCF Nylon filament and a part with a wave infill. Using the MSGD algorithm [76], the internal structure was segmented into three phases: pore, Nylon, and SCF. From this segmentation, the phase volume percentages of the MEX SCF filament were found to be 1.6% pore, 62.2% Nylon, and 36.2% SCF. MSGD analysis of sections of the MEX SCF part estimated phase volume percentages to be 9.8% pore, 59.6% Nylon, and 30.9% SCF. The measured volume percentage of SCF in both the MEX SCF filament and part

match closely with the 35 wt% of SCF provided by the manufacturer. Furthermore, from this analysis the porosity of the filament to the part during the MEX process increases more than 8%. This increase in porosity is expected to lead to a lower strength in the MEX SCF parts.

CT analysis found most pores within the filament to have a volume under 100 μm^3. The largest pores were shown to be at the center of the filaments, suggesting that large pores became trapped or were generated during the cooling process. Higher pore density was found at outside the filament.

For the MEX SCF part, several ROIs were defined across multiple image views to evaluate the SCF orientation and to quantify the porosity density and distribution. SCFs were found to be oriented along the direction of toolpath travel. In the region of intersection between two rasters on a single layer, the SCFs appear to become reoriented normal to the toolpath direction, potentially because of a shearing effect between the two rasters. Within this intersection zone, pores occurred more frequently but with smaller average area compared to that measured in the intersecting rasters.

For the MEX SCF part, the average pore area and porosity distribution were measured at the interface between MEX layers. The top of the layer had nearly non-existent porosity (average pore area < 100 μm^2). The bottom of the layer had high average porosity (average pore area > 250 μm^2), which is expected to contribute to the transverse isotropy in MEX parts.

These findings indicate that layer-to-layer porosity within MEX parts is significant. During experimentation with the AFO, the AFO consistently failed within one month of use. Fractures initiated at surface structural voids and propagated through the entire layer. Because TWSs such as the AFO have small thicknesses with few beads, there is a small safety factor of material to resist loading once cracks initiate.

Future work includes minimizing the porosity by adjusting process parameters and relating the MEX SCF parts' mechanical properties to the internal porosity and the SCF orientation. This data would allow optimization of the MEX process to reduce problematic porosity between layers. CT data can also be used to ensure that the orientation of SCFs is appropriate to the expected loading conditions on a part.

Chapter 6
Conclusions and Future Work

6.1 Conclusions

This thesis investigated the use of MEX in the fabrication of a TWS, such as the AFO. Three requirements for the AFO and other TWSs fabricated by MEX are that they are lightweight and durable and have tunable structural stiffness.

To fabricate a lightweight TWS with tunable structural stiffness, the MEX wave infill, a method of filling the interior of the TWS with a truss-like porous core, was studied in Chapters 2 and 3 of this thesis. The key advantage of the wave infill is that its truss-like structure minimizes TWS mass and homogenizes the TWS for characterization of its structural stiffness. Four metrics affected by the wave infill geometry – stiffness, load capacity, fabrication time, and mass – were studied. Analytical models for these metrics were developed that showed correlations above 85% to experimental measurements. The predictive capabilities of stiffness, mass, and fabrication time analytical models were found to show errors less than 10% compared to experimental measurements. However, prediction of the load capacity of the MEX parts using the analytical model was less accurate. Load capacity was predicted within 25% of experimental values. Possible explanations of the modelling difficulties for load capacity include layer-to-layer weaknesses present in MEX parts or overlap bonding between the wave infill and the outer facings of the TWS. The high strength- and stiffness-to-mass ratios of the wave infill has been demonstrated in the literature for applications such as corrugated paperboard. This study employs mechanical principles from the study of corrugated cardboard and has been developed specifically for MEX wave infill. The models developed in Chapter 2 enable the design of MEX TWSs with uniform

wave infill geometries. Using the sensitivity of MEX TWSs to each of the wave infill geometrical parameters, the stiffness, load capacity, mass, and fabrication time can be used as design tools for simple TWSs in bending. Limitations of this study, however, are that the analytical tools developed in Chapter 2 are limited to simple geometries and loading conditions.

Using these analytical models, a composite simplification model (CSM) of the wave infill in TWSs with generalized geometries was developed. In CSM, the wave infill and TWS faces are modelled as a homogenous stacked composite, which reduces computation and setup time. CSM for the wave infill was found to predict the stiffness of experimental measurements within 15%. The combination of the sensitivity analysis in Chapters 2 and CSM for analyzing generalized TWSs in Chapter 3 serves as an important addition to the MEX community that currently has few options for designing and analyzing MEX structures. An analysis performed on a fixed flat- and AFO-geometry shows CSM to be a powerful finite element and design tool that can optimize the wave infill for TWSs. The CSM tool was developed specifically to interface with structural optimization techniques. From the four input parameters that define a wave infill element, CSM is used to determine the element stiffness. These elements can then be used as building blocks for analyzing the stresses and strains in complex TWSs with wave infill. Elements can have varying wave infills to achieve desired properties such as minimizing mass and achieving a structural stiffness. Future work in this area includes identifying methods to ensure proper fabrication of varying wave infill segments during the MEX process. Other areas of research include validating assumptions that were used to simplify the CSM for wave infill that varies throughout a structure.

To improve the fabrication of durable TWSs, CT was used to inspect the internal structure of MEX parts. To improve quantification of MEX parts analyzed by CT, the MSGD method, an advanced segmentation technique, was developed in Chapter 4. In MSGD, the parameters of

skewed Gaussian distributions were inferred from the measured grayscale histogram from the CT analysis. Using the randomness inherent in the CT data, important physical information such as phase percentages, mean density, and phase distribution can be inferred. The skewness of the MSGD method may provide physical information regarding intra-phase density variations. The MSGD method predicted the porosity of an AM specimen from NIST to within 1% of its experimentally measured value. MSGD provides a method for repeatably fitting skew Gaussian distributions such as those that may occur during CT of AM parts.

In Chapter 5, MSGD was applied to quantify the internal structure of a MEX SCF filament and part. From this analysis, the phase percentages of the MEX SCF filament were found to be 1.6% pore, 62.2% Nylon, and 36.2% SCF. MSGD analysis of sections of the MEX SCF part estimated phase volume percentages to be 9.8% pore, 59.6% Nylon, and 30.9% SCF. From this analysis the porosity of the filament to the part during the MEX process increases more than 8% indicating that porosity likely increases during the MEX layer stacking process. This increase in porosity is expected to lead to a lower strength in the MEX SCF parts. For the MEX part, average void area was found to be highest (>250 μm^2) at the bottom of the layer and smallest (<100 μm^2) at the top of the layer, which could be explained by a large temperature gradient between layers and contractile thermal stresses inside the layer that causes the thermoplastic to have increased shrinkage resulting in larger voids. Heated ovens in high-end printers were introduced to improve the temperature gradients that occur during the layer stacking process. This heating gradient may be an important process parameter that needs to be studied in relation to porosity formation. Porosity distributions that were found in this paper may also be used in thermal analyses to study the curing residual stresses that occur in MEX parts. Models may be developed that simulate important MEX process parameters and their contribution to the porosity within MEX parts.

Inspection techniques reported in this thesis may be used to quickly and repeatably evaluate images for rapid analysis of MEX parts.

During testing of several MEX AFOs that had varying shapes, thicknesses, build orientations and material, each AFO fractured along layer lines within a month of use. This thesis showed that, in addition to structural voids in MEX parts, layer-to-layer porosity occurs, as well. Within MEX TWSs such as the AFO, these layer-to-layer voids likely the increase the likelihood of fatigue fractures that occur during use. Small fractures may initiate at structural voids and propagate into the part easily passing through the high porosity layer-to-layer voids that occur. To ensure that MEX AFOs remain durable, process parameters that induce structural and layer-to-layer voids must be improved.

Overall, this thesis shows: (1) the wave infill can be used to generate a lightweight TWS with tunable structural stiffness, (2) CSM is a powerful finite element technique that may be used to design MEX wave infill TWSs, (3) CT and MSGD may be used to quantify the internal structure of MEX filaments and parts, and (4) voids from the MEX process occur at interfaces between layers, possibly due to large thermal gradients and plastic shrinkage. This research will inform and improve the MEX fabrication process to fabricate TWSs with tunable structural stiffnesses and are lightweight and durable.

6.2 Future Work

Future work in this area will be through industry collaboration. The MEX wave infill for structural property mapping is currently a licensed technology to Stratasys. The research work presented here establishes a foundation for sizing and topology optimization of the wave infill. Using CSM, the wave infill period and TWS thickness can be adjusted depending on the stress field generated from the loading conditions. From this research, the stiffness and mass of the wave

infill TWS can be adjusted to generate tunable stiffness structures that have minimized mass. To implement the non-uniform wave infill, software to generate appropriate machine paths that appropriately deposit the material are required. Once fabrication methods for the wave infill are established, the ability of the CSM to model non-uniform and non-symmetric wave infills should be tested experimentally.

For MEX material inspection, additional work to characterize and quantify the distribution and orientation of SCF is required. In addition to voids between layers, the reason for the anisotropic nature of MEX SCF materials is that the SCFs do not pass between layers. Therefore, the effects of SCF are only seen within a layer. During investigation of the CT data set presented in Chapter 5 of this thesis, shearing effects in the intersection zone reoriented the fibers out of the plane of the layer. This phenomenon is being explored in more with the CT data to determine if a shearing method could be used to improve inter-layer strengths of MEX SCF parts.

Appendix A
Stiffness Analytical Model of MEX Wave Infill Flexural Specimen

The flexural stiffness analytical model K^A for four-point bending and directional area moment of inertia terms, I_Z and I_X, are derived.

A.1 Stiffness Derivation

The stiffness of a beam in flexural loading K^A for the four-point bending flexural is the slope of the load versus deflection curve:

$$K^A = \frac{F_B}{\delta(x)|_{x=b}} \tag{A.1}$$

where F_B is the load applied to the beam, $\delta(x)$ is the deflection of the beam along its length, x is the distance along the beam, and b is the distance between the support and loading pins. In four-point flexure, the loading pins are offset from each other and from the supports by a distance a and b, respectively, as shown in Figure A.1.

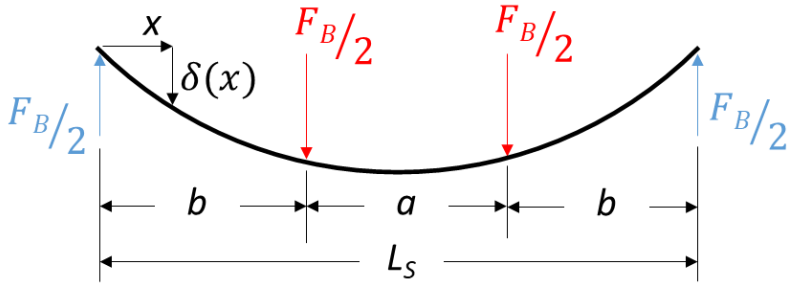

Figure A.1. Beam in four-point flexure with reaction and loading pin forces $F_B/2$, support span Ls, loading distance a, and deflection of $\delta(x)$ at distance x along the beam.

Using the deflection of a beam under a single point load at a distance b from the support [77]:

$$\delta(x)|_{x=b} = \frac{F_B\, b\, (a - L_s)}{96\, E\, I\, L_s}(a^2 + 4\, b^2 - 2\, a\, L_s - 3\, {L_s}^2) \tag{A.2}$$

where E is the flexural modulus, I is the area moment of inertia, and L_S is the supported length. Based on the principle of superposition, the loading pin deflection $\delta(x)$ in four-point loading is:

$$\delta(x) = \frac{F_B\, x}{48\, E\, I}(3\, a^2 + 4\, x^2 - 3\, {L_s}^2) \tag{A.3}$$

Based on Eq. (A.3), the deflection at $x = b$ is:

$$\delta(x)|_{x=b} = \frac{F_B}{48\, E\, I}(2\, a^3 - 3\, a^2\, L_s + \, {L_s}^3) \tag{A.4}$$

Combining Eqs. (A.1) and (A.4), the analytical flexural stiffness K^A of a beam under four-point loading is:

$$K^A = \frac{48\, E\, I}{({L_s}^3 - 3\, a^2\, L_s + \, 2\, a^3)} \tag{A.5}$$

A.2 In-Plane Area Moment of Inertia, I_Z

The in-plane area moment of inertia I_Z is required to estimate the analytical stiffness and load capacity of the MEX wave infill flexural beams. As shown in Figure A.2, the cross-section A-A of the of the in-plane MEX wave infill flexural beam is composed of two outer contours and the wave infill. Because the distance from the neutral axis to the midline of the wave infill varies along the length of the beam, the contribution of the wave infill to the in-plane I_Z is neglected [21]. Using the area moment of inertia of a rectangle and the principle of superposition, the I_Z is $I_Z^{outer} - I_Z^{inner}$ as shown in Figure A.2:

$$I_Z = I_Z^{contour} = \, I_Z^{outer} - I_Z^{inner} = \frac{1}{12} w\, (T^3 - (T - 2W)^3) \tag{A.6}$$

where w is width of the section and $I_Z^{outer} = \frac{1}{12} w T^3$ and $I_Z^{inner} = \frac{1}{12} w\, (T - 2W)^3$.

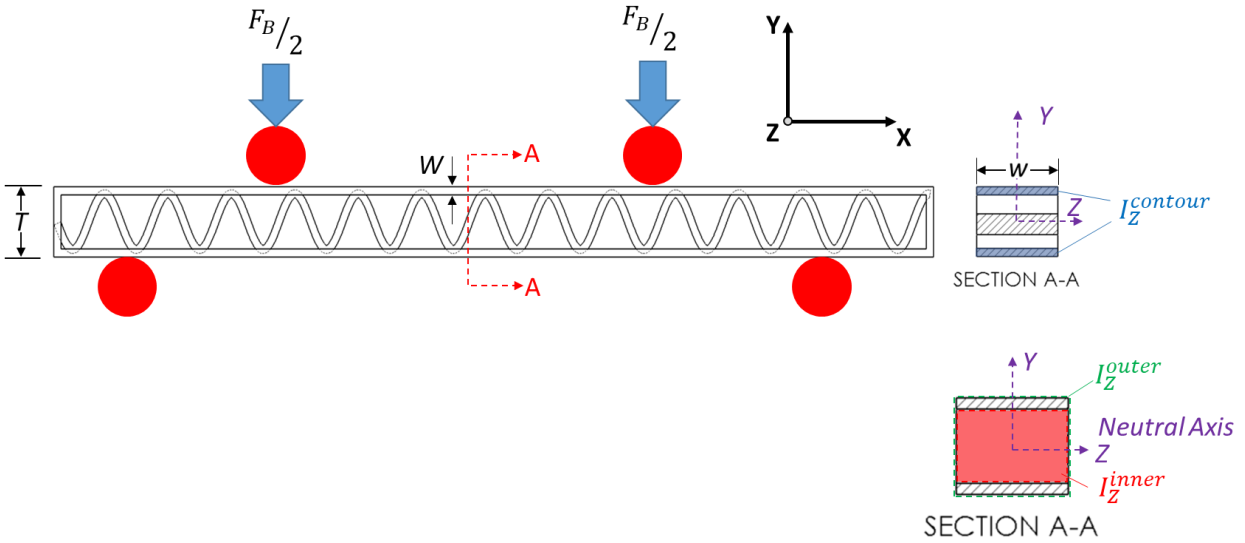

Figure A.2. Section A-A of the bending portion of the in-plane flexural beam with thickness, T, beadwidth, W, width, w, and neutral axis, Z. The regions of area moment of inertia terms $I_Z^{contour}$, I_Z^{outer} and I_Z^{inner} are shown.

A.3 Layer-to-Layer Area Moment of Inertia, I_X

The layer-to-layer area moment of inertia I_X is required to estimate the analytical stiffness and load capacity of the MEX wave infill flexural beams. Expressions for I_X are adapted from Luo *et al.* [21] to match the geometry and constraints for the MEX wave infill described in Sec. 2.4.1. As shown in Figure A.3, the cross-section of the bending portion of the layer-to-layer flexural beam is composed of two outer contours and the wave infill. I_X is, therefore, the contribution of the I_X of the outer contours and the wave infill:

$$I_X = I_X^{contour} + I_X^{wave} \tag{A.7}$$

where $I_X^{contour}$ is the same form as given in Eq. (A.6) and I_X^{wave} is obtained by the principle of superposition of the area moment of inertia terms, I_X^{upper} and I_X^{lower}:

$$I_X^{wave} = I_X^{upper} - I_X^{lower} \tag{A.8}$$

where I_X^{upper} and I_X^{lower} are found by integrating differential elements dI_X^{upper} and dI_X^{lower}, respectively, as shown in Figure A.4(a).

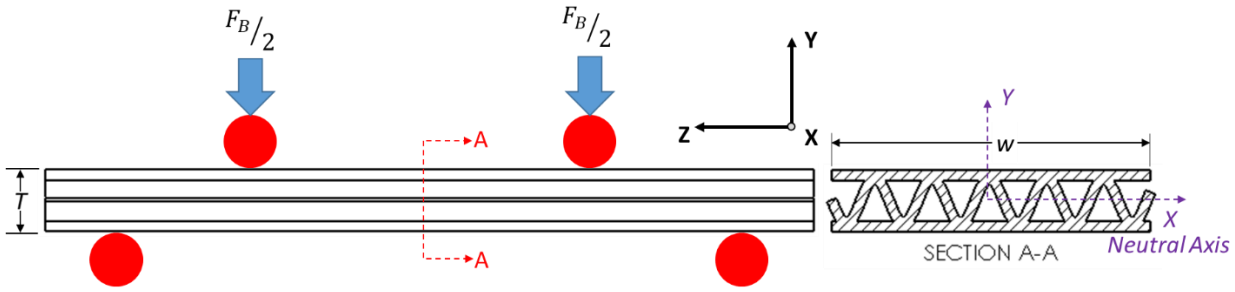

Figure A.3. Cross-section of the bending portion of the layer-to-layer flexural beam with thickness, T, width, w, and neutral axis, X.

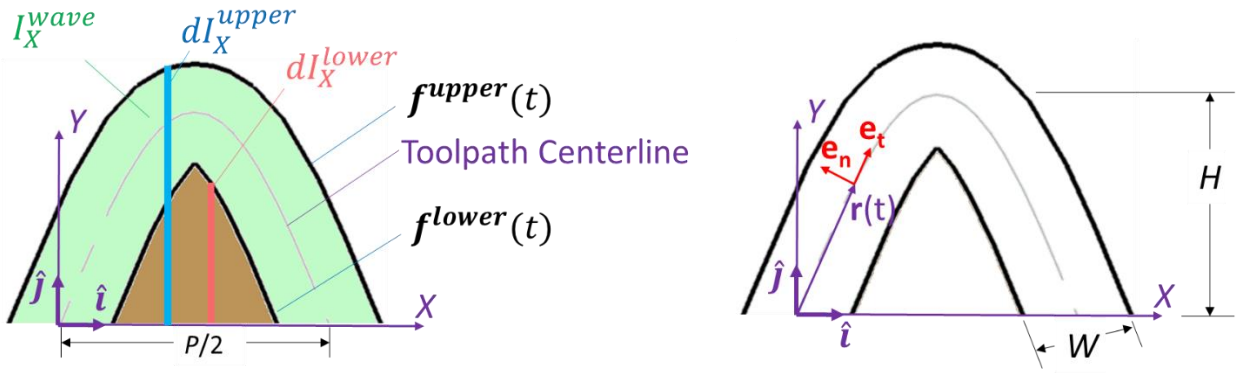

(a) (b)

Figure A.4. Half period of the wave infill indicating (a) toolpath centerline, upper and lower toolpath boundaries, and upper and lower regions of area moment of inertia terms and (b) parameterized toolpath centerline, $\boldsymbol{r}(t)$, and tangential and normal unit vectors.

To calculate I_X^{upper} and I_X^{lower}, a half-period of the toolpath centerline, $y(x)$ (Eq. (2.5) is parameterized as $\boldsymbol{r}(t)$ (Figure A.4(b)):

$$\boldsymbol{r}(t) = t\,\hat{\boldsymbol{\imath}} + H\sin\left(\frac{2\pi}{P}\,t\right)\hat{\boldsymbol{\jmath}} \tag{A.9}$$

where $t \in [0, P/2]$, H is the amplitude of the wave, P is the period of the wave, and $\hat{\boldsymbol{\imath}}$ and $\hat{\boldsymbol{\jmath}}$ are the X- and Y-direction unit vectors, respectively. From $\boldsymbol{r}(t)$, the upper and lower boundaries of the wave infill are defined by the vector functions, $\boldsymbol{f}^{upper}(t)$ and $\boldsymbol{f}^{lower}(t)$, respectively. These vector functions are obtained by offsetting $\boldsymbol{r}(t)$ along its pointwise normal unit vector $\boldsymbol{e_n}$:

$$\boldsymbol{f}^{lower}(t) = \boldsymbol{r}(t) + \frac{W}{2}\,\boldsymbol{e_n} \tag{A.10}$$

$$\boldsymbol{f}^{upper}(t) = \boldsymbol{r}(t) - \frac{W}{2}\,\boldsymbol{e_n} \tag{A.11}$$

where W is the beadwidth. Normal and tangential unit vectors, $\boldsymbol{e_n}$ and $\boldsymbol{e_t}$, respectively, can be defined along the toolpath centerline as shown in Figure A.4(b). The tangential unit vector, $\boldsymbol{e_t}$, is:

$$\boldsymbol{e_t} = \frac{\boldsymbol{dr}}{\boldsymbol{ds}} = \frac{\boldsymbol{dr}}{\boldsymbol{dt}} \frac{dt}{ds} \tag{A.12}$$

where ds is the differential arc length. Based on Eq. (2.8),

$$ds = \sqrt{1 + \left(\frac{2\pi}{P} H \cos\left(\frac{2\pi}{P} x\right)\right)^2}\, dt \tag{A.13}$$

and $\frac{\boldsymbol{dr}}{\boldsymbol{dt}}$ is:

$$\frac{\boldsymbol{dr}}{\boldsymbol{dt}} = 1\ \hat{\boldsymbol{\imath}} + \frac{2\,H\,\pi}{P}\cos\left(\frac{2\pi}{P}\ t\right)\hat{\boldsymbol{\jmath}} \tag{A.14}$$

Combining Eqs. (A.12), (A.13), and (A.14), the tangential unit vector is:

$$\boldsymbol{e_t} = \left(P\ \hat{\boldsymbol{\imath}} + 2\pi H \cos\left(\frac{2\pi}{P}\ t\right)\hat{\boldsymbol{\jmath}}\right)\frac{1}{\sqrt{P^2 + 4\,H^2\pi^2\cos^2\left(\frac{2\pi}{P}\ t\right)}} \tag{A.15}$$

Because $\boldsymbol{e_n}$ and $\boldsymbol{e_t}$ are orthogonal, their inner product is equal to zero. Therefore, the normal unit vector can be solved for its component directions to find:

$$\boldsymbol{e_n} = \left(2\pi H \cos\left(\frac{2\pi}{P}\ t\right)\hat{\boldsymbol{\imath}} - P\,\hat{\boldsymbol{\jmath}}\right)\frac{1}{\sqrt{P^2 + 4H^2\pi^2\cos^2\left(\frac{2\pi}{P}\ t\right)}} \tag{A.16}$$

As can be seen from Figure 2.6, the thickness of the peaks and troughs of some of the wave infill experiment samples overlaps between successive periods. This overlapping effect can be explained by the high radius of curvature at the peaks and troughs of the wave toolpath centerline. For specimens with high radius of curvature (e.g. Experiment 3), offsetting the toolpath centerline to obtain the lower boundary curve, $\boldsymbol{f^{lower}}(t)$, as shown in Figure A.5(a), leads to an undefined function. To ensure the function remains defined regardless of radius of curvature, the $\hat{\boldsymbol{\imath}}$-component of $\boldsymbol{f^{lower}}(t)$ is set equal to $P/4$ and solved for t. This t, t_f^{lower}, defines the upper limit

of the domain of $\boldsymbol{f}^{\boldsymbol{lower}}(t)$. Several periods of the corrected infill and the corresponding microscope image are shown in Figure A.5(b)-(c), respectively.

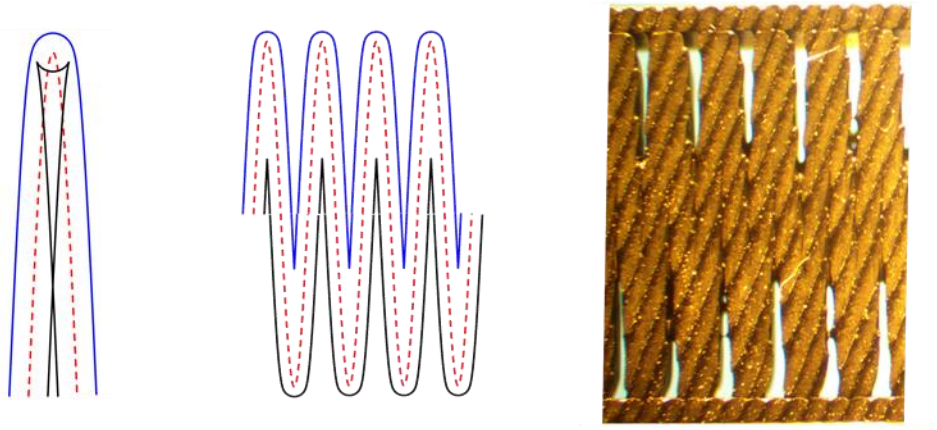

(a) (b) (c)

Figure A.5. (a) Overlapping effect due to the high radius of curvature at peak of toolpath centerline, (b) corrected boundary curves, and (c) microscope image of Experiment 3 of the wave infill specimen set.

The general form of the area moment of inertia I_X can be calculated with respect to the X-axis using:

$$I_X = \int \boldsymbol{f}(t)^2 \, dA \tag{A.17}$$

which can be written using Green's function as [78]:

$$I_X = \frac{1}{3}\int_{t_0}^{t_f} f_{\hat{\boldsymbol{j}}}(t)^3 \, f_{\hat{\boldsymbol{i}}}{}'(t) \, dt \tag{A.18}$$

where t_0 and t_f are the limits of integration, $f_{\hat{\boldsymbol{j}}}(t)$ is the $\hat{\boldsymbol{j}}$-component of the boundary function, $\boldsymbol{f}(t)$, and $f_{\hat{\boldsymbol{i}}}{}'(t)$ is the derivative of the $\hat{\boldsymbol{i}}$-component of the boundary function, $\boldsymbol{f}(t)$. Because of the symmetry of the wave, the limit of integration, t_f, is simply a quarter-period of the wave, $P/4$.

Rewriting Eq. (A.18), the upper area moment of inertia I_X^{upper} is:

$$I_X^{upper} = \frac{1}{3}\int_{t_0^{upper}}^{t_f} (f_{\hat{\boldsymbol{j}}}^{upper}(t))^3 \; f_{\hat{\boldsymbol{i}}}^{upper\prime}(t) \, dt \tag{A.19}$$

The limit of integration, t_0^{upper}, representing the intersection between the boundary curve, $\boldsymbol{f^{upper}}(t)$, and the *X*-axis. t_0^{upper} is found by setting the $\hat{\boldsymbol{j}}$-components of $\boldsymbol{f^{upper}}(t)$ (Eq. (A.11)) equals to zero and substituting trigonometric identities:

$$t_0^{upper} = \frac{-P}{2\pi}\cos^{-1}\left(\frac{-H^2\,P^2 + \sqrt{H^4\left(P^4 + 16\,H^4\pi^4 + 4\,P^2\,\pi^2\,(2H^2 - W^2)\right)}}{4\,H^4\,\pi^2}\right) \tag{A.20}$$

The derivative, $f_{\hat{\boldsymbol{i}}}^{upper\prime}(t)$, of the $\hat{\boldsymbol{i}}$-component of $\boldsymbol{f^{upper}}(t)$ is:

$$f_{\hat{\boldsymbol{i}}}^{upper\prime}(t) = 1 + \frac{2\,H\,P\,\pi^2\,W\sin\left(\frac{2\pi}{P}\,t\right)}{\left(P^2 + 2\,H^2\,\pi^2 + 2\,H^2\,\pi^2\cos\left(\frac{4\pi}{P}\,t\right)\right)^{3/2}} \tag{A.21}$$

Combining Eqs. (A.9), (A.11), (A.16), (A.19), (A.20), and (A.21) and recalling the quarter symmetry conditions, I_X^{upper} is:

$$I_X^{upper} = \frac{4}{3}\int_{t_0^{upper}}^{P/4}\left(H\sin\left(\frac{2\pi}{P}\,t\right) - \frac{P\,W}{2\sqrt{P^2 + 4H^2\pi^2\cos^2\left(\frac{2\pi}{P}\,t\right)}}\right)^3\left(1 + \frac{2\,H\,P\,\pi^2\,W\sin\left(\frac{2\pi}{P}\,t\right)}{\left(P^2 + 2\,H^2\,\pi^2 + 2\,H^2\,\pi^2\cos\left(\frac{4\pi}{P}\,t\right)\right)^{3/2}}\right)dt \tag{A.22}$$

which can be numerically integrated to find I_X^{upper}.

Similarly, Eq. (A.18) is rewritten for the lower area moment of inertia I_X^{lower} using boundary function $\boldsymbol{f^{lower}}(t)$ (Eq. (A.10)):

$$I_X^{lower} = \frac{1}{3}\int_{t_0^{lower}}^{t_f}(f_{\hat{\boldsymbol{j}}}^{lower}(t))^3\;f_{\hat{\boldsymbol{i}}}^{lower\prime}(t)\,dt \tag{A.23}$$

The limit of integration t_0^{lower} is:

$$t_0^{lower} = \frac{P}{2\pi} \cos^{-1}\left(\frac{-H^2\,P^2 + \sqrt{H^4\left(P^4 + 16\,H^4\pi^4 + 4\,P^2\,\pi^2\,(2H^2 - W^2)\right)}}{4\,H^4\,\pi^2}\right) \tag{A.24}$$

The derivative, $f_{\hat{\imath}}^{lower'}(t)$, of the $\hat{\imath}$-component of the upper boundary function, $\boldsymbol{f}^{\boldsymbol{lower}}(t)$, is:

$$f_{\hat{\imath}}^{lower'}(t) = 1 - \frac{2\,H\,P\,\pi^2\,W\sin\left(\frac{2\pi}{P}\,t\right)}{\left(P^2 + 2\,H^2\,\pi^2 + 2\,H^2\,\pi^2\cos\left(\frac{4\pi}{P}\,t\right)\right)^{3/2}} \tag{A.25}$$

Combining Eqs. (A.9), (A.10), (A.16), (A.23), (A.24), and (A.25), I_X^{lower} is:

$$I_X^{lower} = \frac{4}{3}\int_{t_0^{lower}}^{t_f^{lower}} \left(H\sin\left(\frac{2\pi}{P}\,t\right) + \frac{P\,W}{2\sqrt{P^2 + 4H^2\pi^2\cos^2\left(\frac{2\pi}{P}\,t\right)}}\right)^3 \left(1 - \frac{2\,H\,P\,\pi^2\,W\sin\left(\frac{2\pi}{P}\,t\right)}{\left(P^2 + 2\,H^2\,\pi^2 + 2\,H^2\,\pi^2\cos\left(\frac{4\pi}{P}\,t\right)\right)^{3/2}}\right) dt \tag{A.26}$$

which, likewise, must be numerically integrated to find I_X^{lower}.

Appendix B
Load Capacity Analytical Model of MEX Wave Infill Flexural Specimen

The load capacity L^A of a beam in flexure is the peak load F_B that the beam can withstand. To calculate the load capacity, the strength, S, of a beam under flexural loading is given by [77]:

$$S = \frac{M_{max} T}{2\, I} \tag{B.1}$$

where M_{max} is the maximum bending moment in the beam, T is the thickness of the beam (Sec. 2.4.1), and I is the beam area moment of inertia (Appendices A.2 and A.3). M_{max} occurs between two inner loading pins in four-point bending, as shown in Figure B.1:

$$M_{max} = \frac{F_B b}{2} \tag{B.2}$$

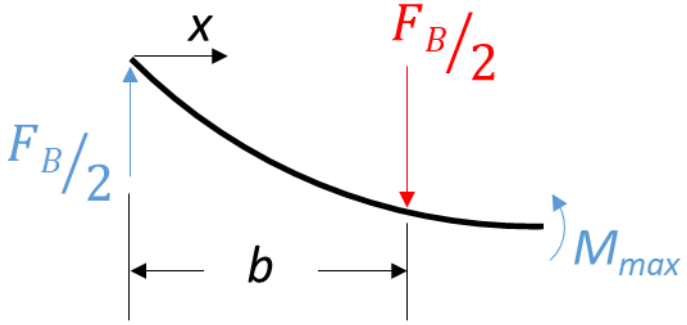

Figure B.1. Free-body diagram four-point bending flexure with reaction and loading pin forces $F_B/2$, the distance between adjacent loading and support noses, b, and the maximum moment, M_{max} in the beam.

Solving Eqs. (B.1) and (B.2) for F_B and with $b = (L_s - a)/2$ as shown in Figure B.1, the load capacity, L^A, of a beam in four-point flexural loading is:

$$L^A = \frac{8\, S\, I}{T\, (L_s - a)} \tag{B.3}$$

Appendix C
Fabrication Time of MEX Wave Infill Flexural Specimen

The analytical model for fabrication time of the wave infill specimen is derived. The wave infill with period P and amplitude H is shown in Figure C.1(a). The MEX machines operate as Cartesian gantries that use two independent linear stages to generate orthogonal movement of the extruder head assembly. The linear stage can be modeled as providing a constant acceleration or deceleration, a_m, until a target, or maximum speed, v_m, is achieved [79].

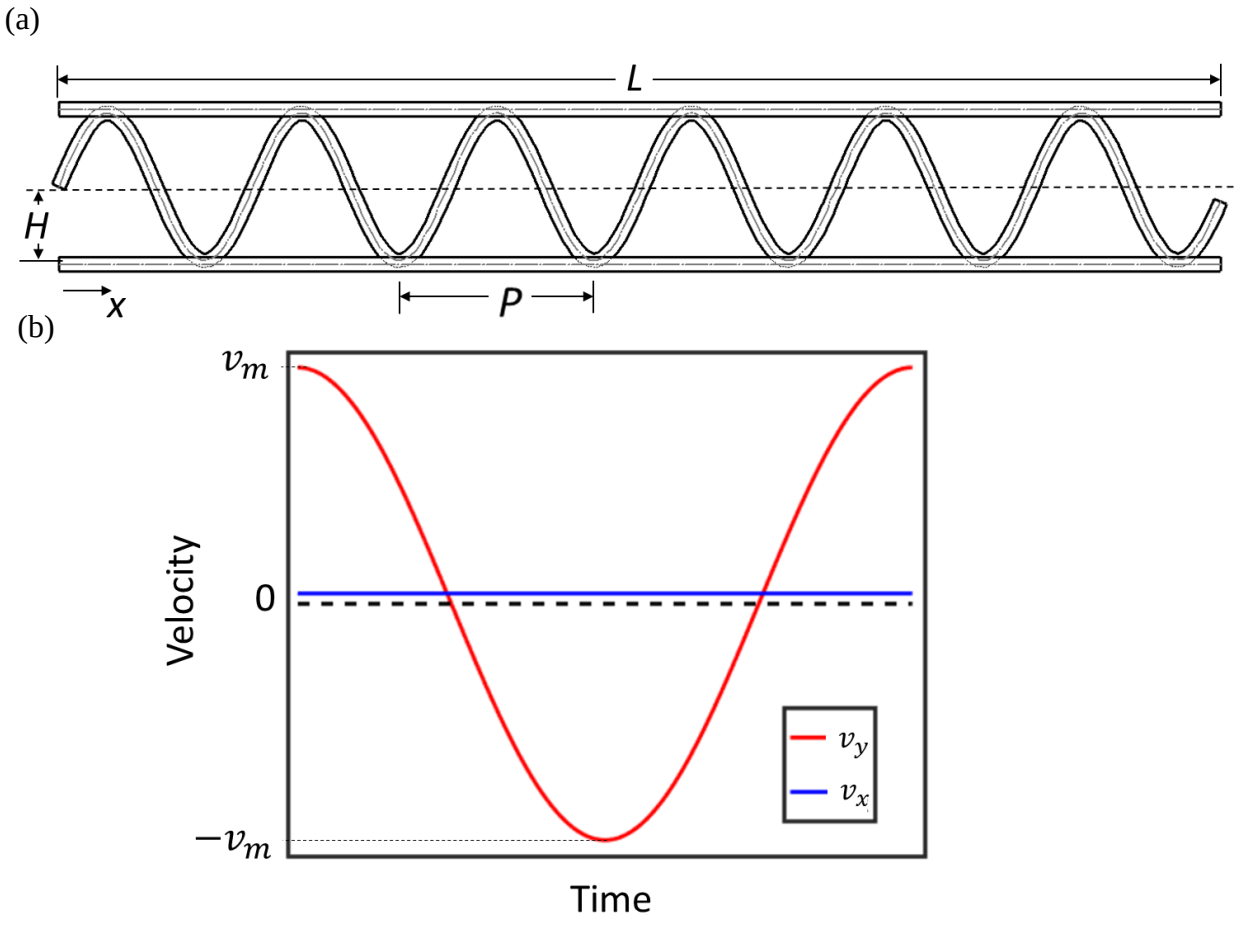

Figure C.1. (a) The wave infill specimen with amplitude, H, period, P, and length, L and (b) velocity profile with a constant x-velocity component and an oscillating y-velocity component between v_m and $-v_m$.

With these assumptions and considering the toolpath centerline given by Eq. (2.5), the toolhead motion through the toolpath centerline can be parameterized as:

$$x(t) = v_x\, t \tag{C.1}$$

$$y(t) = H \sin\left(\frac{2\pi}{P}\, v_x t\right) \tag{C.2}$$

where v_x is the linear velocity of the toolhead in the X-direction and t is the time. The first and second derivatives of the parameterized paths are:

$$\dot{x}(t) = v_x \tag{C.3}$$

$$\ddot{x}(t) = 0 \tag{C.4}$$

$$\dot{y}(t) = \frac{2\pi}{P} H\ v_x \cos(\frac{2\pi}{P}\, v_x t) \tag{C.5}$$

$$\ddot{y}(t) = -H\ \left(\frac{2\pi}{P}\ v_x\right)^2 \sin\left(\frac{2\pi}{P}\, v_x t\right) \tag{C.6}$$

The maximum velocity, $\frac{2\pi}{P} H\ v_x$, and acceleration, $-H\ \left(\frac{2\pi}{P}\ v_x\right)^2$, in Eqs. (C.5) and (C.6), respectively, are upper-bounded by the machine's maximum velocity and acceleration. If the maximum velocity in Eq. (C.5) is greater than the maximum velocity of the machine's linear stage (i.e. $\frac{2\pi}{P} H\ v_x > v_m$), the linear velocity due to the velocity limitation, v_{xv}, is bounded by:

$$v_{xv} = \frac{P}{2\pi}\, \frac{v_T}{H} \tag{C.7}$$

If the maximum acceleration in Eq. (C.6) is greater than the maximum acceleration of the motor (i.e. $H\ (\frac{2\pi}{P}\ v_x)^2 > a_m$), then the linear velocity due to the velocity limitation, v_{xa}, is upper-bounded by:

$$v_{xa} = \sqrt{\frac{a_m}{H\left(\frac{2\pi}{P}\right)^2}} \tag{C.8}$$

The linear velocity, v_x, is then the minimum of the upper-bounds in Eqs. (C.7) and (C.8):

$$v_x = min(v_{xv}, v_{xa}) \tag{C.9}$$

The velocity profile for the sine wave path is shown in Figure C.1 (b). The time per period, τ_P, for the sine wave infill is therefore:

$$\tau_P = \frac{P}{v_x} \tag{C.10}$$

where v_x is the linear velocity found in Eq. (C.9).

From Eq. (C.10), the time per period, τ_P, is multiplied by the number of periods, P, per specimen length, L, to find the total time to print the wave infill. The time to print the straight, outer contour segments, τ_S, was determined using Eqs. (E.1)-(E.5), which are derived in Appendix E. The total predicted time, $\tau^A(\boldsymbol{x})$, for the toolhead to traverse the wave infill is therefore:

$$\tau^A(\boldsymbol{x}) = \tau_P\left(\frac{L}{P}\right) + \tau_S \tag{C.11}$$

Appendix D
Mass of MEX Wave Infill Flexural Specimen

The mass of specimen M^A is estimated from the wave path length, L_{wave}, cross-sectional area, A_B, and density, ρ, of the deposited bead:

$$M^A = L_{wave}\, A_B\, \rho \tag{D.1}$$

The path length, L_{wave}, of the wave infill was determined using Eq. 2.8. The cross-sectional area of a deposited MEX bead, shown in Figure D.1, is assumed to have a slot-like shape with area, A_B [80]:

$$A_B = \frac{\pi l^2}{4} + l\,(W - l) \tag{D.2}$$

where l is the layer height and W is the beadwidth in the MEX process.

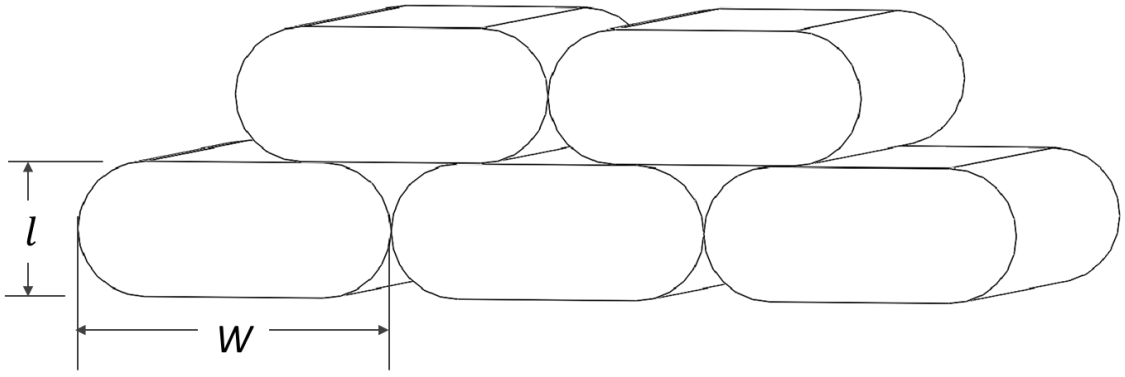

Figure D.1. Cross-sectional area of a deposited MEX beads is assumed to have a slot-like shape with the width of the deposited bead, W, and the layer height, l.

Appendix E
Comparison of Fabrication Time of Wave and Direction-Parallel Infill

A comparison of the time to print equivalent specimens with direction-parallel and wave infill using analytical models and experimental results is presented in this section.

E.1 Fabrication Time for Direction-Parallel Infill

Calculating the fabrication time for the direction-parallel infill requires the toolhead motion assumptions stated in Appendix C.1 (i.e. the toolhead is assumed to have constant acceleration or deceleration, a_m, and a maximum speed, v_m). With a constant acceleration through a linear path, a minimum ramping distance, d_m is required to achieve the maximum speed, v_m:

$$d_m = \frac{{v_m}^2}{2\,a_m} \tag{E.1}$$

The direction-parallel infill, shown in Figure E.1(a), has a period, P, and amplitude, H. The change in direction at each corner requires the overall toolhead speed to decelerate to zero. Depending on the length of the linear segment, d, three velocity profiles, $d < d_m$, $d = d_m$, and $d > d_m$, can be achieved, as shown in Figure E.1(b). The total time for the toolhead to traverse a segment, τ_S, depends on segment length, d. If $d \leq 2\,d_m$,

$$\tau_S = 2\sqrt{\frac{d}{a_m}} \tag{E.2}$$

and if $d > 2\,d_m$,

$$\tau_R = 2\sqrt{\frac{2d}{a_m}} \tag{E.3}$$

$$\tau_C = \frac{d - 2\,d_m}{v_m} \tag{E.4}$$

$$\tau_S = \tau_R + \tau_C \tag{E.5}$$

where τ_R is the ramp time and τ_C is the time at constant velocity. For the direction-parallel infill, the segment length, $d = 2\,H$ for amplitude segments and $d = P/2$ for period segments.

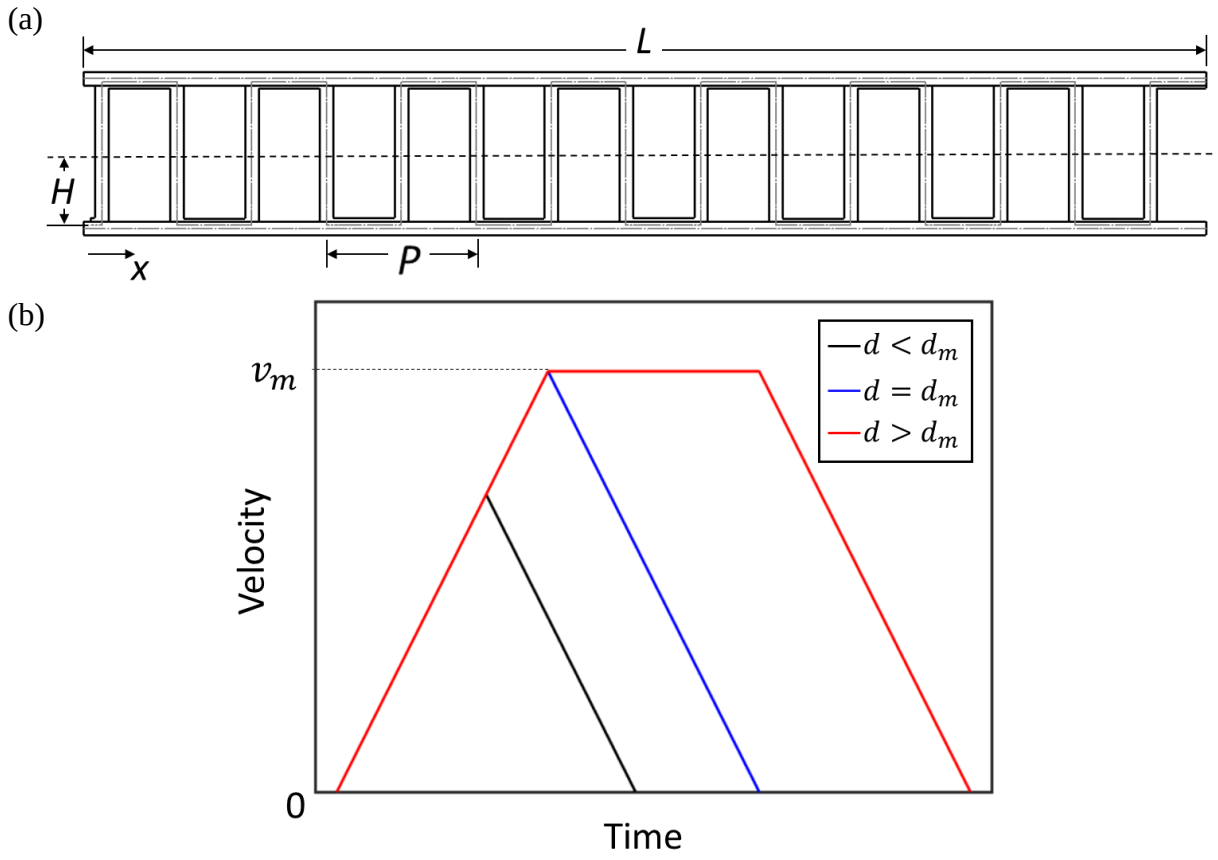

Figure E.1. (a) The direction-parallel infill specimen with amplitude, H, period, P, and length, L and (b) three velocity profiles depending on the length of the linear segment, d, compared with the minimum length required to accelerate to maximum velocity, v_m.

E.2 Efficiency Comparison

The time to print equivalent specimens was compared using the dynamic models with the maximum speed of the linear stage approximated as $v_m = 150$ (mm/s) and the maximum

acceleration approximated as $a_m = 3000$ (mm/s^2). Layer time estimates for both direction-parallel (Figure E.1(a)) and wave infill (Figure 2.2) specimens with equal amplitude and period were calculated for varying thickness, as shown in Figure E.2. For thin-walled parts (i.e. specimens with thickness less than 20 mm) with equivalent infill, the wave infill is up to 10% more efficient. With typical TWS parts having more than one-thousand layers, the added efficiency of using the wave infill can save more than an hour per part.

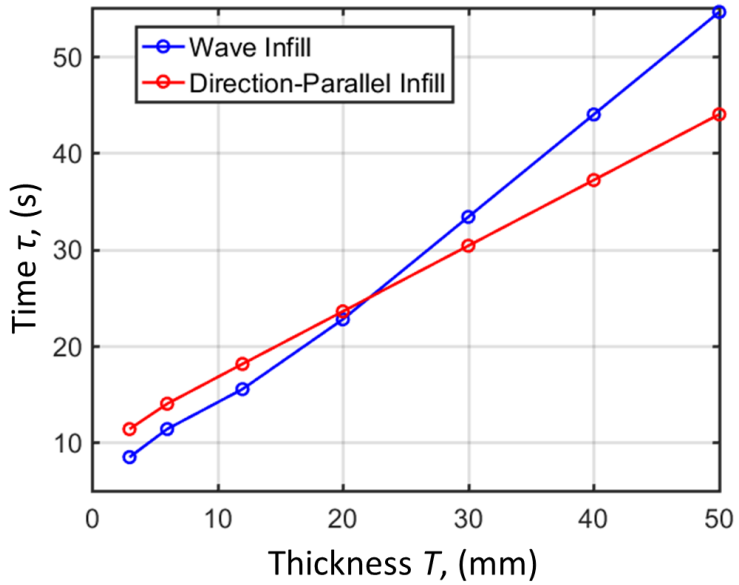

Figure E.2. Analytical time per layer comparison between the wave and direction-parallel infill with varying specimen thickness (and amplitude) and a fixed period, P = 2.0 mm, overlap, O = 0.15 mm, and length, L = 100 mm.

Appendix F
Derivation of the Analytical Expression of the Effective Shear Modulus, G_{YZ}^{C}

A model for calculating the effective shear modulus, G_{YZ}^{C}, is shown in Figure F.1. When a shear stress τ_{YZ} is applied to one of the facings over a half period of the structure (Figure F.1(a)), the stress is transmitted to core, which deforms by δ_{YZ} (Figure F.1(b)). The shear stress generates a shear force, T_{YZ}:

$$T_{YZ} = \tau_{YZ} \left(b \frac{P}{2} \right) \tag{F.1}$$

Because δ_{YZ} of the wave due to the shear force T_{YZ} is difficult to estimate, the deformation of the core can be modeled as the deformation of a flat plate (as shown in Figure F.1(c)) subject to the same T_{YZ}. Using the equation for shear modulus,

$$G = \frac{F/A}{\delta/l} \tag{F.2}$$

the deformation of the flat plate is:

$$\delta_{ZY} = \frac{T_{YZ}\ L_{wave}/2}{W\ b\ G_{XZ}} \tag{F.3}$$

where G_{XZ} is the shear modulus of the base material and $A = b\ W$ and $l = L_{wave}$ is the length of the wave infill of Eq. (F.2) with period of P:

$$L_{wave} = \int_0^P \sqrt{1 + \left(\frac{2\pi}{P}\ H \cos\left(\frac{2\pi}{P} x \right) \right)^2}\ dx \tag{F.4}$$

where H is defined in Eq. (3.1) and shown in Figure 3.2. Using Eqs. (F.2) and (F.3) and the shear modulus equation for Figure F.1(b), the effective shear modulus, G_{YZ}^{C}, of the core lamina is:

$$G_{YZ}^{C} = \frac{4\,T_C\,W}{P\,L_{wave}}\,G_{XZ} \tag{F.5}$$

where $A = b\frac{P}{2}$ and $l = T_C$ of Eq. (F.2) and G_{XZ} for a transversely orthotropic material is:

$$G_{XZ} = \frac{\sqrt{E_X E_Z}}{2(1 + (\nu_{XZ}\nu_{ZX})^{1/2})} \tag{F.6}$$

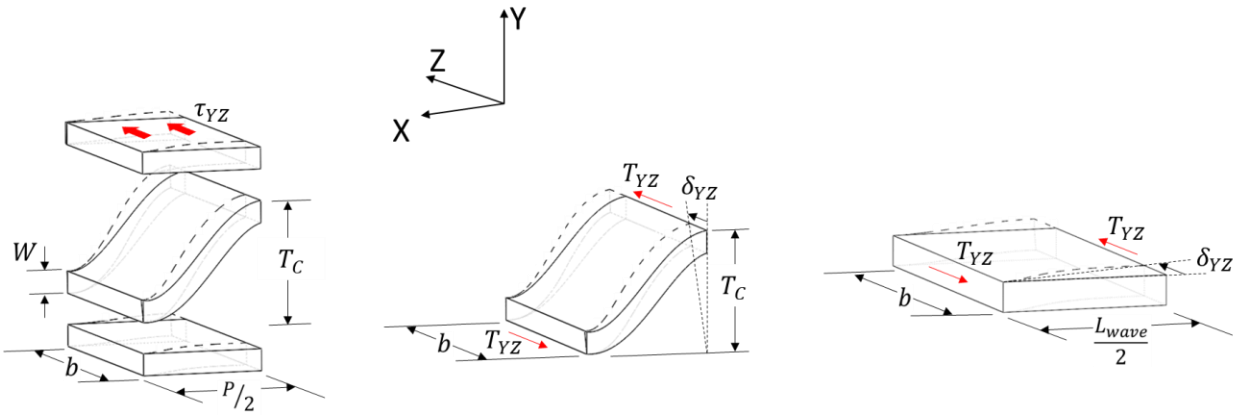

(a) (b) (c)

Figure F.1. (a) Model of MEX wave infill subject to shear stress, τ_{YZ}, (b) deformation, δ_{YZ}, of MEX wave infill core subject to shear force, T_{YZ}, and (c) plate model of the wave infill core for calculating the deformation, δ_{YZ}, due to the shear force, T_{YZ}.

Appendix G
Derivation of the Analytical Expression of the Effective Shear Modulus, G_{YX}^{C}

A model for calculating the effective shear modulus, G_{YX}^{C}, is shown in Figure G.1. The effective shear modulus, G_{YX}^{C}, requires a stress analysis of the wave infill geometry subject to the shear stress, τ_{YX}, on the facing, as shown in Figure G.1(a). With this shear stress, the core structure deforms as shown in Figure G.1(b). To quantify G_{YX}^{C}, of the wave infill core, the deformation and a generalized loading must be related. For this analysis, the wave infill core subjected to the generalized loading will be defined along the axes ξ-ζ. The toolpath of the wave infill core is represented by the function:

$$\zeta = H \sin\left(\frac{2\pi}{P}\,\xi\right) \tag{G.1}$$

The slope at a position on the wave infill is:

$$\phi = \frac{d\zeta}{d\xi} \tag{G.2}$$

An element CD of the wave infill is shown in Figure G.1(c). The shear loading of the face generates longitudinal and shear forces V_D and H_D and moment M_D on the peak of the wave infill element. From applied forces V_D and H_D and moment M_D, equilibrium equations define the forces, $N$and T, and moment M, internal to the core:

$$N = V_D \sin\phi + H_D \cos\phi \tag{G.3}$$

$$T = -H_D \sin\phi + V_D \cos\phi \tag{G.4}$$

$$M = H_D\left(\frac{T_C}{2} - \zeta\right) - V_D\left(\frac{P}{2} - \xi\right) + M_D \tag{G.5}$$

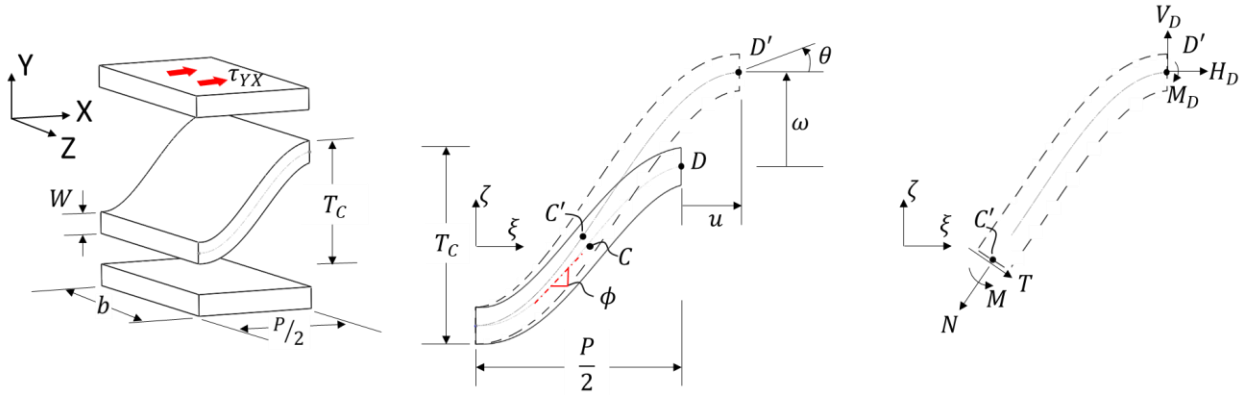

(a) (b) (c)

Figure G.1. (a) Model of MEX wave infill facing subject to shear stress, τ_{YX}. (b) From shear stress, τ_{YX}, the wave infill segment AD deforms to segment AD'. (c) Vertical and horizontal forces, V_D and H_D, respectively, and moment, M_D, from the shear stress, τ_{YX}, are transmitted through the wave infill core element C'D' to generate normal and tangential forces, N and T, respectively, and moment, M. These internal forces and moment are used to calculate stresses in the core.

Compared with normal and bending stresses, shear stresses within wave infill segments are assumed to be negligible in this analysis. The total stress in the wave infill is then:

$$\sigma = \sigma_s + \sigma_b \tag{G.6}$$

where σ_s and σ_b are normal and bending stresses, respectively, given by:

$$\sigma_s = \frac{N}{A_X} \tag{G.7}$$

$$\sigma_b = -\frac{M}{A_X r_o} \tag{G.8}$$

where $A_X \approx b\,W$ and r_o is the radius of curvature of the toolpath centerline:

$$r_o = \left| \frac{(1 + (\zeta')^2)^{\frac{3}{2}}}{\zeta''} \right| \tag{G.9}$$

The normal, ϵ_S, and angular strain, $\frac{d\phi}{ds}$, in the wave infill element are:

$$\epsilon_S = \frac{\sigma}{E_X} \tag{G.10}$$

$$\frac{d\phi}{ds} = -\frac{M}{E_X J} + \frac{\epsilon_S}{r_o} \tag{G.11}$$

where E_X is the X-direction elastic modulus of the base material and J is the second moment of area of the cross-section ($I = \frac{1}{12} b\, W^3$) times a correction factor ($\kappa \approx 1 + \frac{3}{20}\left(\frac{t_c}{r_o}\right)^2 + \frac{3}{112}\left(\frac{t_c}{r_o}\right)^4$).

Assuming small displacements in the core, the rotation $d\phi$ and elongation ϵ_S produce differential axial and vertical displacements, du and $d\omega$, respectively, and rotation, $d\theta$:

$$du = \left(\left(-\frac{d\phi}{ds}\right)\left(\frac{T_C}{2} - \zeta\right) + \epsilon_S \cos\phi\right) ds \tag{G.12}$$

$$d\omega = \left(\left(\frac{d\phi}{ds}\right)\left(\frac{P}{2} - \xi\right) + \epsilon_S \sin\phi\right) ds \tag{G.13}$$

$$d\theta = -\frac{d\phi}{ds} ds \tag{G.14}$$

To obtain the total displacements of the wave infill element, Eqs. G.12-G.14 are integrated over an arc length, S, of the wave:

$$u = \int_S du\ ds \tag{G.15}$$

$$\omega = \int_S d\omega\ ds \tag{G.16}$$

$$\theta = \int_S d\theta\ ds \tag{G.17}$$

where ds is a differential element of the desired arc length, S. To integrate Eqs. G.15-G.17, a change-of-variables from S to ξ must be performed such that the integration can occur over the half period, $\frac{P}{2}$, of the wave infill core. The change-of-variables requires that:

$$\frac{ds}{d\xi} = \sqrt{1 + \left(\frac{d\zeta}{d\xi}\right)^2} \tag{G.18}$$

With these relationships, the applied loads to the core at point D (i.e. global forces) can be related to the total system displacements (i.e. global displacements) by the relationship:

$$\begin{bmatrix} u \\ \omega \\ \theta \end{bmatrix} = \frac{1}{E_X\, A_X} \begin{bmatrix} C_{11} & C_{12} & C_{13} \\ C_{12} & C_{22} & C_{23} \\ C_{13} & C_{23} & C_{33} \end{bmatrix} \begin{bmatrix} H_D \\ V_D \\ M_D \end{bmatrix} \tag{G.19}$$

where C_{ij} are the coefficients of the wave infill core compliance matrix given by:

$$C_{11} = \int_S \left(\left(\frac{12}{\kappa\, W^2} + \frac{1}{r_o^2} \right) \left(\frac{T_c}{2} - \zeta \right)^2 - 2 \left(\frac{\cos\phi}{r_o} \right) \left(\frac{T_c}{2} - \zeta \right) + \cos^2\phi \right) ds \tag{G.20}$$

$$C_{12} = \int_S \left(\left(\frac{-12}{\kappa\, W^2} + \frac{1}{r_o^2} \right) \left(\frac{P}{2} - \xi \right) \left(\frac{T_c}{2} - \zeta \right) - \left(\frac{\cos\phi}{r_o} \right) \left(\frac{P}{2} - \xi \right) - \left(\frac{\sin\phi}{r_o} \right) \left(\frac{T_c}{2} - \zeta \right) + \cos\phi \sin\phi \right) ds \tag{G.21}$$

$$C_{13} = \int_S \left(\left(\frac{12}{\kappa\, W^2} + \frac{1}{r_o^2} \right) \left(\frac{T_c}{2} - \zeta \right) - \left(\frac{\cos\phi}{r_o} \right) \right) ds \tag{G.22}$$

$$C_{22} = \int_S \left(\left(\frac{12}{\kappa\, W^2} + \frac{1}{r_o^2} \right) \left(\frac{P}{2} - \xi \right)^2 + 2 \left(\frac{\sin\phi}{r_o} \right) \left(\frac{P}{2} - \xi \right) + \sin^2\phi \right) ds \tag{G.23}$$

$$C_{23} = \int_S \left(\left(\frac{-12}{\kappa\, W^2} + \frac{1}{r_o^2} \right) \left(\frac{P}{2} - \xi \right) - \left(\frac{\sin\phi}{r_o} \right) \right) ds \tag{G.24}$$

$$C_{33} = \int_S \left(\frac{12}{\kappa\, W^2} + \frac{1}{r_o^2} \right) ds \tag{G.25}$$

During the deformation of the MEX wave infill TWS, the calculation of G_{YZ}^c depends on whether the facings remain rigid during deformation of the core. From experiments, the MEX facings can be assumed to be rigid during shear deformation of the core. With rigid facings, deformations of the wave infill core are subject to two constraints: (1) no rotation of the wave infill segment (i.e. $\theta = 0$) and (2) no change in core thickness, T_C (i.e. $\omega = 0$). Applying these conditions to Eq. G.19 produces:

$$\begin{bmatrix} u \\ 0 \\ 0 \end{bmatrix} = \frac{1}{E_X\, A_X} \begin{bmatrix} C_{11} & C_{12} & C_{13} \\ C_{12} & C_{22} & C_{23} \\ C_{13} & C_{23} & C_{33} \end{bmatrix} \begin{bmatrix} H_D \\ V_D \\ M_D \end{bmatrix} \tag{G.26}$$

G_{YX}^{C} is defined as:

$$G_{YX}^{C} = \frac{\tau_{YX}}{\gamma_{YX}} \tag{G.27}$$

where shear stress, τ_{YX}, and shear deformation, γ_{YX}, for small displacements are:

$$\tau_{YX} = \frac{H_D}{\frac{P}{2}\, b} \tag{G.28}$$

$$\gamma_{YX} = \frac{u}{T_c} + \frac{\omega}{\frac{P}{2}} \tag{G.29}$$

Because thickness is assumed not to change (i.e. $\omega = 0$), G_{YX}^{C} is:

$$G_{YX}^{C} = \frac{H_D}{u}\left(\frac{T_c}{\frac{P}{2}\, b}\right) \tag{G.30}$$

H_D/u relates the horizontal force applied to the wave infill core and its resultant displacement and, with Eq. G.30, can be written in terms of the geometry of the wave infill. To solve for H_D/u using Eq. G.26, V_D and M_D are eliminated from the top row to find:

$$u = \frac{H_D}{E_X A_X} \frac{(-C_{33}C_{12}^2 + 2\, C_{12}C_{13}C_{23} - C_{22}C_{13}^2 - C_{11}C_{23}^2 + C_{11}C_{22}C_{33})}{-C_{23}^2 + C_{22}C_{33}} \tag{G.31}$$

which can be rewritten in terms of $\frac{H_D}{u}$ and simplified:

$$\frac{H_D}{u} = E_X\, A_X \frac{\det\begin{bmatrix} C_{22} & C_{23} \\ C_{23} & C_{33} \end{bmatrix}}{\det\begin{bmatrix} C_{11} & C_{12} & C_{13} \\ C_{12} & C_{22} & C_{23} \\ C_{13} & C_{23} & C_{33} \end{bmatrix}} \tag{G.32}$$

where $\det[\ ]$ is the determinant. Substituting Eq. G.33 into Eq. G.30, G_{XY}^{C} can be expressed in terms of the base material properties and the wave infill geometry:

$$G_{XY}^{C} = E_X\, A_X \left(\frac{T_c}{\frac{P}{2}\; b} \right) \frac{\det \begin{bmatrix} C_{11} & C_{12} \\ C_{12} & C_{22} \end{bmatrix}}{\det \begin{bmatrix} C_{11} & C_{12} & C_{13} \\ C_{12} & C_{22} & C_{23} \\ C_{13} & C_{23} & C_{33} \end{bmatrix}} \tag{G.33}$$

References

[1] Totah, D., Menon, M., Jones-hershinow, C., Barton, K., and Gates, D. H., 2019, "Gait & Posture The impact of ankle-foot orthosis stiffness on gait : A systematic literature review," Gait Posture, **69**(January), pp. 101–111.

[2] Gibson, I., Rosen, D., and Stucker, B., Additive Manufacturing Technologies.

[3] Chisena, R. S., and Shih, A. J., 2018, "Analytical Characterization and Experimental Validation of the Material Extrusion Wave Infill for Thin-Walled Structures," Manuscr. Submitt. Publ.

[4] Shih, A., Park, D. W., Yang, Y.-Y. (Dory), Chisena, R., and Wu, D., 2017, "Cloud-based Design and Additive Manufacturing of Custom Orthoses," Procedia CIRP, **63**, pp. 156–160.

[5] Liu, Y., 2017, "Additive manufacturing techniques and their biomedical applications," Fam. Med. Community Heal., **5**(4), pp. 286–298.

[6] Klippstein, H., Diaz De Cerio Sanchez, A., Hassanin, H., Zweiri, Y., and Seneviratne, L., 2018, "Fused Deposition Modeling for Unmanned Aerial Vehicles (UAVs): A Review," Adv. Eng. Mater., **20**(2), pp. 1–17.

[7] Singerman, R., Hoy, D., and Mansour, J., 1999, "Design Changes in Ankle-Foot Orthosis Intended to Alter Stiffness Also Alter Orthosis Kinematics," J. Prosthetics Orthot., **11**(3).

[8] Han, W., Jafari, M. a., Danforth, S. C., and Safari, A., 2002, "Tool Path-Based Deposition Planning in Fused Deposition Processes," J. Manuf. Sci. Eng., **124**(2), p. 462.

[9] Jin, Y.-A., He, Y., Xue, G.-H., and Fu, J.-Z., 2014, "A parallel-based path generation method for fused deposition modeling," Int. J. Adv. Manuf. Technol., **77**(5–8), pp. 927–

937.

[10] Han, W., Jafari, M. a., and Seyed, K., 2003, “Process speeding up via deposition planning in fused deposition-based layered manufacturing processes,” Rapid Prototyp. J., **9**(4), pp. 212–218.

[11] Mohamed, O. a., Masood, S. H., and Bhowmik, J. L., 2015, “Optimization of fused deposition modeling process parameters: a review of current research and future prospects,” Adv. Manuf., pp. 42–53.

[12] Chin Ang, K., Fai Leong, K., Kai Chua, C., and Chandrasekaran, M., 2006, “Investigation of the mechanical properties and porosity relationships in fused deposition modelling-fabricated porous structures,” Rapid Prototyp. J., **12**(2), pp. 100–105.

[13] Smith, J., Hodgins, J., Oppenheim, I., and Witkin, A., 2002, “Creating models of truss structures with optimization,” ACM Trans. Graph., **21**(3), pp. 295–301.

[14] Wu, J., Aage, N., and Sigmund, O., 2016, “Infill Optimization for Additive Manufacturing – Approaching Bone-like Porous Structures,” Talk, pp. 1–11.

[15] Wu, J., Wang, C. C. L., Zhang, X., and Westermann, R., 2016, “Self-supporting rhombic infill structures for additive manufacturing,” CAD Comput. Aided Des., **80**, pp. 32–42.

[16] Roger, F., and Krawczak, P., 2015, “3D-printing of thermoplastic structures by FDM using heterogeneous infill and multi-materials : An integrated design-advanced manufacturing approach for factories of the future,” Association Française de Mécanique, Lyon, pp. 1–7.

[17] Bendsøe, M. P., and Sigmund, O., 2003, Topology optimization: theory, methods, and applications.

[18] “Contour Crafting - CC” [Online]. Available: http://www.contourcrafting.org/.

[19] Swanson, W., and Mannella, D., 2014, “Method for printing three-dimensional parts with

additive manufacturing using scaffolds."

[20] Nordstrand, T., 2003, "Basic Testing and Strength Design of Corrugated Board and Containers," Lund University.

[21] Luo, S., Suhling, J. C., Considine, J. M., and Laufenberg, T. L., 1992, "The Bending Stiffnesses of Corrugated Board," Mech. Cellul. Mater., **145**, pp. 15–26.

[22] Chisena, R. S., Shih, A. J., Hanson, A., Larson, G., Funes, M., Wensman, J., Bolger, D., and Holhouser, C., 2017, "METHOD OF ADDITIVE MANUFACTURING AN INTERNAL WAVE SPARSE STRUCTURE WITH VARYING GEOMETRY FOR LOCALIZED TUNABLE STRUCTURAL PROPERTIES THROUGHOUT A PART."

[23] Jin, Y., He, Y., and Du, J., 2017, "A novel path planning methodology for extrusion-based additive manufacturing of thin-walled parts," Int. J. Comput. Integr. Manuf., **30**(12), pp. 1301–1315.

[24] Jiménez-Caballero, M. a, Conde, I., García, B., and Liarte, E., 2009, "Design of different types of corrugated board packages using finite element tools," SIMULIA Cust. Conf., pp. 1–15.

[25] Park, J., Kim, G., Kwon, S., Chung, S., Kwon, S., Choi, W., Mitsuoka, M., Inoue, E., Okayasu, T., and Choe, J., 2012, "Finite element analysis of corrugated board under bending stress," J. Fac. Agric. Kyushu Univ., **57**(1), pp. 181–188.

[26] Zhang, Z., Qiu, T., Song, R., and Sun, Y., 2014, "Nonlinear finite element analysis of the fluted corrugated sheet in the corrugated cardboard," Adv. Mater. Sci. Eng., **2014**.

[27] Gilchrist, A. C., Suhling, J. C., and Urbanik, T. J., 1999, "Nonlinear Finite Element Modeling of Corrugated Board," Amd, **231**, pp. 101–106.

[28] Allansson, A., and Svärd, B., 2001, "Stability and collapse of corrugated board; Numerical

and Experimental Analysis," Struct. Mech., **Master's**.

[29] Allaoui, S., Aboura, Z., and Benzeggagh, M., 2011, "Contribution to the modelling of the Corrugated Cardboard Behaviour," p. 10.

[30] Nordstrand, T. M., Carlsson, L. A., and Allen, H. G., 1994, "Transverse shear stiffness of structural core sandwich," Compos. Struct., **27**, pp. 317–329.

[31] Wu, J., 2016, "Infill Optimization for Additive Manufacturing –Approaching Bone-like Porous Structures - Talk," Talk.

[32] Sun, Q., Rizvi, G. M., Bellehumeur, C. T., and Gu, P., 2008, "Effect of processing conditions on the bonding quality of FDM polymer filaments," Rapid Prototyp. J., **14**(2), pp. 72–80.

[33] Tronvoll, S. A., Welo, T., and Elverum, C. W., 2018, "The effects of voids on structural properties of fused deposition modelled parts : a probabilistic approach," pp. 3607–3618.

[34] Properties, M., Strength, T., Method, T., Strength, T., Strength, C., and Properties, T., "FDM Nylon 12CF FDM Nylon 12CF," pp. 1–2.

[35] Upadhyay, K., Dwivedi, R., and Singh, A. K., 2017, "Determination and Comparison of the Anisotropic Strengths of Fused Deposition Modeling P400 ABS," Adv. 3D Print. Addit. Manuf. Technol.

[36] Alafaghani, A., Qattawi, A., Alrawi, B., and Guzman, A., 2017, "Experimental Optimization of Fused Deposition Modelling Processing Parameters: A Design-for-Manufacturing Approach," Procedia Manuf., **10**, pp. 791–803.

[37] Li, H., Zhang, S., Yi, Z., Li, J., Sun, A., Guo, J., and Xu, G., 2017, "Bonding quality and fracture analysis of polyamide 12 parts fabricated by fused deposition modeling," Rapid Prototyp. J., **23**(6), pp. 973–982.

[38] Ning, F., Cong, W., Qiu, J., Wei, J., and Wang, S., 2015, "Additive manufacturing of carbon fiber reinforced thermoplastic composites using fused deposition modeling," Compos. Part B Eng., **80**, pp. 369–378.

[39] Slotwinski, J. A., Garboczi, E. J., and Hebenstreit, K. M., 2014, "Porosity Measurements and Analysis for Metal Additive Manufacturing Process Control," J. Res. Natl. Inst. Stand. Technol., **119**, p. 494.

[40] Zeltmann, S. E., Gupta, N., Tsoutsos, N. G., Maniatakos, M., Rajendran, J., and Karri, R., 2016, "Manufacturing and Security Challenges in 3D Printing," Jom, **68**(7), pp. 1872–1881.

[41] Chen, R., Lo, T., Chen, L., and Shih, A., 2015, "Nano-CT Characterization of Structrual Voids and Air Bubbles in Fused Deposition Modeling for Additive Manufacturing," ASME 2015 International Manufacturing Science and Engineering Conference, American Society of Mechanical Engineering (ASME).

[42] Kim, F. H., Moylan, S. P., Garboczi, E. J., and Slotwinski, J. A., 2017, "Investigation of pore structure in cobalt chrome additively manufactured parts using X-ray computed tomography and three-dimensional image analysis," Addit. Manuf., **17**, pp. 23–38.

[43] Hanke, R., Fuchs, T., and Uhlmann, N., 2008, "X-ray based methods for non-destructive testing and material characterization," Nucl. Instruments Methods Phys. Res. Sect. A Accel. Spectrometers, Detect. Assoc. Equip., **591**(1), pp. 14–18.

[44] Garcea, S. C., Wang, Y., and Withers, P. J., 2018, "X-ray computed tomography of polymer composites," Compos. Sci. Technol., **156**, pp. 305–319.

[45] Kastner, J., Plank, B., Salaberger, D., and Sekelja, J., 2010, "Defect and Porosity Determination of Fibre Reinforced Polymers by X-ray Computed Tomography," NDT Aerosp. 2010 - We.1.A.2, (February 2015), pp. 1–12.

[46] Maire, E., and Withers, P. J., 2014, "Quantitative X-ray tomography," Int. Mater. Rev., **59**(1), pp. 1–43.

[47] Straumit, I., Hahn, C., Winterstein, E., Plank, B., Lomov, S. V., and Wevers, M., 2016, "Computation of permeability of a non-crimp carbon textile reinforcement based on X-ray computed tomography images," Compos. Part A Appl. Sci. Manuf., **81**, pp. 289–295.

[48] Van Bael, S., Kerckhofs, G., Moesen, M., Pyka, G., Schrooten, J., and Kruth, J. P., 2011, "Micro-CT-based improvement of geometrical and mechanical controllability of selective laser melted Ti6Al4V porous structures," Mater. Sci. Eng. A, **528**(24), pp. 7423–7431.

[49] Kerckhofs, G., Pyka, G., Moesen, M., Van Bael, S., Schrooten, J., and Wevers, M., 2013, "High-resolution microfocus X-ray computed tomography for 3d surface roughness measurements of additive manufactured porous materials," Adv. Eng. Mater., **15**(3), pp. 153–158.

[50] J. Bernsen, 1986, "Dynamic Thresholding of Grey-level Images," InternationalConference on Pattern Recognition, Paris, France, p. 1251–1255.

[51] Kim, F. H., Moylan, S. P., Garboczi, E. J., and Slotwinski, J. A., 2017, "Investigation of pore structure in cobalt chrome additively manufactured parts using X-ray computed tomography and three-dimensional image analysis," Addit. Manuf., **17**, pp. 23–38.

[52] Otsu, N., 1979, "A Threshold Selection Method from Gray-Level Histograms," IEEE Trans. Syst. Man. Cybern., **9**(1), pp. 62–66.

[53] Bischoff, M., Bletzinger, K.-U., Wall, W. A., and Ramm, E., 2004, "Models and Finite Elements for Thin-Walled Structures," Encyclopedia of Computational Mechanics, John Wiley & Sons, Ltd.

[54] Bellehumeur, C., Li, L., Sun, Q., and Gu, P., 2004, "Modeling of Bond Formation Between

Polymer Filaments in the Fused Deposition Modeling Process," J. Manuf. Process., **6**(2), pp. 170–178.

[55] Bellini, A., and Güçeri, S., 2003, "Mechanical characterization of parts fabricated using fused deposition modeling," Rapid Prototyp. J., **9**(4), pp. 252–264.

[56] Casavola, C., Cazzato, A., Moramarco, V., and Pappalettere, C., 2016, "Orthotropic mechanical properties of fused deposition modelling parts described by classical laminate theory," Mater. Des., **90**, pp. 453–458.

[57] Ahn, S. H., Baek, C., Lee, S., and Ahn, I. S., 2003, "Anisotropic Tensile Failure Model of Rapid Prototyping Parts - Fused Deposition Modeling (FDM)," Int. J. Mod. Phys. B, **17**(08n09), pp. 1510–1516.

[58] Specimens, P., and Materials, E. I., 2011, "Standard Test Methods for Flexural Properties of Unreinforced and Reinforced Plastics and Electrical Insulating Materials 1," Annu. B. ASTM Stand., (C), pp. 1–11.

[59] Stratasys, 2015, Safety data sheet, Eden Prairie.

[60] Stewart, J., 1995, Calculus, Brooks/Cole Pub. Co., Pacific Grove, Calif.

[61] Ryan, T. P., 2007, "Miscellaneous Design Topics," Modern Experimental Design, John Wiley & Sons, Inc., pp. 483–543.

[62] Stratasys, 2017, FDM Nylon 12.

[63] Nordstrand, T. M., 1995, "Parametric study of the post-buckling strength of structural core sandwich panels," Compos. Struct., **30**(94), pp. 441–451.

[64] Amado-becker, A., Ramos-grez, J., and Gaete, L., 2008, "Elastic tensor stiffness coefficients for SLS Nylon 12 under different degrees of densification as measured by ultrasonic technique," **5**(May), pp. 260–270.

[65] Sezgin, M., 2004, “Survey over image thresholding techniques and quantitative performance evaluation,” **13**(January), pp. 146–165.

[66] Kittler, J., and Illingworth, J., 1986, “Minimum error thresholding,” Pattern Recognit., **19**(1), pp. 41–47.

[67] Nakagawa, Y., and Rosenfeld, A., 1979, “Some experiments on variable thresholding,” Pattern Recognit., **11**(3), pp. 191–204.

[68] O’Hagan, A., and Leonard, T., 1976, “Bayes Estimation Subject to Uncertainty About Parameter Constraints,” Biometrika Trust, **63**(1), pp. 201–203.

[69] Russ, J. C., 2016, “The Image Processing Handbook.”

[70] Gibson, I., Rosen, D. W. D. W., and Stucker, B., 2009, Additive Manufacturing Technologies: Rapid Prototyping to Direct Digital Manufacturing.

[71] Zhong, W., Li, F., Zhang, Z., Song, L., and Li, Z., 2001, “Short fiber reinforced composites for fused deposition modeling,” Mater. Sci. Eng. A, **301**(2), pp. 125–130.

[72] Shofner, M. L., Lozano, K., Rodríguez-Macías, F. J., and Barrera, E. V., 2003, “Nanofiber-reinforced polymers prepared by fused deposition modeling,” J. Appl. Polym. Sci., **89**(11), pp. 3081–3090.

[73] Daniel, I. M., and Ishai, O., 2005, “Engineering mechanics of composite materials,” p. xviii, 411 p.

[74] Stamopoulos, A., Tserpes, K., and Prucha, P., 2014, “Characterization of Porous CFRP Laminates by Mechanical Testing and X-ray Computed Tomography,” 6th Int. Symp. NDT Aerosp., (November), pp. 12–14.

[75] Nikishkov, Y., Airoldi, L., and Makeev, A., 2013, “Measurement of voids in composites by X-ray Computed Tomography,” Compos. Sci. Technol., **89**, pp. 89–97.

[76] Chisena, R. S., Engstrom, S. M., and Shih, A. J., 2019, "Thresholding Method for the Computed Tomography Inspection of the Internal Composition of Parts Fabricated using Additive Manufacturing," Manuscr. Submitt. Publ.

[77] Hibbeler, R. C., 2011, Mechanics of Materials, Prentice Hall.

[78] Weisstein, E. W., "Area Moment of Inertia," MathWorld--A Wolfram Web Resour. [Online]. Available: http://mathworld.wolfram.com/AreaMomentofInertia.html.

[79] Quinones, J. I., 2012, "Applying acceleration and deceleration profiles to bipolar stepper motors," Analog Appl.

[80] Ahn, S., Montero, M., Odell, D., Roundy, S., and Wright, P. K., 2002, "Anisotropic material properties of fused deposition modeling ABS," Rapid Prototyp. J., **8**(4), pp. 248–257.